Nonlinear Optical Properties of Carotenoid and Chlorophyll Harmonophores

by

Danielle Barbara Tokarz

A thesis submitted in conformity with the requirements
for the degree of Doctor of Philosophy

Department of Chemistry
University of Toronto

Nonlinear Optical Properties of Carotenoid and Chlorophyll Harmonophores

Danielle Barbara Tokarz

Doctor of Philosophy

Department of Chemistry
University of Toronto

2014

Abstract

Information regarding the structure and function of living tissues and cells is instrumental to the advancement of cell biology and biophysics. Nonlinear optical microscopy can provide such information, but only certain biological structures generate nonlinear optical signals. Therefore, structural specificity can be achieved by introducing labels for nonlinear optical microscopy. Few studies exist in the literature about labels that facilitate harmonic generation, coined "harmonophores". This thesis consists of the first major investigation of harmonophores for third harmonic generation (THG) microscopy.

Carotenoids and chlorophylls were investigated as potential harmonophores. Their nonlinear optical properties were studied by the THG ratio technique. In addition, a tunable refractometer was built in order to determine their second hyperpolarizability (γ). At 830 nm excitation wavelength, carotenoids and chlorophylls were found to have large negative γ values however, at 1028 nm, the sign of γ reversed for carotenoids and remained negative for chlorophylls. Consequently, at 1028 nm wavelength, THG signal is canceled with mixtures of carotenoids and chlorophylls. Furthermore, when such molecules are covalently bonded as dyads or interact within photosynthetic pigment-protein complexes, it is found that additive effects with

the γ values still play a role, however, the overall γ value is also influenced by the intra-pigment and inter-pigment interaction.

The nonlinear optical properties of aggregates containing chlorophylls and carotenoids were the target of subsequent investigations. Carotenoid aggregates were imaged with polarization-dependent second harmonic generation and THG microscopy. Both techniques revealed crystallographic information pertaining to H and J aggregates and β-carotene crystalline aggregates found in orange carrot. In order to demonstrate THG enhancement due to labeling, cultured cells were labeled with carotenoid incorporated liposomes. In addition, *Drosophila melanogaster* larvae muscle as well as keratin structures in the hair cortex were labeled with β-carotene.

Polarization-dependent THG studies may be particularly useful in understanding the structural organization that occurs within biological structures containing carotenoids and chlorophylls such as photosynthetic pigment-protein complexes and carotenoid aggregates in plants and alga. Further, artificial labeling with carotenoids and chlorophylls may be useful in clinical applications since they are nontoxic, nutritionally valuable, and they can aid in visualizing structural changes in cellular components.

Acknowledgments

Thanks to my supervisors, Professor Virginijus Barzda and Professor Ulrich Fekl. Two professors from two different disciplines came together to develop a project which I have been so fortunate to call mine for the past few years. I am extremely grateful that they decided to take a chance on me! I am also thankful for their support, patience, understanding, knowledge, motivation and enthusiasm throughout this entire process.

Thank you to my committee members, Professor Claudiu Gradinaru and Professor Ulrich Krull. Both professors have been tremendously supportive of my interdisciplinary studies and I thank them for their guidance and wisdom. I would also like to thank Professor Garth J. Simpson for serving on my exam committee, but also, for inspiring much of the work presented in the thesis.

A strong support system is necessary for surviving graduate school. Many thanks are in order to the members of the Barzda Group for looking after me and treating me as one of the physicists. I would like to further extend my gratitude to Richard Cisek for guidance throughout each and every project that I pursued. Thank you to Nicole Prent for programming help and research advice. Thank you to Daaf Sandkuijl for assistance with the laser as well as research and life advice during the occasional beer. Thank you to Adam Tuer for all his help with the THG ratio technique as well as his assistance with course work and also for listening to my complaints. Thank you to Masood Samim for help with course work as well as research advice and also for listening to my many complaints. Thank you to Serguei Krouglov for his help in developing equations for PIPO THG and answering my many questions. Thank you to Lukas Kontenis for fluorescence lifetime measurements. Thanks to Ahmad Golaraei for friendly discussions.

Thanks to the Fekl Group for their support and research advice. In particular, thanks to Antonio De Crisci for teaching me how to work in a chemistry lab, but also his encouragement during this project. Thanks to Neilson Nguyen and Dan Harrison for advice and helpful discussions.

Thanks to Peter Duggan of the UTM Machine Shop for all his help with the prism holder and spacers. Thank you to Andrew Veglio, Peter Mui and Mirosław Szreder at UTM Micro-Electronics for seeing through the resurrection of my refractometer power supply several times.

I have had the pleasure of working with many collaborators. Thank you to Laura Junker for HPLC data, carotenoids and chlorophylls, and enjoyable conversations about love, life, and carotenoids. Thanks to Professor Bryan Stewart and Xinping Qiu for interesting research ideas and an endless supply of cells. Thanks to Professor George Espie and Omar El-Ansari for many interesting research discussions and the growing of alga. Thanks to Martyna Garbaczewska for countless hours of muscle dissections, and Professor Joel Levine for fruit fly samples. Thanks to Professor Tom Moore, Professor Ana Moore, Katie Wong Carter and Smitha Pillai for the dyads.

Thank you to the Department of Chemistry and the Department of Chemical and Physical Sciences at UTM who have both offered me many opportunities during my Ph.D. career that I will never forget! Thank you to the granting agencies including the Natural Sciences and Engineering Research Council of Canada (NSERC), the Canadian Institutes of Health Research, the Ontario Centres of Excellence, Canada Foundation for Innovation, and Ontario Innovation Trust for making my project possible. I would like to also acknowledge NSERC and the Ontario Graduate Scholarship program for financial support.

Thanks to my family for their love and encouragement. To my beloved parents, Barbara and Andrew, and my brother, Michael, who have constantly supported me throughout this process. I hope to continue to make you proud in who I am and what I do. To my husband who has loved me and cared for me during this entire process. The best outcome from these past years has been finding you.

"*I have so loved the joys of discovery,*
of connecting physical chemistry with other areas,
of participating in that great central mystery
of the connection of mathematics and physics
to what happens in the world of matter."

Professor Kent R. Wilson*

*Wilson, K. R. (1999). "Summing up - Kent R. Wilson." Journal of Physical Chemistry A **103**(49): 10022-10034.

Table of Contents

List of Tables

List of Figures

List of Abbreviations

2P FL	two-photon excitation fluorescence
3D	three-dimensional
3P FL	three-photon excitation fluorescence
9 db	9 double bonds
10 db	10 double bonds
abs	absorption
Ast	astaxanthin
β-car	β-carotene
Can	canthaxanthin
Chl *a*	chlorophyll *a*
CMOS	complementary metal-oxide semiconductor
CO	collection objective
D	dipolar term
DM	dichroic mirror
DMF	dimethylformamide
DMSO	dimethyl sulfoxide
DPPC	DL-α-phosphatidylcholine, dipalmitoyl
DPPG	1,2- dipalmitoylphosphatidylglycerol
EO	excitation objective

F	filter
fl	fluorescence
FM	flipping mirror
FWHM	full-width half-maximum
GFP	green fluorescent protein
ic	internal conversion
IR	infrared
isc	intersystem crossing
L	lens
LED	light emitting diode
LH1	light-harvesting complex 1
LH2	light-harvesting complex 2
LHCII	light-harvesting chlorophyll *a*/*b* pigment-protein complex
Lut	lutein
M	mirror
MPF	multiphoton excitation fluorescence
N	negative term
NA	numerical aperture
Neo	neoxanthin
PH	pinhole

PIPO	polarization-in, polarization-out
PMT	photomultiplier tube
POPC	1-palmitoyl-2-oleoyl-*sn*-glycero-3-phosphocholine
S2	*Drosophila* Schneider 2
SHG	second harmonic generation
THG	third harmonic generation
Ti:Sapphire	titanium-doped sapphire oscillator
TP	two-photon term
UTM	University of Toronto Mississauga
UV	ultraviolet
Vio	violaxanthin
YAG	yttrium aluminum garnet
Yb:KGW	ytterbium-doped potassium gadolinium tungstate oscillator
ZnNcS	sulfonated zinc (II) 2,3-naphthalocyanine porphyrin

List of Publications

As part of the thesis work, several refereed publications were generated. The works marked with an asterisk are directly related or referenced in this thesis:

***Tokarz, D.**, Cisek, R., Krouglov, S., Kontenis, L., Fekl, U., and Barzda, V. (2013) "Molecular organization in crystalline β-carotene from carrots determined with polarization second and third harmonic generation microscopy." Submitted and under review.

***Tokarz, D.**, Cisek, R., Fekl, U., and Barzda, V. (2013) "The molecular second hyperpolarizability of the light-harvesting chlorophyll *a*/*b* pigment-protein complex of photosystem II." Journal of Physical Chemistry B **117**(38): 11069-11075.

Sandkuijl, D., Tuer, A., **Tokarz, D**., Sipe, J.E., and Barzda, V. (2013) "Numerical second- and third-harmonic generation microscopy." Journal of the Optical Society of America B: Optical Physics **30**(2): 382-395.

***Tokarz, D.**, Cisek, R., Prent, N., Fekl, U., and Barzda, V. (2012) "Measuring the molecular second hyperpolarizability in absorptive solutions by the third harmonic generation ratio technique." Analytica Chimica Acta **755**(2012): 86-92.

***Tokarz, D.**, Cisek, R., Garbaczewska, M., Sandkuijl, D., Qiu, X., Stewart, B., Levine, J.D., Fekl, U., and Barzda, V. (2012) "Carotenoid based bio-compatible labels for third harmonic generation microscopy." Physical Chemistry Chemical Physics **14**(30): 10653-10661.

Tuer, A., Krouglov, S., Cisek, R., **Tokarz, D.** and Barzda, V. (2011) "Three-dimensional visualization of the first hyperpolarizability tensor." Journal of Computational Chemistry **32**(6): 1128-1134.

Tuer, A., **Tokarz, D.**, Prent, N., Cisek, R., Alami, J., Dumont, D.J., Bakueva, L., Rowlands, J., and Barzda, V. (2010) "Nonlinear Multicontrast Microsopy of Hematoxylin-and-Eosin-Stained Histological Sections." Journal of Biomedical Optics **15**(2): 0260181-0260189.

***Tokarz, D.**, Tuer, A., Cisek, R., Krouglov, S., and Barzda, V. (2010) "*Ab initio* calculations of the linear and nonlinear optical properties of amino acids." Journal of Physics: Conference Series **256**(1): 0120151-0120155.

Chapter 1
Molecular Labels for Nonlinear Optical Microscopy

1.1 The Pursuit of Harmonophores

Nonlinear optical microscopy is highly valued as a technique used for noninvasive structural visualization without labeling. However, harmonic generation is not always highly specific to particular biomolecules or cell organelles. Structural specificity can be achieved by designing molecular labels for nonlinear optical microscopy that demonstrate large second-order and third-order optical nonlinearities. Labels for harmonic generation microscopy are referred to as 'harmonophores'. Harmonophores are analogous to fluorophores however, since harmonic generation is described by a tensor rather than a vector, structural information about the sample can be obtained. As well, photobleaching can be reduced as long as the harmonophore molecules do not absorb light at the fundamental laser wavelength and the corresponding harmonic wavelength. Therefore, labeling with harmonophores alongside fluorophores may offer more biological information.

In this chapter, the concept of fluorescence labels will first be introduced along with their impact on current research. Then, an introduction to the history of nonlinear optical microscopy will be presented. The biological structures that are imaged in this thesis with harmonic generation microscopy will also be discussed. The second section of this chapter will introduce nonlinear optical susceptibilities and hyperpolarizabilities that characterize the ability of materials and molecules, respectively to generate nonlinear optical responses. Lastly, molecular properties of efficient harmonophores will be discussed.

1.1.1 Labeling in Fluorescence Microscopy

The first fluorescence microscope was built in 1911 by the physicist O. Heimstädt (Rusk 2009). One of the major challenges O. Heimstädt had to overcome included concentrating enough ultraviolet (UV) light on a sample to cause the sample to fluoresce (Rusk 2009). In order to do this, O. Heimstadt used cuvettes constructed by H.M. Lehmann to eliminate all wavelengths of light except for UV generated by his carbon arc lamp light source. His microscope images were free of noise as he employed dark field illumination that ensured no excitation light would enter

the objective lens. This provided high contrast since the fluorescence signal was observed on a dark background.

With his invention, O. Heimstädt imaged the autofluorescence from many biological organisms; however, due to the limitation of imaging only autofluorescence, Oskar Heimstädt was pessimistic about the future of his invention (Rusk 2009). It wasn't until two decades later when M. Haitinger and his team of chemists developed a technique in which they could apply exogenous fluorescent chemicals to samples allowing for targeted fluorescence labeling of structures, which do not naturally fluoresce (Rusk 2009). M. Haitinger referred to these dyes as 'fluorochromes'(Rusk 2009). Fluorochromes (now commonly known as fluorophores), since their development as functionalized labels for targeting specific biological molecules in 1933, have become essential to the application of the fluorescence microscopy in biological imaging. Even a specific fluorophore, the green fluorescent protein (GFP), was highly recognized, as the Nobel Prize in Chemistry in 2008 was awarded to O. Shimomura, M. Chalfie and R. Y. Tsien for the discovery and development of this fluorophore. The introduction and expression of the GFP gene in cells facilitated time lapse studies of cell dynamics with fluorescence microscopy.

1.1.2 Labeling in Nonlinear Optical Microscopy

The field of nonlinear optics began with the discovery of second harmonic generation (SHG) by P.A. Franken et al. in 1961 (Franken, Weinreich et al. 1961). After the invention of the laser by T.H. Maiman in 1960, P.A. Franken et al. demonstrated the ability to generate light with twice the frequency of incident light when a pulsed ruby laser was focused onto crystalline quartz (Franken, Weinreich et al. 1961). Only intense electric fields are strong enough to induce nonlinear optical responses (Boyd 2008).

Decades later, microscopes capable of imaging nonlinear optical phenomena were designed, including: a second harmonic generation microscope invented by C.J.R. Sheppard et al. in 1977 (Sheppard, Gannaway et al. 1977) and a multiphoton fluorescence microscope invented by W. Denk et al. in 1990 (Denk, Strickler et al. 1990). Third harmonic generation (THG) from interfaces was demonstrated by Tsang in 1995 (Tsang 1995) and a couple years later, the third harmonic generation microscope was described by Barad et al. (Barad, Eisenberg et al. 1997). Since the development of these microscopes, much research has concentrated on studying biological structures which naturally give rise to SHG and THG. For instance, SHG

microscopy has been used to study biological crystalline structures such as collagen (Freund and Deutsch 1986, Stoller, Reiser et al. 2002), starch granules (Mizutani, Sonoda et al. 2000, Chu, Chen et al. 2001), cellulose (Chu, Chen et al. 2001), myosin (Chu, Chen et al. 2004, Greenhalgh, Prent et al. 2007), calcite found in the pineal gland of brain (Baconnier and Lang 2004), aggregates of the light-harvesting chlorophyll *a*/*b* pigment-protein complex of photosystem II (LHCII) (Prent, Cisek et al. 2005, Barzda 2008, Cisek, Prent et al. 2009, Cisek, Spencer et al. 2009), and integral membrane proteins such as human β2-adrenergic receptor fused to lysozyme from T4 phage (Kissick, Gualtieri et al. 2010, Gualtieri, Guo et al. 2011, Haupert and Simpson 2011, Kissick, Dettmar et al. 2013). Examples of biological structures visualized with THG microscopy include plant leaf cells (Muller, Squier et al. 1998), rhizoids from green algae (Squier, Muller et al. 1998), chloroplasts (Millard, Wiseman et al. 1999, Chu, Chen et al. 2001, Barzda 2008, Cisek, Spencer et al. 2009), erythrocytes (Millard, Wiseman et al. 1999), cultured neurons and yeast cells (Yelin and Silberberg 1999), glial cells (Barille, Canioni et al. 2001), LHCII aggregates (Prent, Cisek et al. 2005, Barzda 2008, Cisek, Prent et al. 2009, Cisek, Spencer et al. 2009), sea urchin larval spicules (Oron, Tal et al. 2003), cristae in mitochondria (Barzda, Greenhalgh et al. 2005), myocytes (Chu, Chen et al. 2004, Barzda, Greenhalgh et al. 2005), *Drosophila* embryos (Supatto, Debarre et al. 2005), hemozoin crystals in malaria infected blood cells (Belisle, Costantino et al. 2008), human cornea (Olivier, Aptel et al. 2010), leukocytes (Tsai, Chen et al. 2012) and adipocytes (Tsai, Wang et al. 2013).

Although SHG and THG microscopy are highly valued for noninvasive structural visualization without labeling, specificity and high contrast can be achieved by designing molecular labels analogous to fluorophores that demonstrate large second-order or third-order optical nonlinearities. Molecules capable of generating strong harmonic signals are referred to as ‘harmonophores,’ a term coined by Professor Kent Wilson (Millard, Campagnola et al. 2003). Examples of harmonophores that have been shown to label and enhance the SHG signal intensity of stained intracellular structures include dyes aligned in cellular lipid bilayers in order to preserve a noncentrosymmetric arrangement, which is required for SHG (Barsu, Fortrie et al. 2006, Teisseyre, Millard et al. 2007, De Meulenaere, Asselberghs et al. 2009, Reeve, Collins et al. 2009, Barsu, Cheaib et al. 2010, De Meulenaere, Chen et al. 2012). Examples of THG harmonophores include tissue stained with the histological dye hematoxylin (Tuer, Bakueva et al. 2008, Yu, Tai et al. 2008, Tuer, Tokarz et al. 2010). This stain demonstrates increased THG

intensity from intracellular structures rich in nucleic acids including the nucleus, mitochondria, and ribosomes (Tuer, Bakueva et al. 2008, Yu, Tai et al. 2008, Tuer, Tokarz et al. 2010). Other examples include lipid enclosed cadmium selenide quantum dots functionalized with antibodies which have been used with THG microscopy to detect the expression of receptors in live breast cancer cells (Chang, Chen et al. 2008). Other metallic and semiconductor nanoparticles could also be used for labeling purposes. Examples include gold nanoparticles (Yelin, Oron et al. 2003, Lippitz, van Dijk et al. 2005) and silver nanoparticles (Liu, Tai et al. 2006) which exhibit enhanced THG when illuminated with light in resonance with their surface plasmon modes.

In this thesis, carotenoid and chlorophyll pigments were investigated as potential harmonophores for THG microscopy. Previous studies have shown that conjugated compounds such as β-carotene produce large linear and nonlinear optical responses (Hermann, Ricard et al. 1973, Hermann and Ducuing 1974, Boyd 2008). In addition to this, carotenoids and chlorophylls occur in nature, they are nontoxic and they have nutritional value in the human diet. Therefore, unlike metallic or semiconductor nanoparticles, which have been used in biological studies, carotenoid and chlorophyll pigments offer a safe alternative for labeling to enhance the harmonic generation imaging contrast for *in vivo* microscopy.

In order to determine the usefulness of harmonophores in THG microscopy, the ability for harmonophores to generate THG must be characterized. An introduction to nonlinear optical processes and parameters used to quantify the ability of a harmonophore to generate SHG and THG will be introduced in the following section.

1.2 Nonlinear Optical Processes

1.2.1 Introduction to Hyperpolarizabilities and Nonlinear Optical Susceptibilities

Light has an electric field component, $\boldsymbol{E_{loc}}$, which can interact with the charges, q, found in a molecule producing a force (equal to $q\boldsymbol{E_{loc}}$). This causes an instantaneous displacement of the electron density of an atom away from the nucleus resulting in charge separation and an induced dipole moment, $\boldsymbol{\mu}$. For small electric fields typical of linear optical processes such as reflection, refraction and linear absorption, the induced dipole moment is proportional to the strength of the applied electric field (Stucky, Marder et al. 1991):

$$\boldsymbol{\mu} = \boldsymbol{\mu}_{\circ} + \alpha : \boldsymbol{E}_{loc} \tag{1.2.1}$$

where $\boldsymbol{\mu_o}$ is the static dipole moment in the absence of an applied electric field, α is the linear polarizability tensor and ":" denotes tensor multiplication which is not specific to tensor rank.

For the case of intense electric field strengths, the induced dipole moment of a molecule depends nonlinearly on the applied electric field strength. Mathematically, the induced dipole moment can be expressed as a power series of the applied electric field (Stucky, Marder et al. 1991):

$$\boldsymbol{\mu} = \boldsymbol{\mu}_{\circ} + \alpha : \boldsymbol{E}_{loc} + \beta : \boldsymbol{E}_{loc}\boldsymbol{E}_{loc} + \gamma : \boldsymbol{E}_{loc}\boldsymbol{E}_{loc}\boldsymbol{E}_{loc} + ... \tag{1.2.2}$$

The tensors β and γ are referred to as the first and second hyperpolarizabilities, respectively. In order to fully describe the first hyperpolarizability, 27 elements are required while 81 elements are needed to fully define the second hyperpolarizability. The first hyperpolarizability expresses the ability of a molecule to generate second-order nonlinear optical processes such as second harmonic generation, while the second hyperpolarizability describes the ability of a molecule to generate third-order nonlinear optical processes including third harmonic generation and two-photon excitation fluorescence.

For an ensemble of molecules in bulk material, polarization $\boldsymbol{P}$ is defined as the dipole moment per unit volume which can be expressed as (Stucky, Marder et al. 1991):

$$\boldsymbol{P} = \varepsilon_{\circ} N \langle \boldsymbol{\mu} \rangle \tag{1.2.3}$$

where ε_o is the permittivity of free space, N is the number density of molecules and $<\boldsymbol{\mu}>$ is the average dipole moment of the material. Thus, the polarizability of an isotropic material can be expressed as (Stucky, Marder et al. 1991):

$$\boldsymbol{P} = \varepsilon_{\circ} N \langle \mu_{\circ} \rangle + \varepsilon_{\circ} N \langle \alpha \rangle : \boldsymbol{E}_{loc} + \varepsilon_{\circ} N \langle \beta \rangle : \boldsymbol{E}_{loc}\boldsymbol{E}_{loc} + \varepsilon_{\circ} N \langle \gamma \rangle : \boldsymbol{E}_{loc}\boldsymbol{E}_{loc}\boldsymbol{E}_{loc} + ... \tag{1.2.4}$$

where $<\mu_o>$, $<\alpha>$, $<\beta>$ and $<\gamma>$ are orientationally averaged tensors.

The polarizability of an isotropic material can be expressed in terms of the applied electric field where the material susceptibilities are proportional to the orientationally averaged tensors, $<\mu_o>$, $<\alpha>$, $<\beta>$ and $<\gamma>$ (Boyd 2008):

$$\begin{aligned} \boldsymbol{P} &= \varepsilon_\circ \chi^{(0)} + \varepsilon_\circ \chi^{(1)} : \boldsymbol{E} + \varepsilon_\circ \chi^{(2)} : \boldsymbol{EE} + \varepsilon_\circ \chi^{(3)} : \boldsymbol{EEE} + \ldots \\ \boldsymbol{P} &= \boldsymbol{P}_\circ^{(0)} + \boldsymbol{P}^{(1)} + \boldsymbol{P}^{(2)} + \boldsymbol{P}^{(3)} + \ldots \end{aligned} \tag{1.2.5}$$

where $\boldsymbol{P}_\circ^{(0)}$ is the static dipole of the material, $\boldsymbol{E}$ is the total applied electric field, $\chi^{(1)}$ is the linear optical susceptibility of an ensemble of molecules while $\chi^{(2)}$ and $\chi^{(3)}$ are referred to as the second-order and third-order nonlinear optical susceptibility tensors, respectively.

The local fields in the microscopic expression are related to the total applied electric field in the macroscopic expression by the following relation (Boyd 2008):

$$\begin{aligned} \boldsymbol{E}_{loc} &= \boldsymbol{E} + \frac{1}{3}\chi^{(1)}\boldsymbol{E} \\ \boldsymbol{E}_{loc} &= \left(\frac{\varepsilon^{(1)} + 2}{3}\right)\boldsymbol{E} \end{aligned} \tag{1.2.6}$$

where $\varepsilon^{(1)}$ is the linear dielectric constant.

Therefore, the second-order nonlinear optical susceptibility tensor of isotropic material can be related to the average orientational first hyperpolarizability where it is assumed that the molecules do not interact (Boyd 2008):

$$\chi_{ijk}^{(2)}\left(\omega_m + \omega_n; \omega_m, \omega_n\right) = f^{(2)}\left(\omega_m + \omega_n, \omega_m, \omega_n\right) N \left\langle \beta\left(\omega_m + \omega_n, \omega_m, \omega_n\right)\right\rangle \tag{1.2.7}$$

where the frequency dependency of $\chi^{(2)}$ is noted. The frequency summation, $\omega_m + \omega_n$, represents the frequency of the output field while ω_m and ω_n are the frequencies of the incoming fields. $f^{(2)}$ is the local-field enhancement factor relating the local electric field to the total electric field. Interactions between neighboring dipoles are taken into account through the local field correction factors (Boyd 2008):

$$f^{(2)}\left(\omega_m+\omega_n;\omega_m,\omega_n\right)=\left(\frac{\varepsilon^{(1)}\left(\omega_m+\omega_n\right)+2}{3}\right)\left(\frac{\varepsilon^{(1)}\left(\omega_m\right)+2}{3}\right)^2 \tag{1.2.8}$$

For second harmonic generation, $\omega_m = \omega_n$, and thus, the local-field enhancement factor can be simplified to (Boyd 2008):

$$\left(\frac{\varepsilon^{(1)}\left(\omega_m+\omega_n\right)+2}{3}\right)\left(\frac{\varepsilon^{(1)}\left(\omega_m\right)+2}{3}\right)^2 \approx \left(\frac{n_{2\omega}^2+2}{3}\right)\left(\frac{n_{\omega}^2+2}{3}\right)^2 \tag{1.2.9}$$

where the local field correction can be approximated by the refractive indices at the second harmonic frequency (2ω) and fundamental frequency (ω) when experiments are done off-resonance for isotropic materials.

Similarly, the third-order nonlinear optical susceptibility tensor of isotropic material can be related to the average orientational second hyperpolarizability where it is assumed that the molecules do not interact (Boyd 2008):

$$\begin{aligned}\chi_{ijkl}^{(3)}\left(\begin{matrix}\omega_m+\omega_n+\omega_o;\\ \omega_m,\omega_n,\omega_o\end{matrix}\right)&= f^{(3)}\left(\begin{matrix}\omega_m+\omega_n+\omega_o,\\ \omega_m,\omega_n,\omega_o\end{matrix}\right)N\left\langle\gamma\left(\begin{matrix}\omega_m+\omega_n+\omega_o,\\ \omega_m,\omega_n,\omega_o\end{matrix}\right)\right\rangle\\ f^{(3)}\left(\omega_m+\omega_n+\omega_o;\omega_m,\omega_n,\omega_o\right)&=\left(\frac{\varepsilon^{(1)}\left(\omega_m+\omega_n+\omega_o\right)+2}{3}\right)\left(\frac{\varepsilon^{(1)}\left(\omega_m\right)+2}{3}\right)^3\end{aligned} \tag{1.2.10}$$

For third harmonic generation, $\omega_m = \omega_n = \omega_o$. and therefore, the local-field enhancement factor can be simplified to (Boyd 2008):

$$\left(\frac{\varepsilon^{(1)}\left(3\omega_m\right)+2}{3}\right)\left(\frac{\varepsilon^{(1)}\left(\omega_m\right)+2}{3}\right)^3 \approx \left(\frac{n_{3\omega}^2+2}{3}\right)\left(\frac{n_{\omega}^2+2}{3}\right)^3 \tag{1.2.11}$$

where the local field correction can be approximated by the refractive indices at the third harmonic frequency (3ω) and fundamental frequency (ω) when experiments are done off-resonance for isotropic materials.

1.2.2 The Nonlinear Optical Wave Equation

A laser excitation source can induce all orders of nonlinear optical polarization and as a result, many different nonlinear optical processes can simultaneously take place in a medium. Nonlinear optical processes are characterized by new components of the electromagnetic field. Nonlinear optical polarization, $\boldsymbol{P}^{\boldsymbol{NL}}$, drives waves with amplitude, $\boldsymbol{E}$, generalized by the nonlinear optical wave equation (Boyd 2008):

$$\nabla^2 \boldsymbol{E} - \frac{n^2}{c^2}\frac{\partial^2 \boldsymbol{E}}{\partial t^2} = \frac{1}{\varepsilon_\circ c^2}\frac{\partial^2 \boldsymbol{P}^{\boldsymbol{NL}}}{\partial t^2} \tag{1.2.12}$$

where n represents the linear index of refraction, c is the speed of light in vacuum, and t is time.

For an electromagnetic field propagating along the z-axis, the electric field and nonlinear polarization can be expressed as (Boyd 2008):

$$\begin{aligned} \boldsymbol{E}(r,t) &= A(r,t)e^{i(kz-\omega t)} + A(r,t)e^{-i(kz-\omega t)} \\ \boldsymbol{P}^{\boldsymbol{NL}}(r,t) &= p^{NL}(r,t)e^{i(kz-\omega t)} + p^{NL}(r,t)e^{-i(kz-\omega t)} \end{aligned} \tag{1.2.13}$$

where $A(r, t)$ is the amplitude of the electric field, k is the wave vector also equal to $2\pi n/\lambda$ where n is the refractive index, λ is the wavelength and ω is the angular frequency also equal to $2\pi/T$ where T is the period of oscillation at λ.

In order to solve the nonlinear optical wave equation, the slowly varying amplitude approximation (also known as the slowly varying envelope approximation) is assumed. This implies that the electric field amplitude varies only slowly with respect to space and time. As a result, the second derivative of the amplitude with respect to space and time can be neglected.

The resultant nonlinear optical wave equation becomes (Boyd 2008):

$$2ik_q \frac{\partial A_q}{\partial z} + \nabla^2 A_q = -\frac{\omega_q^2}{\varepsilon_\circ c^2} p^{NL} e^{i\Delta kz} \tag{1.2.14}$$

where the coefficient q is used to express the order of the nonlinear optical process and Δk is referred to as the phase mismatch or the wave-vector mismatch. Δk is equal to (Boyd 2008):

$$\Delta k = qk_{\omega} - k_{q\omega} \tag{1.2.15}$$

where k_{ω} is the wave vector at the fundamental frequency and $k_{q\omega}$ is the wave vector of the q^{th} order nonlinear optical process.

The nonlinear optical responses used in the thesis will be described in the following sections.

1.2.3 Multiphoton Excitation Fluorescence

Multiphoton excitation fluorescence (MPF) occurs by first, molecular absorption of two or more photons causing excitation of an electron from a ground state to an excited state. From the excited state, the electron can experience nonradiative relaxation to the lowest excited state. At this point, the electron may further undergo internal conversion to the ground state or a photon may be emitted bringing the molecule to the ground state. This radiative process is referred to as multiphoton excitation fluorescence. Intersystem crossing to the triplet state from the lowest excited singlet state may also occur. This process leads to excitation relaxation pathways including phosphorescence.

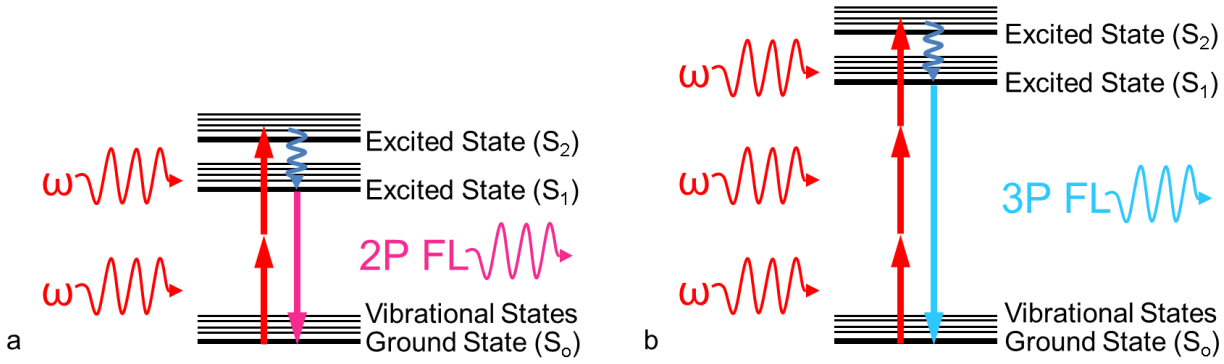

Figure 1.2.1: Multiphoton excitation fluorescence. Energy level schematic diagrams of (a) two-photon excitation fluorescence (2P FL) and (b) three-photon excitation fluorescence (3P FL).

For the two-photon absorption process, the nonlinear absorption cross section, σ, is described as (Boyd 2008):

$$\sigma = \sigma^{(2)} I \tag{1.2.16}$$

where $\sigma^{(2)}$ describes the strength of the two-photon absorption process.

Two-photon absorption is related to the imaginary $\chi^{(3)}$:

$$\sigma^{(2)} \propto \omega \mathrm{Im}\left(\chi^{(3)}\left(-\omega;\omega,-\omega,\omega\right)\right) \tag{1.2.17}$$

The two photon absorption transition rate is expressed as (Boyd 2008):

$$R = \frac{\sigma^{(2)} I^2}{\hbar\omega} \tag{1.2.18}$$

where ω is the excitation frequency.

Substitution of equations (1.2.16) and (1.2.17) into equation (1.2.18) result in the following relation:

$$R \propto \mathrm{Im}\left(\chi^{(3)}\left(-\omega;\omega,-\omega,\omega\right)\right) I^2 \tag{1.2.19}$$

As a result, the rate of two-photon absorption has a quadratic dependence on intensity and a linear dependence on the imaginary $\chi^{(3)}$.

1.2.4 Second Harmonic Generation

The second-order nonlinear optical polarization is induced when the second-order nonlinear optical susceptibility is not zero. Assuming a monochromatic electric field strength of a laser is characterized as $E(t)=E\cos\omega t$, the second-order nonlinear optical polarization can be expressed as (Boyd 2008):

$$\begin{aligned} \boldsymbol{P}^{(2)} &= \varepsilon_0 \chi^{(2)} : \boldsymbol{EE} \\ P^{(2)}(t) &= \varepsilon_\circ \chi^{(2)} E(t)^2 \\ &= \varepsilon_\circ \chi^{(2)} \left(E\cos\omega t\right)^2 \\ &= \frac{1}{2}\varepsilon_\circ \chi^{(2)} E^2 \cos 2\omega t + \frac{1}{2}\varepsilon_\circ \chi^{(2)} E^2 \end{aligned} \tag{1.2.20}$$

The first contribution in the second-order nonlinear optical polarization expression with 2ω leads to light emitting at the second harmonic frequency of the laser. Second harmonic generation occurs when two photons of frequency ω nonlinearly scatter generating the emission of a single photon at twice the frequency of the incident photons. SHG involves an intermediate virtual

energy level and as a result, absorption of the fundamental laser frequency does not occur. The second contribution in the second-order nonlinear optical polarization expression leads to the optical rectification process in which a static electric field is created within a nonlinear crystal.

SHG only occurs in noncentrosymmetric material since media with inversion symmetry have a zero second-order nonlinear optical susceptibility. For media with inversion symmetry, a change in the applied electric field results in a change in the sign of the second-order nonlinear optical polarization (Boyd 2008):

$$\begin{aligned} -P^{(2)}(t) &= \varepsilon_{\circ}\chi^{(2)}\left[-E(t)\right]^2 \\ &= \varepsilon_{\circ}\chi^{(2)}E(t)^2 \end{aligned} \tag{1.2.21}$$

The above expression is only valid when the second-order nonlinear optical susceptibility is zero. Therefore, SHG is prohibited in media with centrosymmetric symmetry.

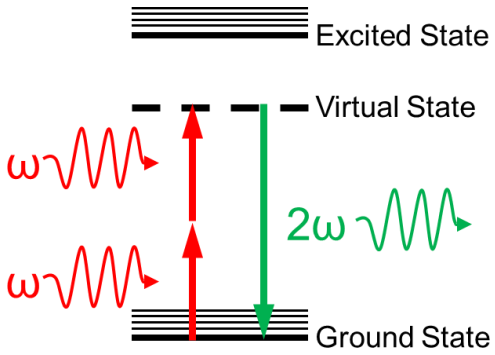

Figure 1.2.2: Second harmonic generation. Energy level schematic diagrams of second harmonic generation (2ω).

1.2.5 Third Harmonic Generation

The third-order nonlinear optical polarization is induced when the third-order nonlinear optical susceptibility is not zero (Boyd 2008):

$$\begin{aligned} \boldsymbol{P}^{(2)} &= \varepsilon_0\chi^{(3)} : \boldsymbol{EEE} \\ &= \varepsilon_{\circ}\chi^{(3)}E^3\cos^3\omega t \\ &= \varepsilon_{\circ}\chi^{(3)}E^3\left(\frac{1}{4}\cos 3\omega t + \frac{3}{4}\cos\omega t\right) \\ &= \frac{3}{4}\varepsilon_{\circ}\chi^{(3)}E^3\cos\omega t + \frac{1}{4}\varepsilon_{\circ}\chi^{(3)}E^3\cos 3\omega t \end{aligned} \tag{1.2.22}$$

The first contribution in the third-order nonlinear optical polarization expression leads to a nonlinear contribution to the index of refraction by the frequency of the incident electric field. When the electric field strength is high, refractive index is expressed as (Boyd 2008):

$$n = n_{\circ} + n_2 I \tag{1.2.23}$$

where n_0 is the linear refractive index, I is the intensity of the laser and n_2 is the nonlinear refractive index expressed as (Boyd 2008):

$$n_2 = \frac{3}{2n_{\circ}^2 \varepsilon_{\circ} c} \chi^{(3)} \tag{1.2.24}$$

If a laser beam of light with a non-uniform transverse intensity distribution propagates through media in which the nonlinear refractive index is positive, self-focusing can occur where the media acts as a lens, causing rays of light to curve creating a focal spot. The resulting focused beam can damage the material.

The second contribution in the third-order nonlinear optical polarization expression (equation (1.2.22)) containing 3ω leads to light emission at the third harmonic frequency of the laser. Similar to SHG, THG occurs via three photons of frequency ω which nonlinearly scatter photons at thrice the frequency of the incident photons. THG can be generated via virtual energy levels and thus, absorption at the fundamental laser frequency or the second and the third harmonic frequency may not occur.

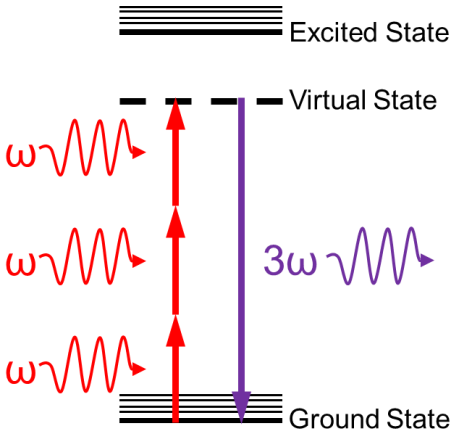

Figure 1.2.3: Third harmonic generation. Energy level schematic diagrams of third harmonic generation (3ω).

The nonlinear optical wave equation as applied to third-order nonlinear optical polarization results in the following wave equation for THG (Boyd 2008):

$$2ik_{3\omega}\frac{\partial A_{3\omega}}{\partial z}+\nabla^2 A_{3\omega}=-\frac{(3\omega)^2}{c^2}\chi^{(3)}A_{\omega}^3 e^{i\Delta kz} \tag{1.2.25}$$

where $A_{3\omega}$ is the amplitude of the generated third harmonic electric field, A_{ω} is the amplitude of the fundamental electric field, and the wave-vector mismatch between the excitation field and the emitted third harmonic field is (Boyd 2008):

$$\Delta k=3k_{\omega}-k_{3\omega}=6\pi\frac{n_{\omega}-n_{3\omega}}{\lambda} \tag{1.2.26}$$

The wave-vector mismatch is representative of the phase difference between the generated third harmonic field and the excitation field as a result of dispersion.

Further, since THG measurements were performed with a focused Gaussian laser beam, the fundamental field and the generated third harmonic field can be assumed to have a Gaussian spatial profile (Boyd 2008):

$$A_{n\omega}(r,z)=\frac{A_{n\omega}(z)}{1+2i\frac{z}{b}}e^{-r^2/w_{\circ}^2\left(1+2i\frac{z}{b}\right)} \tag{1.2.27}$$

where $w_{\circ}$ is the radius of the laser beam waist and b is the confocal parameter of the Gaussian beam.

The confocal parameter of the focused laser beam, b, is a measure of the longitudinal extent of the laser focus and b is related to the beam waist radius by the following equation (Clay, Millard et al. 2006):

$$b=2\pi n_{\lambda}\frac{w_{\circ}^2}{\lambda}=\frac{2n_{\omega}\lambda}{\pi}\frac{\left(n_{\omega}^2-NA^2\right)}{NA^2} \tag{1.2.28}$$

where *NA* is the numerical aperture of the focusing laser beam. The numerical aperture is related to the half cone angle (θ) of the focusing laser beam and the index of refraction by the following equation:

$$NA = n_{\omega} \sin\theta \tag{1.2.29}$$

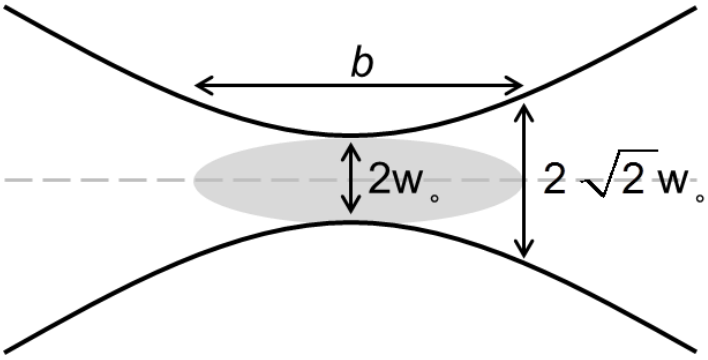

Figure 1.2.4: Confocal parameter of a focused Gaussian laser beam. The confocal parameter (*b*) is a measure of the longitudinal extent of the laser focus.

An approximation is made to equation (1.2.25) called the constant pump approximation which assumes that there is no depletion of the fundamental input field. Therefore, it is assumed that the amplitude is constant where $A_{3\omega}$ is a function of z. Substituting equation (1.2.27) into equation (1.2.25) and integrating over z, the amplitude of the generated third harmonic electric field can be expressed as (Boyd 2008):

$$A_{3\omega}(z) = \frac{i3\omega}{2n_{3\omega}c}\chi^{(3)}A_{\omega}^{3}J(\Delta k, z_{\circ}, z) \tag{1.2.30}$$

where A_{ω} is the amplitude of the fundamental electric field and *J* is the phase-matching integral expressed as (Boyd 2008):

$$J = \int_{z_{\circ}}^{z} \frac{e^{i\Delta kz}}{\left(1+\frac{i2z}{b}\right)^{2}} \tag{1.2.31}$$

The lower limit of the phase-matching integral, z_o, is the entrance of a nonlinear medium while the upper limit, *z*, is the outlet of the nonlinear medium. For the case of a tightly focused

laser beam in a nonlinear medium, the phase-matching integral is zero for $\Delta k \leq 0$ (normal dispersion) whereas for $\Delta k > 0$ (electronic resonance), the phase-matching integral is nonzero.

Since the phase-matching integral is zero for all normally dispersive media, the THG cannot be obtained from bulk media with the use of a tightly focused laser beam. Instead, a positive wave-vector mismatch is necessary for efficient THG. The cancellation of THG in the far field by use of a tightly focused laser beam in normally dispersive bulk media can be understood from the Gouy shift also known as the phase anomaly (Boyd 2008). As the laser beam travels through its focus, it experiences a phase change of 180° (Boyd 2008). The phase shift causes the THG produced on one side of the focus to destructively interfere with the THG produced on the opposite side of the focus therefore, canceling THG signal in the far-field. However, THG can be observed when focal symmetry is broken by introducing an interface of two materials with different refractive indices or third-order nonlinear optical susceptibilities. Although THG can only be collected from an interface, THG is a volume effect as it is generated by bulk media on each side of the interface (Tsang 1995).

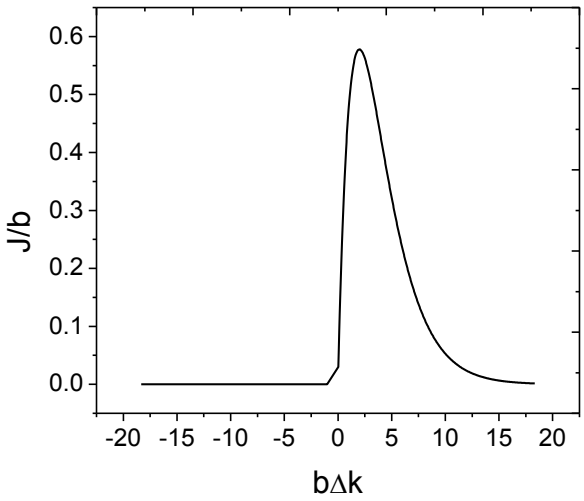

Figure 1.2.5: Modeled behavior of the phase-matching integral. The values of $b\,\Delta\,k$ was varied by keeping $n_{3\omega}$ constant (1.4946) and varying n_{ω} from 1.4632 to 1.5260 in order to demonstrate materials with normal dispersion, no dispersion, and anomalous dispersion. The calculations were performed in MATLAB.

Hypothetically, if one was interested in studying an interface made from two materials with the same dispersion characteristics, but different $\chi^{(3)}$ values, the THG intensity generated

from the interface between the two materials would be proportional to the squared difference in $\chi^{(3)}$ values (Sreedharanpillai 2006). However, in practice, many materials do not have the same dispersion properties and therefore in such cases, it is the squared difference in the products of $\chi^{(3)} \times J$ that determine the magnitude of the THG intensity (Sreedharanpillai 2006).

The magnitude of the phase-matching integral is also largely dependent upon the integration limit. The magnitude of the phase-matching integral largely fluctuates for nonlinear optical materials smaller than 100 μm in thickness. However, it can be assumed that the limit of integration is infinity for nonlinear optical materials whose thicknesses are larger than 100 μm as shown below in Figure 1.2.6.

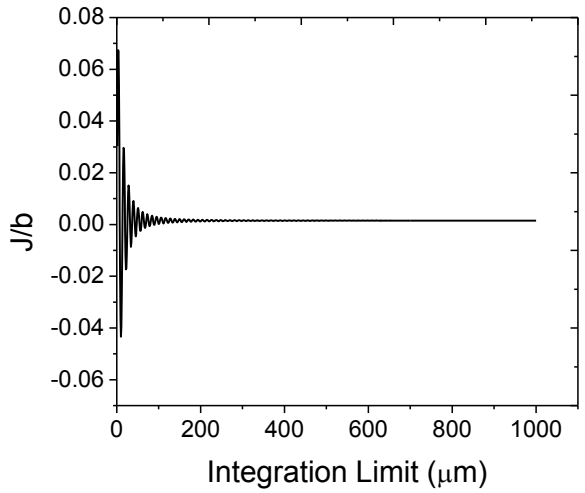

Figure 1.2.6: Effect of integration limit on the magnitude of the phase-matching integral. The values of $n_{3\omega}$ and n_{ω} were kept constant and assumed to be the refractive indices of borosilicate glass (1.4946 and 1.4632) while the integration limit of the phase-matching integral was varied from 0 to 1000 μm. The calculations were performed in MATLAB.

1.2.6 Resonance Enhancement

THG does not require real electronic states however, if real electronic states are present at the fundamental, second harmonic or third harmonic wavelength, then THG can be resonantly enhanced. As a result, $\chi^{(3)}$ is the sum of non-resonant and resonant $\chi^{(3)}$ contributions (Boyd 2008):

$$\chi^{(3)}_{total} = \chi^{(3)}_{non-resonant} + \chi^{(3)}_{resonant} \tag{1.2.32}$$

The third-order nonlinear optical susceptibility descriptive of third harmonic generation representing three-photon resonance where it is assumed that all molecules are initially in the ground state (represented by Figure 1.2.7) is (Boyd 2008):

$$\chi^{(3)}_{kjih}(3\omega,\omega,\omega,\omega)=\frac{N}{\varepsilon_\circ\hbar^3}\sum_{nm}\frac{\mu^k_{0v}\mu^j_{vn}\mu^i_{nm}\mu^h_{m0}}{\left[(\omega_{v0}-3\omega)-i\Gamma_{v0}\right]\left[(\omega_{n0}-2\omega)-i\Gamma_{n0}\right]\left[(\omega_{m0}-\omega)-i\Gamma_{m0}\right]} \quad (1.2.33)$$

where N is the number of molecules, μ is the electric dipole transition moment, and Γ is the damping coefficient. The indices (m, n, v) indicate different electronic states and 0 is the ground state.

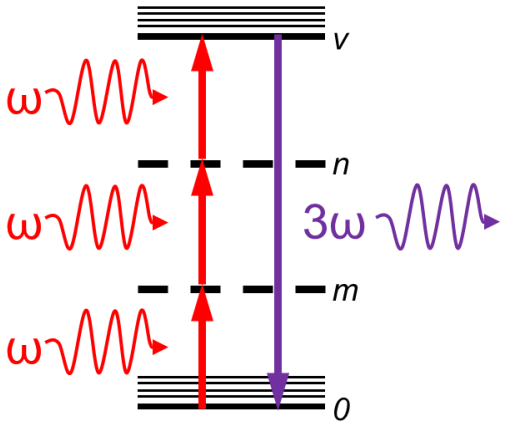

Figure 1.2.7: Third harmonic generation representing three-photon resonance where it is assumed that all molecules are initially in the ground state.

The symmetry rules indicative of one-photon absorption also apply to three-photon absorption. Both processes are odd-parity processes. Therefore, linear absorption at fundamental and third harmonic frequencies will indicate whether one-photon and three-photon resonance will occur. Caution should be applied when studying optical properties of such materials, as one-photon absorption by the material will absorb the incoming fundamental light and three-photon absorption by the material will absorb the outgoing generated third harmonic.

1.3 Molecular Properties for Optimal Harmonic Generation

1.3.1 Harmonophores for Second Harmonic Generation

Organic conjugated π electron molecules have been found to exhibit large first hyperpolarizability values (Nalwa 1991). Delocalized π electrons respond more freely to an applied optical field than σ electrons, which results in larger linear optical responses as well as

larger nonlinear optical responses (Boyd 2008). In particular, β values are large for compounds with asymmetric charge distributions (Long 1995). Such compounds contain electron-donor and electron-acceptor groups. Many SHG harmonophores consist of donor-acceptor derivatives of benzene, stilbene and other analogous systems (Nalwa 1991). Significant enhancement can be achieved by extending the conjugation length present between electron-donor and electron-acceptor groups (Long 1995).

One major requirement necessary for SHG harmonophores is that they must be noncentrosymmetric and the crystal structure packing of the harmonophores must have no inversion symmetry. Since there are no inherent symmetry restrictions for third-order nonlinear optical effects, hence the structure of harmonophores for THG has less symmetry constraints.

1.3.2 Harmonophores for Third Harmonic Generation

Similar to second harmonic generation, third harmonic generation is enhanced by conjugated molecules. Theoretical calculations modeling the behavior of π electrons in a conjugated polymer where π electrons were free to move in a one-dimensional square well potential consisting of the length of the polymer were performed by Rustagi and Ducuing (Rustagi and Ducuing 1974). Results demonstrated that the second hyperpolarizability increases with a fifth power dependence on the length of the polymer (Rustagi and Ducuing 1974):

$$\gamma = \frac{256L^5}{45a_\circ^3 e^2 \pi^6 N^5} \tag{1.3.1}$$

where L is the length of the polymer, a_o is the Bohr radius, e is the charge of the electron, and N is the number of electrons per unit length.

J.P. Hermann and J. Ducuing confirmed this behavior of γ with increasing number of conjugated double bonds in varying lengths of polyenes (Hermann and Ducuing 1974). Therefore, conjugated organic molecules are good candidates for harmonophores. In particular, β-carotene has been previously studied (Hermann, Ricard et al. 1973) and referred to as a standard for γ measurements.

In addition to conjugated organic molecules, inorganic molecules can also be manipulated to optimize γ. For instance, the d orbitals of transition metals can interact with a

conjugated organic ligand thus extending π electron delocalization (Long 1995). Further, enhancement of γ can be readily achieved by varying the ligand. Examples of inorganic complexes with large third-order nonlinear optical properties include porphyrin and phthalocyanine metal complexes (Nalwa 1991, Long 1995).

Since there are no symmetry restrictions for harmonophores generating third-order nonlinear optical effects, the focus of this thesis will be on studying labels for third harmonic generation. The next section of the thesis will describe a technique by which the second hyperpolarizability of harmonophores can be measured. Further chapters include the investigation of carotenoids and chlorophylls as THG labels for biological systems.

Chapter 2
Harmonophore Characterization Techniques[1]

2.1 THG Ratio Measurement Technique

2.1.1 Introduction

Many techniques have been previously used to characterize the third-order nonlinear optical susceptibility of materials. In particular, the third-order nonlinear optical susceptibility has been found by the Maker fringe technique (Maker, Savage et al. 1962, Meredith, Buchalter et al. 1983, Meredith, Buchalter et al. 1983), z-scan (Sheik-Bahae, Said et al. 1990), four-wave mixing, and the optical Kerr effect (Mayer and Gires 1964).

Recently, a new method for determining the third-order susceptibility referred to as the THG ratio technique has been introduced (Barad, Eisenberg et al. 1997, Barille, Canioni et al. 2002, Veres, Matsumoto et al. 2002, Shcheslavskiy, Petrov et al. 2003, Clay, Millard et al. 2006, Pillai, Brakenhoff et al. 2006). This technique is advantageous as it can be used to obtain the third-order nonlinear optical susceptibility values within a harmonic generation microscope. Limitations with the older techniques such as the Maker fringe technique and the z-scan technique include the requirement for high light intensities and large refractive index dispersion to detect signal (Samoc, Samoc et al. 1998). With four-wave mixing, separation of $\chi^{(3)}$ into its real and imaginary components is required and extra experiments are needed to do this (Samoc, Samoc et al. 1998). As well, four-wave mixing is typically only used for films whereas the THG ratio technique can be applied for films or solutions. Lastly, the Maker fringe technique, z-scan, four-wave mixing, and the optical Kerr effect require concentrated samples (with the exception when at resonance), whereas low concentrations of solution can be used with the THG ratio technique.

---

[1]Parts of the following chapter were adapted from a published paper. Reprinted from Analytica Chimica Acta, 755, Tokarz, D., Cisek, R., Prent, N., Fekl, U., and Barzda, V. Measuring the molecular second hyperpolarizability in absorptive solutions by the third harmonic generation ratio technique, 86-92, Copyright (2012), with permission from Elsevier. The specific contributions made by all authors are presented in the Statement of Contributions section on page 142.

In this chapter, the implementation of the THG ratio technique in a nonlinear optical microscope is described. In the past, the THG ratio technique has been applied to non-absorbing materials (Barad, Eisenberg et al. 1997, Barille, Canioni et al. 2002, Veres, Matsumoto et al. 2002, Shcheslavskiy, Petrov et al. 2003, Pillai, Brakenhoff et al. 2006). However, this method can also be used to accurately determine the third-order nonlinear optical susceptibilities of absorbing materials if the refractive index of the material is known at both the fundamental laser wavelength and the third harmonic wavelength (Clay, Millard et al. 2006). Equipment for an ultraviolet to near-infrared range tunable refractometer was not available. Therefore, the second section in this chapter describes the development of a refractometer.

The second hyperpolarizability values were determined for non-absorbing biological harmonophores. It will be demonstrated that the refractive index at the fundamental and third harmonic wavelength can be assumed to be the same as the solvent as long as the harmonophores do not absorb. Examples of second hyperpolarizability determination in absorbing solutions will be demonstrated in Chapters 3 and 4 with the study of carotenoids and chlorophylls as harmonophores.

The second hyperpolarizability is measured by dissolving a harmonophore in solution and therefore, the harmonophore is presumed to have an isotropic orientation. However, many instances in nature exist where harmonophores are present as crystalline aggregates. Therefore, at the end of this chapter, details pertaining to a method used to provide structural details based on crystallinity and orientation of the sample referred to as polarization-in, polarization-out SHG and THG microscopy is described. In Chapter 3, the organizational structures of carotenoid aggregates are investigated with polarization-dependent SHG and THG microscopy.

2.1.2 Underlying Principles of the THG Ratio Technique

In order to calculate the $\chi^{(3)}$ value of a solution, the ratio of THG intensities at two interfaces are measured where one interface is used as a reference. In the experimental setup, four interfaces from a glass capillary tube filled with solution can be studied including an air-glass, glass-solution, solution-glass, and glass-air interface. The laser is focused with a microscope objective onto an interface and the THG intensity from each interface is collected.

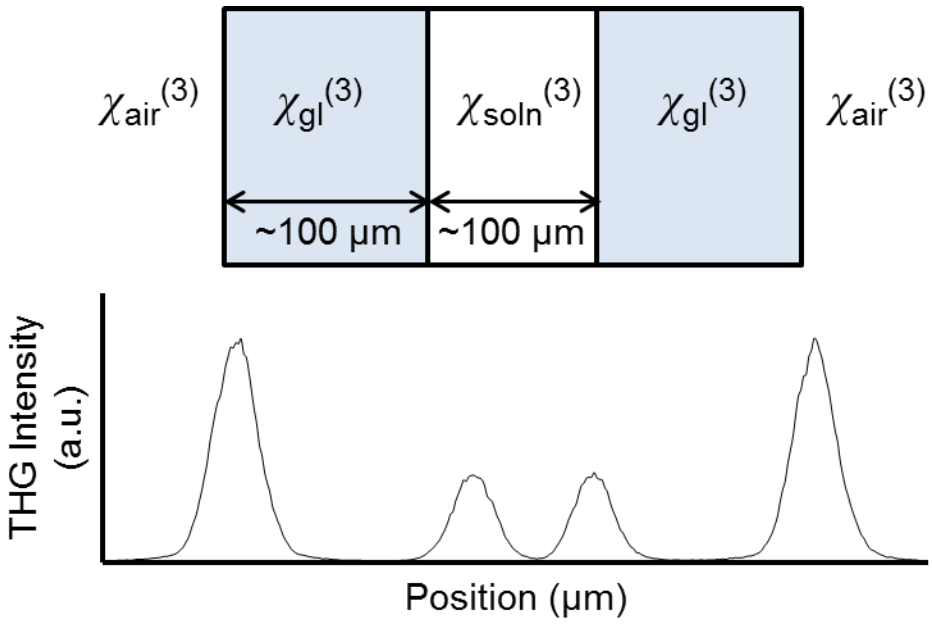

Figure 2.1.1: Glass capillary tube configuration for $\chi^{(3)}$ measurements. A capillary tube revealing four interfaces for THG studies: an air-glass, glass-solution, solution-glass, and glass-air interface. The laser beam is propagating from left to right.

The intensity of the fundamental laser beam (I_ω) can be expressed as (Boyd 2008):

$$I_\omega = 2n_\omega \varepsilon_\circ c \left|A_\omega\right|^2 \tag{2.1.1}$$

where A_ω is the amplitude of the fundamental electric field.

Similarly, the intensity of the generated third harmonic ($I_{3\omega}$) can be expressed as (Boyd 2008):

$$I_{3\omega} = 2n_{3\omega} \varepsilon_\circ c \left|A_{3\omega}\right|^2 \tag{2.1.2}$$

where $A_{3\omega}$ is the amplitude of the generated third harmonic electric field which can be represented as (Boyd 2008):

$$A_{3\omega}(z) = \frac{i3\omega}{2n_{3\omega}} \chi^{(3)} A_\omega^3 J_3(\Delta k, z_\circ, z) \tag{2.1.3}$$

Therefore, the third harmonic intensity can be expressed as:

$$I_{3\omega} = 2n_{3\omega}\varepsilon_{\circ}c\left|\frac{i3\omega}{2n_{3\omega}}\chi^{(3)}A_{\omega}^{3}J_{3}\left(\Delta k, z_{\circ}, z\right)\right|^{2} \tag{2.1.4}$$

The amplitude of the fundamental electric field can be expressed as a function of the fundamental laser intensity:

$$\left|A_{\omega}\right| = \sqrt{\frac{I_{\omega}}{2n_{\omega}\varepsilon_{\circ}c}} \tag{2.1.5}$$

where this equation can be substituted into the expression for the amplitude of the generated third harmonic electric field (equation (2.1.3)):

$$\begin{aligned} I_{3\omega} &= \frac{n_{3\omega}}{8n_{\omega}^{3}\varepsilon_{\circ}^{2}c^{2}}\left|\frac{i3\omega}{2n_{3\omega}}\chi^{(3)}J_{3}\left(\Delta k, z_{\circ}, z\right)\right|^{2} I_{\omega}^{3} \\ I_{3\omega} &\propto \frac{n_{3\omega}}{n_{\omega}^{3}}\left|\frac{1}{n_{3\omega}}\chi^{(3)}J_{3}\left(\Delta k, z_{\circ}, z\right)\right|^{2} I_{\omega}^{3} \end{aligned} \tag{2.1.6}$$

At the air-glass interface ($I_{3\omega\text{air-gl}}$), the THG intensity can be expressed as:

$$I_{3\omega\text{air-gl}} \propto \frac{n_{3\omega\text{gl}}}{n_{\omega\text{air}}^{3}}\left|\frac{1}{n_{3\omega\text{air}}}\chi^{(3)}J_{\text{air}}\left(\Delta k, z_{\circ}, z\right)+\frac{1}{n_{3\omega\text{gl}}}\chi^{(3)}J_{\text{gl}}\left(\Delta k, z_{\circ}, z\right)\right|^{2} I_{\omega}^{3} \tag{2.1.7}$$

where n_{air} is the refractive index of air assumed to be equal to 1 at both fundamental and third harmonic wavelengths, n_{gl} is the refractive index of glass and J_{air} and J_{gl} expresses the phase-matching integrals for air and glass, respectively. The THG intensity of the air-glass interface can be assumed to be completely due to the $\chi^{(3)}$ and dispersion properties of glass since the $\chi^{(3)}$ of air is 3 orders of magnitude lower than the $\chi^{(3)}$ of glass (Boyd 2008). As a result, the expression for $I_{3\omega\text{air-gl}}$ is reduced to:

$$I_{3\omega\text{air-gl}} \propto n_{3\omega\text{gl}}\left|\frac{1}{n_{3\omega\text{gl}}}\chi^{(3)}J_{\text{gl}}\left(\Delta k, z_{\circ}, z\right)\right|^{2} I_{\omega}^{3} \tag{2.1.8}$$

The THG intensity of the glass-solution interface ($I_{3\omega\text{gl-soln}}$) can be represented as the summation contributions from the glass and solution separately:

$$I_{3\omega\text{gl-soln}} \propto \frac{n_{3\omega\text{soln}}}{n_{\omega\text{gl}}^3}\left|\frac{1}{n_{3\omega\text{soln}}}\chi_{\text{soln}}^{(3)}J_{\text{soln}}\left(\Delta k, z_\circ, z\right)+\frac{1}{n_{3\omega\text{gl}}}\chi_{\text{gl}}^{(3)}J_{\text{gl}}\left(\Delta k, z_\circ, z\right)\right|^2 I_\omega^3 \qquad (2.1.9)$$

where n_{soln} is the refractive index of the solution and J_{soln} expresses the phase-matching integral for the solution.

Therefore, the resulting equation expressing the THG intensity ratio by Shcheslavskiy et al. was used (Reintjes 1984, Shcheslavskiy, Petrov et al. 2003):

$$\frac{I_{3\omega\text{gl-soln}}}{I_{3\omega\text{air-gl}}} = \frac{1}{n_{\omega\text{gl}}^3 n_{3\omega\text{gl}} n_{3\omega\text{soln}}} \times \frac{\left|n_{3\omega\text{soln}}\chi_{\text{gl}}^{(3)}J_{\text{gl}} + n_{3\omega\text{gl}}\chi_{\text{soln}}^{(3)}J_{\text{soln}}\right|^2}{\left|\chi_{\text{gl}}^{(3)}\right|^2\left|J_{\text{gl}}\right|^2} \qquad (2.1.10)$$

Similar equations to equation (2.1.10) have also been published (Barad, Eisenberg et al. 1997, Barille, Canioni et al. 2002, Veres, Matsumoto et al. 2002, Clay, Millard et al. 2006) however, this specific equation was chosen because correction of spherical aberrations was not necessary as a low NA objective was used in this experiment. Further, the other equations also showed similar trends in $\chi^{(3)}$ to the solutions studied (Barad, Eisenberg et al. 1997, Barille, Canioni et al. 2002, Clay, Millard et al. 2006).

2.1.3 $\chi^{(3)}$ and γ Relation

The third-order nonlinear optical susceptibility of an isotropic material (e.g. a solution) has only one unique element, $\chi^{(3)}_{xxxx}$, which is proportional to the summation over second hyperpolarizability elements:

$$\chi_{xxxx}^{(3)} = f^{(3)}N\frac{1}{5}\left(\gamma_{xxxx}+\gamma_{yyyy}+\gamma_{zzzz}+\gamma_{xxyy}+\gamma_{xxzz}+\gamma_{yyxx}+\gamma_{yyzz}+\gamma_{zzxx}+\gamma_{zzyy}\right) \qquad (2.1.11)$$

where summation under repeated indexes is implied.

The $\chi^{(3)}$ of a solution can be described by the following relation (Kajzar and Messier 1985):

$$\chi^{(3)} = \left(\frac{n_\omega^2+2}{3}\right)^3\left(\frac{n_{3\omega}^2+2}{3}\right)\left(N_s\gamma_s + N_{sol}\gamma_{sol}\right) \qquad (2.1.12)$$

where n_ω is the refractive index of the solution at the fundamental wavelength, $n_{3\omega}$ is the refractive index of the solution at the third harmonic wavelength, the subscript "s" refers to solute and the subscript "*sol*" refers to the solvent, N is the number density of molecules, and $\langle\gamma\rangle$ refers to the unique isotropic description of the second hyperpolarizability of a single molecule via:

$$\langle\gamma\rangle = \frac{1}{5}\left(\gamma_{xxxx} + \gamma_{yyyy} + \gamma_{zzzz} + \gamma_{xxyy} + \gamma_{xxzz} + \gamma_{yyxx} + \gamma_{yyzz} + \gamma_{zzxx} + \gamma_{zzyy}\right) \tag{2.1.13}$$

By substituting for the number density of solute and solvent molecules in solution (equation (2.1.12)) one obtains the following equation, which allows for the extraction of the γ value of the solute if the $\chi^{(3)}$ of solutions are measured at a number of concentrations along with the refractive index at the fundamental and third harmonic wavelengths:

$$\chi^{(3)}(C) = \left(\frac{n_\omega^2 + 2}{3}\right)^3 \left(\frac{n_{3\omega}^2 + 2}{3}\right)\left(\frac{N_A \rho}{1 + C}\right)\left(C\frac{\gamma_s}{M_s} + \frac{\gamma_{sol}}{M_{sol}}\right) \tag{2.1.14}$$

where C is concentration expressed as the ratio of the weight of the solute molecules to the weight of solvent molecules, ρ is the density of the solution approximated as the density of the solvent, M_s and M_{sol} are the molecular masses of the solute and solvent, respectively.

If the solutions are dilute (~mM concentration), then it can be assumed that $(1+C)\sim 1$. As a result, the $\chi^{(3)}$ of a solution increases linearly with concentration:

$$\chi^{(3)}(C) = \left(\frac{n_\omega^2 + 2}{3}\right)^3 \left(\frac{n_{3\omega}^2 + 2}{3}\right) N_A \rho \left(C\frac{\gamma_s}{M_s} + \frac{\gamma_{sol}}{M_{sol}}\right) \tag{2.1.15}$$

Thus, in order to extract the γ values of harmonophores, plots consisting of the $\chi^{(3)}$ values versus concentration were fit with equation (2.1.14) similar to previous experiments done by Tykwinski et al. (Tykwinski, Gubler et al. 1998). However, caution must be taken when analyzing $\chi^{(3)}$ data. Since $\chi^{(3)}$ values are calculated using a quadratic equation (equation (2.1.10)), there are two possible roots for the $\chi^{(3)}$ value where one is solved using subtraction and a second is solved using addition in the quadratic equation. Trends in the two roots for $\chi^{(3)}$ values of aqueous NaCl solutions versus concentration are shown in Figure 2.1.2.

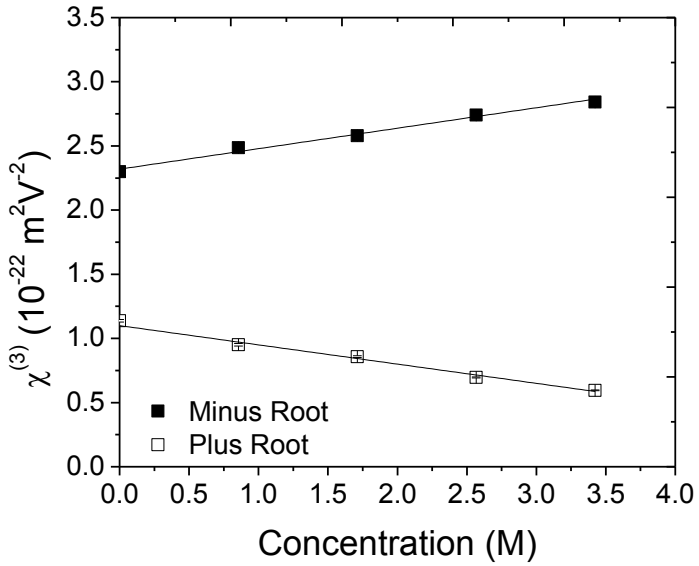

Figure 2.1.2: The third-order nonlinear susceptibility of aqueous NaCl solutions versus concentration. Two distinct roots of the quadratic equation for finding the $\chi^{(3)}$ values of aqueous NaCl solutions are shown. One set of data represents the 'minus root' solution where subtraction is used in the quadratic equation and the second set of data represents the 'plus root' where addition is used in the quadratic equation. Note that the error bars are too small to be seen having a magnitude of 10^{-24} m^2V^{-2}.

As seen in Figure 2.1.2, the magnitude of the slopes of both the minus root and plus root are both similar however, the direction of the slope indicates whether the phase of the THG emitted from the solute is in or out of phase with the THG emitted from the solvent. Therefore, it is important to resolve the quadratic equation sign ambiguity. Previous researchers have done this by comparing their experimental values for $\chi^{(3)}$ to previously found literature values as well as taking into account published trends for $\chi^{(3)}$ of solvents (Pillai, Brakenhoff et al. 2006). This problem was overcome by comparing extracted values for the γ of the solvent with previously published measurements.

2.1.4 Nonlinear Optical Microscope Setup

Imaging and $\chi^{(3)}$ measurements were performed with a nonlinear optical multicontrast microscope (Greenhalgh, Prent et al. 2007). The laser source consisted of a tunable titanium-doped sapphire (Ti:Sapphire) crystal based oscillator which provided ~100 fs duration pulses emitting at wavelengths that could be tuned between 773 nm and 830 nm with a pulse repetition rate of 66 MHz. As well, a second laser source was used to provide measurements at 1028 nm wavelength. The second laser consisted of a femtosecond ytterbium-doped potassium gadolinium

tungstate (Yb:KGd$(WO_4)_2$ or referred to as Yb:KGW) crystal based oscillator which provided ~450 fs duration pulses with a pulse repetition rate of 14.3 MHz (Major, Cisek et al. 2009).

The microscope setup is shown in Figure 2.1.3. Both lasers are directed through an optical isolator (715, Conoptics). The optical isolator ensures that back reflections from optics in the microscope do not interfere with the mode locking of the laser. After the optical isolator, two mirrors (M1 and M2) are used to direct the laser into an input port of the microscope. Outside of the microscope box, a long-pass filter (F1) is placed in order to block external light (FEL750, Thorlabs). Additionally, optical density filters are placed outside the microscope in order to reduce the intensity of the laser beam. Inside the microscope, the laser beam is focused through a pinhole (PH) (30 μm, Thorlabs). The PH is used as a spatial filter to achieve a Gaussian beam profile. The PH is placed at the focus of a 1:2 telescope (between L1 and L2) where the telescope magnifies the laser beam to match the size of the scanning mirrors.

The scanning mirrors consist of 10 mm galvanometric mirrors (SC2000 controller with two MiniSax amplifiers and VM1000 galvonometers, GSI Lumonics Inc.) that are able to raster scan the beam at a speed of 10 frames per second for 128×128 pixel mode. A second telescope is placed after the scanning mirrors, consisting of an achromatic lens (L3) and a tube lens (L4) (Zeiss). The second telescope is used to expand the laser beam in order to match the entrance aperture of the excitation objective (EO).

After the second telescope, the laser beam is transmitted through a dichroic mirror (DM1) and then an excitation microscope objective (EO). For imaging, two high numerical aperture objectives were used including a 0.75 NA (Zeiss) air objective and a 1.3 NA (Zeiss) oil objective. The two objectives have working distances of 600 μm and 250 μm, respectively. For $\chi^{(3)}$ measurements of harmonophores dissolved in solutions, a 0.25 NA objective (Zeiss) was used for excitation in order to minimize optical aberrations from higher NA objectives (Pillai, Brakenhoff et al. 2006).

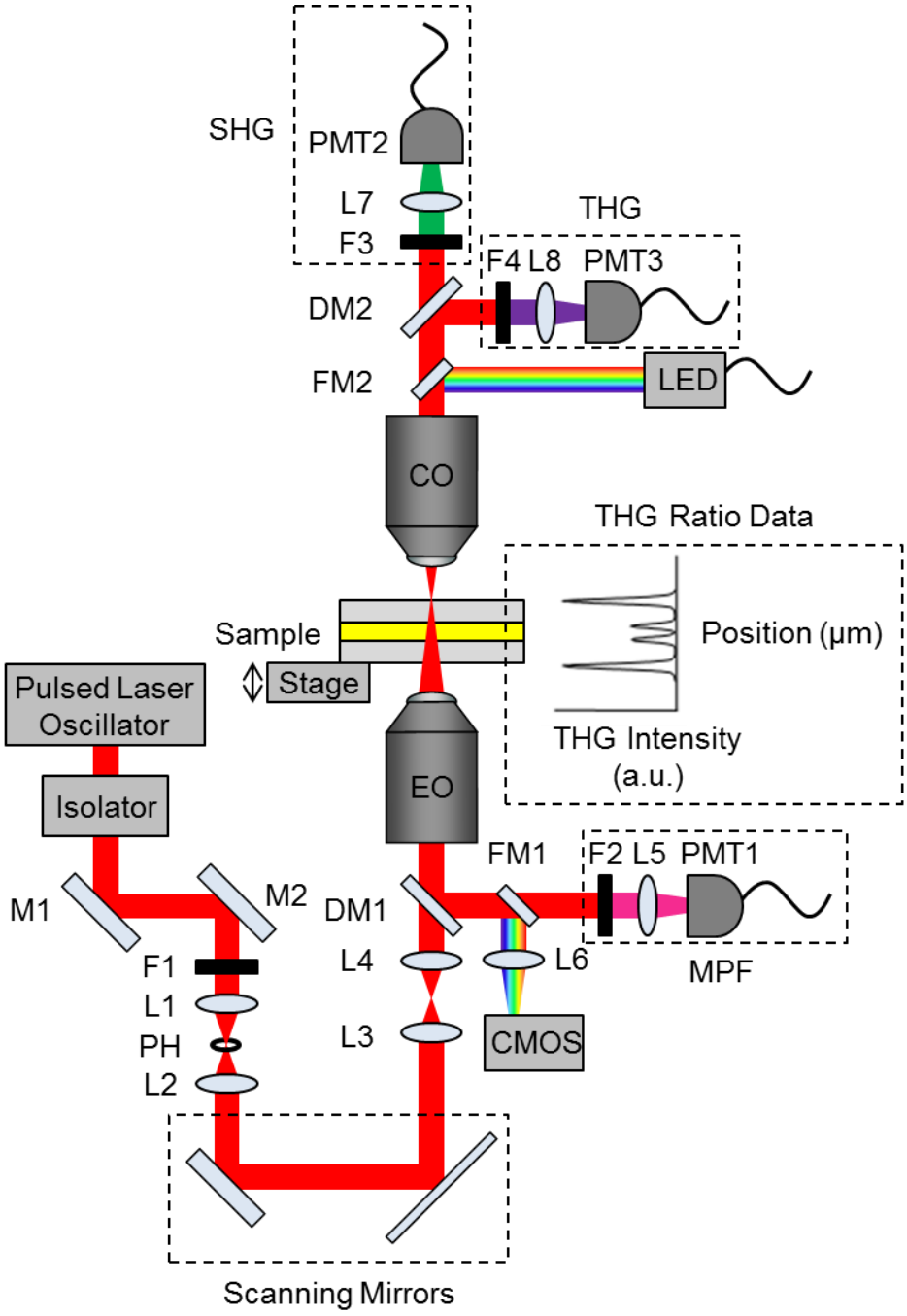

Figure 2.1.3: A nonlinear optical microscope with multimodal detection of MPF, SHG and THG. The nonlinear optical microscope was used to collect THG generated at all interfaces of a capillary tube corresponding to an air-glass, glass-solution, solution-glass, and glass-air interface seen in the graph of THG intensity versus position. The graph is representative of what is recorded with this system. The following abbreviations are used: M-mirror, F-filter, L-lens, PH-pinhole, DM-dichroic mirror, EO-excitation objective, CO- collection objective, PMT-photomultiplier tube, FM-flipping mirror, CMOS-CMOS detector, and LED-white light source. Image not to scale.

MPF, SHG and THG imaging is conducted simultaneously. Epi-detection is used to collect MPF using the same objective for excitation. MPF signals are separated from the fundamental laser with a dichroic mirror (DM1) (565-720 nm, R&G). MPF signals are directed through a band pass interference filter (F2) or color glass filter (dependent upon the emission wavelength range of the fluorophore) and focused by a lens (L5) into a photomultiplier tube detector (PMT1). The photomultiplier tubes are set to photon-counting mode (MPF and SHG: H7421-40, Hamamatsu and THG: MP-1343, Perkin Elmer).

Epi-detection can be used with MPF signals as fluorescence generally produces isotropic emission however; harmonic generation is mostly generated in the forward direction. As a result, harmonic generation signals were collected in the forward direction. Both SHG and THG signals pass through a custom 0.85 NA collection objective (CO) to collimate the resulting signal. In order to separate between SHG and THG, the signals are passed through a dichroic mirror (DM2) (Ti:Sapphire: HT800+400nm, HR266, CVI Melles Griot or Yb:KGW: HT1030+515nm, HR 340nm, CVI Melles Griot).

The SHG signal is filtered with a band pass interference filter (F3) (Ti:Sapphire: F25-400, CVI Melles Griot or Yb:KGW: F10-514.5, CVI Melles Griot) and a color glass filter to block the excitation beam (BG-39, CVI Melles Griot). The THG signal is also filtered with a band pass interference filter (F4) (Ti:Sapphire: F25-265 CVI Melles Griot or Yb:KGW: F10-340, CVI Melles Griot). The SHG and THG signals are focused by lenses (L7 and L8, respectively) onto photomultiplier tubes (PMT2 and PMT3, respectively).

The nonlinear optical microscope is also equipped with white-light imaging capability in order to find a region of interest within a sample. A white illuminator (LED) is directed through the collection objective (CO) via a flipping mirror (FM2) in order to illuminate the sample. The white light is collected by the excitation objective (EO) and directed onto a complementary metal-oxide semiconductor (CMOS) detector via a dichroic mirror (DM1) and another flipping mirror (FM1), and focused by a lens (L6). During laser scanning, both flipping mirrors (FM1 and FM2) are turned away so as to not interfere with the laser.

For $\chi^{(3)}$ measurements, the samples consist of glass capillary tubes (W5010, VitroCom) containing harmonophore solutions. In order to collect THG through the cross-sectional area of a capillary tube (W5010, VitroCom), the sample is translated axially with a piezoelectric

translation stage (400 μm range, Dynamic Structures & Materials, LLC) by a home programmed LabVIEW microscope control interface. This process is referred to as a z-scan. The THG signal generated from the top two interfaces (air-glass and glass-solution) closest to the collection objective are used in the THG ratio technique. As a result, absorption of the solution can be ignored as well as the absorption of glass since the glass transmits the third harmonic wavelength of both lasers.

2.1.5 Third-order Nonlinear Susceptibility Calculations

In order to accurately calculate the third-order nonlinear optical susceptibility of a solution by use of the THG ratio technique, the refractive indices of the solution at the fundamental and third harmonic wavelengths should be known in addition to the THG intensity generated at the air-glass and glass-solution interfaces (see equation (2.1.10)). The refractive indices of many solvents can be found in the literature. However, measurement of THG intensities at the two interfaces requires an experimental procedure where the THG intensity generated from these interfaces during z-scanning are collected and fit with a Gaussian function:

$$y = y_{\circ} + Ae^{-\frac{(x-x_c)^2}{2w^2}} \tag{2.1.16}$$

where y_o is an offset in the y-axis, A is the height of the Gaussian peak, w is the width of the Gaussian curve and x_c is the position of the center of the Gaussian peak. The width of the Gaussian curve is related to the full-width half-maximum (FWHM) by the following relation:

$$\mathrm{FWHM} = 2w\sqrt{\ln 4} \tag{2.1.17}$$

Fitting THG intensity data is performed with a custom LabVIEW program. THG intensity data can be loaded as a text file. An initial guess of the position of the maximum THG intensity is given by moving the cursor to the top of the peak and pressing the ‘Insert’ button. As well, an initial guess for the width of the Gaussian peak is provided in the ‘Width Guess’ box. Once this is done, the ‘Model’ button will fit the original data seen in the top ‘Selected Profile’ graph by using the Levenberg-Marquardt algorithm. The original data is drawn in white with the fitted Gaussian data drawn in red in the ‘Best Fit’ graph below. Multiple datasets can be fit at once.

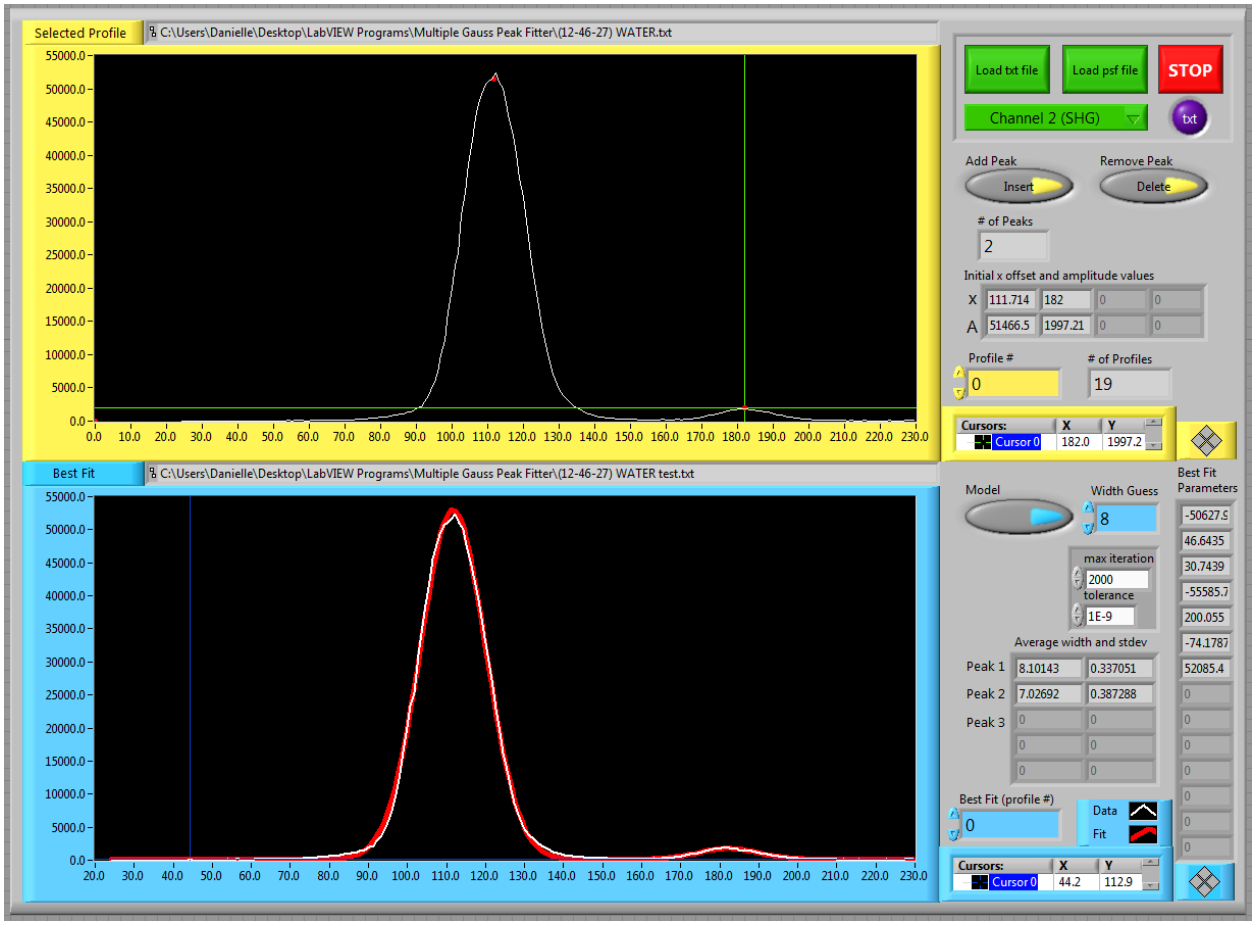

Figure 2.1.4: Multiple peak fitting program in LabVIEW. The LabVIEW program performs a Gaussian fit with the Levenberg-Marquardt algorithm of the THG intensity from the air-glass interface and the glass-water interface in this instance and returns the fitted values. The program was created by Nicole Prent.

The text file generated with the multiple peak fitting program includes the amplitude of the two THG intensity peaks as well as a width term which is related to the FWHM by equation (2.1.17). The confocal parameters used in equation (2.1.10) are determined experimentally by multiplying the FWHM by $\sqrt{3}$. This is done because the volume of a third-order nonlinear optical process decreases by a factor of $\sqrt{3}$ relative to its linear volume (Squier and Muller 2001). The amplitudes and confocal parameters of the air-glass and glass-solution interface data are averaged amongst at least 40 sample scans and the averages of these values are used to calculate $\chi^{(3)}$.

The refractive indices, the THG intensities found by taking the average of the fitted Gaussian amplitudes and the average experimental confocal parameters are entered in a custom

LabVIEW program to calculate $\chi^{(3)}$. The program is capable of calculating the $\chi^{(3)}$ using a number of different equations found in the literature (Barad, Eisenberg et al. 1997, Barille, Canioni et al. 2002, Veres, Matsumoto et al. 2002, Shcheslavskiy, Petrov et al. 2003, Clay, Millard et al. 2006). The program also includes the refractive index values at the third harmonic and fundamental wavelengths for a number of different types of glass.

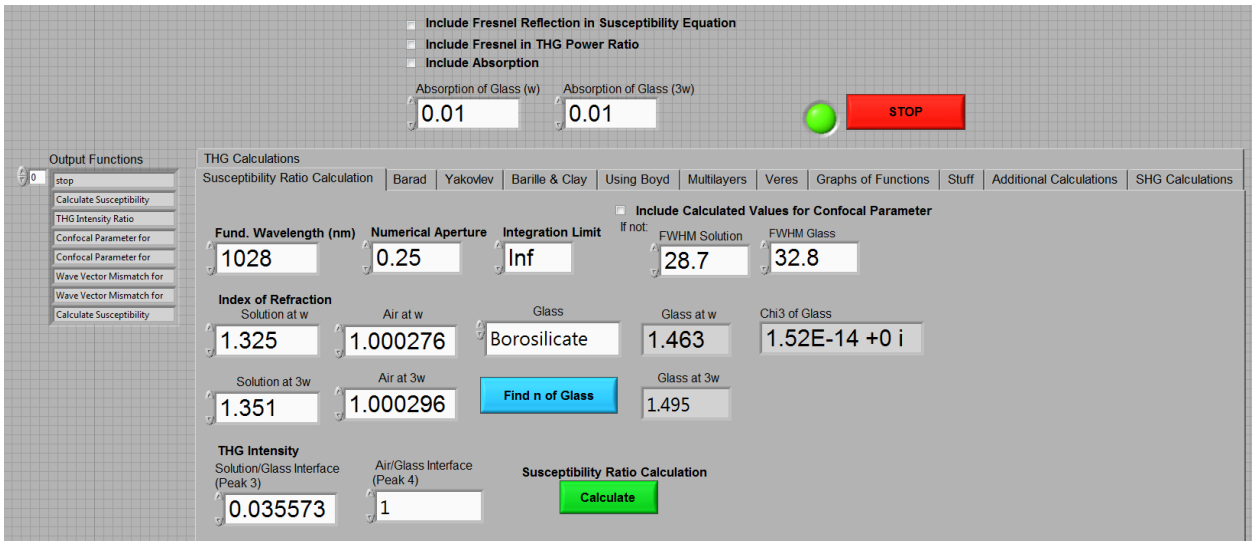

Figure 2.1.5: Third-order nonlinear optical susceptibility program in LabVIEW. The LabVIEW program calculates the third-order nonlinear optical susceptibility using several different equations. The input needed includes the refractive indices at the fundamental and third harmonic wavelengths, the THG intensity at the solution-glass and glass-air interfaces and the confocal parameters which can be added directly or calculated using the program.

Equations used to calculate the phase-matching integrals and the final $\chi^{(3)}$ values were programmed by using MATLAB script nodes in LabVIEW. The phase-matching integral was numerically evaluated using an adaptive Gauss-Kronrod quadrature algorithm. This function was chosen as it is most efficient at solving oscillatory and contour integrands.

2.1.6 Refractive Index of Borosilicate Glass

In order to measure the $\chi^{(3)}$ of solutions using the THG ratio technique, both the refractive indices of the glass and the $\chi^{(3)}$ value of the glass used to make the capillary tubes are needed. SCHOTT-Rohrglas GmbH (personal communications) provided the refractive indices at several wavelengths for the appropriate glass (Duran borosilicate glass) used in the experiments.

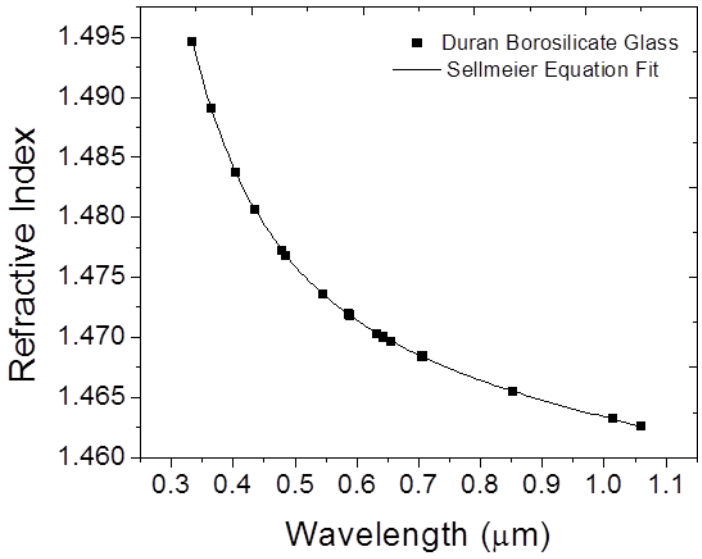

Figure 2.1.6: Refractive index measurements of Duran Borosilicate glass. Refractive indices of Duran Borosilicate glass were fit with a Sellmeier equation and refractive indices for far UV wavelengths were extrapolated from the fit. The adjusted R-squared value was 0.99999. The refractive index of Duran Borosilicate glass was provided by SCHOTT-Rohrglas GmbH (personal communications).

In order to determine the refractive indices at specific wavelengths, the refractive index values provided were plotted against wavelength and fit with a Sellmeier equation:

$$n_\lambda^2 = 1 + \frac{B_1\lambda^2}{\lambda^2 - C_1} + \frac{B_2\lambda^2}{\lambda^2 - C_2} + \frac{B_3\lambda^2}{\lambda^2 - C_3} \tag{2.1.18}$$

where λ is the wavelength of interest expressed in micrometers and B and C are Sellmeier coefficients found in Table 2.1-1which were used to find the refractive index of the glass at desired wavelengths.

Table 2.1-1: The Sellmeier coefficients obtained from fitting refractive indices of Duran Borosilicate glass given by SCHOTT-Rohrglas GmbH (personal communications) with the Sellmeier equation.

Glass	B_1	C_1	B_2	C_2	B_3	C_3
Duran Borosilicate	1.08088	0.00715	0.06091	0.02671	845.01573	86395.64087

The refractive indices of Duran borosilicate glass at the fundamental and third harmonic wavelengths of the Ti:Sapphire and Yb:KGW lasers were calculated using the Sellmeier equation and found to be (where n_ω and $n_{3\omega}$ are expressed as n_λ and $n_{\lambda/3}$): n_{773} =1.4669 and n_{258} =1.5195, n_{830} =1.4659 and n_{277} =1.5115, n_{1028} =1.4632 and n_{343} =1.4946. Although the refractive

indices of Duran Borosilicate glass can be calculated using the Sellmeier equation, THG intensity ratio measurements also require knowledge of the $\chi^{(3)}$ value of the glass. The next section describes a method by which the $\chi^{(3)}$ of Duran Borosilicate glass can be estimated.

2.1.7 Miller's Rule

Miller's rule can be applied to predict the non-resonant $\chi^{(3)}$ values of various media. Specifically, Miller's rule has been shown to be valid for certain ionic crystals (Wynne 1969). Miller's rule is expressed by the following equation (Boyd 2008):

$$\begin{aligned}\chi^{(3)}_{non-resonant}(\omega_4,\omega_3,\omega_2,\omega_1) &\propto \chi^{(1)}(\omega_4)\chi^{(1)}(\omega_3)\chi^{(1)}(\omega_2)\chi^{(1)}(\omega_1)\\ &\propto \left[n^2(\omega_4)-1\right]\left[n^2(\omega_3)-1\right]\left[n^2(\omega_2)-1\right]\left[n^2(\omega_1)-1\right]\end{aligned} \tag{2.1.19}$$

where the general form of this rule can be applied to THG:

$$\begin{aligned}\chi^{(3)}_{non-resonant}(3\omega) &\approx \chi^{(1)}(3\omega)\left[\chi^{(1)}(\omega)\right]^3\\ &\approx \left[n^2_{3\omega}-1\right]\left[n^2_{\omega}-1\right]^3\end{aligned} \tag{2.1.20}$$

Miller's rule can be used to find the $\chi^{(3)}$ of Duran Borosilicate glass as long as the refractive indices at the fundamental and third harmonic wavelengths are known, as well as the known values of $\chi^{(3)}$ and the refractive indices at the fundamental and third harmonic wavelengths of a standard are used.

Fused silica was chosen as the standard where the $\chi^{(3)}$ value at 1064 nm is reported by Bosshard et al. (Bosshard, Gubler et al. 2000) as suggested by Débarre and Beaurepaire (Débarre and Beaurepaire 2007). The $\chi^{(3)}$ value at 1064 nm along with the refractive indices of fused silica at 773 nm, 830 nm and 1028 nm were used to find the $\chi^{(3)}$ of fused silica at the indicated wavelengths. Then, the ratio between the $\chi^{(3)}$ values and the refractive indices of fused silica and Duran borosilicate glass were used to find the $\chi^{(3)}$ values of Duran borosilicate glass at 773 nm, 830 nm and 1028 nm. The $\chi^{(3)}$ of Duran borosilicate glass was found to be $(2.3\pm0.2)\times10^{-22}$ m^2 V^{-2} at 773 nm, $(2.2\pm0.2)\times10^{-22}$ m^2 V^{-2} at 830 nm and $(2.1\pm0.2)\times10^{-22}$ at 1028 nm. These values were used in order to calculate the $\chi^{(3)}$ of harmonophore solutions at 773 nm, 830 nm and 1028 nm.

2.1.8 The Third-Order Nonlinear Susceptibilities of Solvents

The refractive indices of Duran Borosilicate glass, the refractive indices of different solvents provided by literature, and the THG intensities of the air-glass and glass-solution interfaces for glass capillary tubes containing different solvents were used to determine the $\chi^{(3)}$ of a number of solvents. Results are shown in Table 2.1-2.

Table 2.1-2: The third-order nonlinear optical susceptibilities of solvents measured by the THG ratio technique and compared to the third-order nonlinear optical susceptibilities in literature.

Solvent	THG Intensity Ratio (glass-solution/air-glass)	$n_{3\omega}$- n_{ω} for 1064 nm	$\chi^{(3)}$ Literature (10^{-22} m^2V^{-2})	$\chi^{(3)}$ Measured using Refractive Indices for 1064 nm (10^{-22} m^2V^{-2})	$n_{3\omega}$- n_{ω} for 1028 nm	$\chi^{(3)}$ Measured using Refractive Indices for 1028 nm (10^{-22} m^2V^{-2})
Acetone	0.391±0.004	0.050[a]	6.6±0.3[a]	6.5±0.3[a]	0.027[b]	3.8±0.4[b]
Benzene	0.267±0.006	0.130[a]	16.8±0.8[a]	15.3±0.7[a]	0.074[c]	8.8±0.9[c]
Chloroform	0.589±0.004	0.066[a]	9.8±0.5[a]	9.6±0.5[a]	0.035[c]	5.4±0.3[c]
Ethanol	0.213±0.001	0.044[a]	4.8±0.2[a]	5.0±0.2[a]	0.025[b]	3.0±0.2[b]
Water	0.0326±0.0007	0.046[a]	3.9±0.2[a]	3.7±0.2[a]	0.026[d]	2.2±0.2[d]

[a]Refractive index values as well as literature $\chi^{(3)}$ values measured by Kajzar and Messier at 1064 nm (Kajzar and Messier 1985).
[b]Refractive index values for acetone and ethanol at 343 nm and 1028 nm measured by Rheims et al. (Rheims, Koser et al. 1997).
[c]Refractive index values for benzene and chloroform at 343 nm and 1028 nm measured by Samoc (Samoc 2003).
[d]Refractive index values for water at 343 nm and 1028 nm measured by Daimon and Masumura (Daimon and Masumura 2007).

The measured $\chi^{(3)}$ values are within error of the literature $\chi^{(3)}$ values demonstrated by Kajzar and Messier at 1064 nm if the dispersion of the solvents are assumed to be the same. Therefore, the THG ratio technique demonstrates similar results to the Maker fringe method used by Kajzar and Messier to measure $\chi^{(3)}$. However, more recent publications have updated the refractive indices of solvents at UV and infrared (IR) wavelengths. Using these new dispersion values, the $\chi^{(3)}$ values of solvents are smaller than the $\chi^{(3)}$ values reported by Kajzar and Messier.

Débarre and Bearepaire reported the $\chi^{(3)}$ of water at 1064 nm as $(1.83\pm0.1)\times10^{-22}$ m^2 V^{-2} (Débarre and Beaurepaire 2007). The dispersion that the authors used is smaller than the dispersion used for water in Table 2.1-2. When the $\chi^{(3)}$ of water is calculated using the suggested dispersion that the authors used (0.0235), the calculated $\chi^{(3)}$ is within error of the $\chi^{(3)}$ of water reported. Therefore, $\chi^{(3)}$ is sensitive to the difference in refractive index at the fundamental and

third harmonic wavelength and as a result, the development of a refractometer was necessary in order to accurately determine $\chi^{(3)}$ values of harmonophore solutions. The development of a refractometer will be described in the following section.

2.1.9 Conclusions

Similar third-order nonlinear optical susceptibilities of solvents have been found with the implemented THG ratio technique as compared to the Maker fringe method. In order to achieve accurate $\chi^{(3)}$ values, it is important that the $\chi^{(3)}$ of reference glass is known which can be found using Miller's rule and applying previously reported $\chi^{(3)}$ values with known refractive indices of glass. Caution must be taken when reporting $\chi^{(3)}$ values with the THG ratio technique since two possible roots for the $\chi^{(3)}$ value are possible. In order to resolve the quadratic equation sign ambiguity, $\chi^{(3)}$ can be compared to previously found literature values of solvents or alternatively, the γ of the solvent can be compared to literature. In order to calculate γ values of harmonophores, measurements of the change in $\chi^{(3)}$ values with the change in harmonophore concentration is needed. Lastly, $\chi^{(3)}$ was shown to be sensitive to the difference in refractive index at the fundamental and third harmonic wavelength and as a result, the development of a refractometer is necessary in order to accurately determine $\chi^{(3)}$ values.

2.2 Tunable Refractometer for Improved Hyperpolarizability Measurements

2.2.1 The Working Principles of a Refractometer

The Abbe refractometer was the first commercial refractometer developed and is still commonly used today for measuring the refractive index of a sample at the sodium D line (589.3 nm) (Abbe 1873, Rheims, Koser et al. 1997). The Abbe refractometer is based on the principle of total internal reflection where a sample is placed between two highly refractive glass prisms (Abbe 1873, Rheims, Koser et al. 1997).

Light passes through the bottom prism (illumination prism) to the interface of the sample. The surface of the illuminating prism is matted and as a result, incident light enters the sample at many angles. If incident light is at an angle higher than $\sin^{-1}(n_{sample}/n_{glass})$ (from Snell's Law), then total internal reflection occurs and no light is transmitted. However, if incident light is at an angle lower than $\sin^{-1}(n_{sample}/n_{glass})$, light is transmitted through the sample, the second prism

(measuring prism) and a telescope. This causes a bright range to be seen in the eyepiece of the refractometer (Abbe 1873, Rheims, Koser et al. 1997). At the critical angle, a sharp separation between the bright range and the dark range is visible to the observer.

The telescope is employed to measure the position of the border between the bright and dark areas. Two Amici prisms are present within the telescope in order to collect divergent critical angle rays into a single beam. The eyepiece of the telescope contains crosshairs and when performing a refractive index measurement, the prism angle is changed until the light-dark interface just coincides with the crosshairs. The refractive index can be read off a fixed scale. Refractive index measurements with the Abbe refractometer can also be performed at specific temperatures by circulating water through jackets surrounding the prisms.

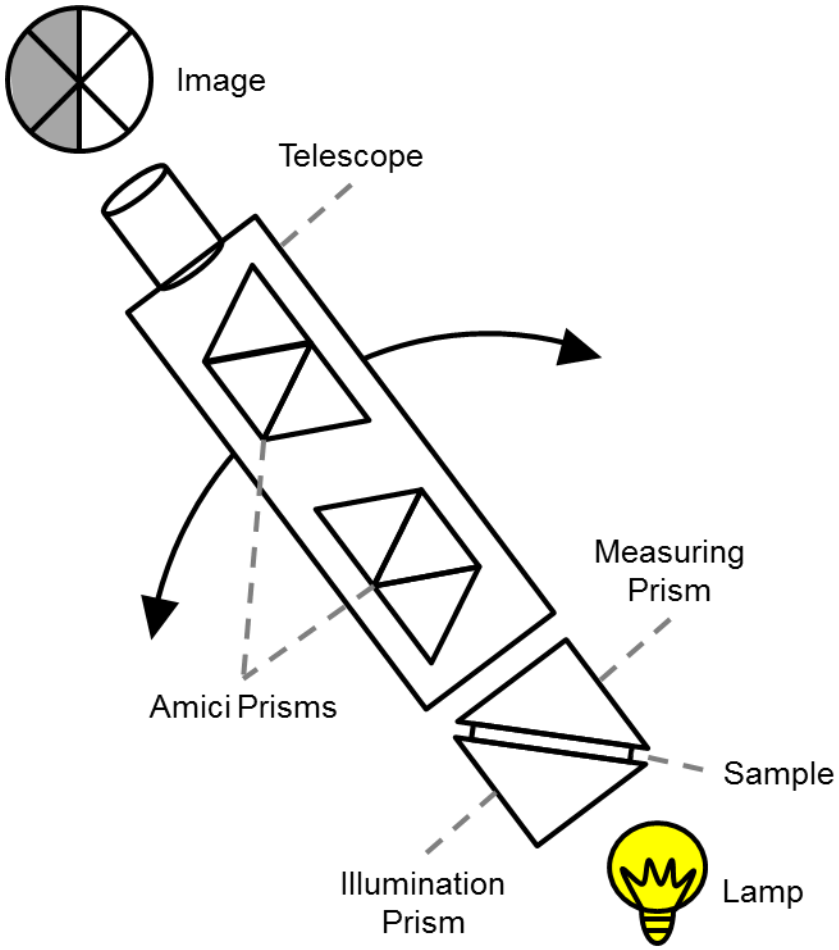

Figure 2.2.1: The design and working principles of an Abbe refractometer. Light passes through the illumination prism. If incident light is present at an angle higher than the value of $\sin^{-1}(n_{sample}/n_{glass})$, then total internal reflection occurs at this interface and no light is transmitted through the sample.

Although the Abbe refractometer is accurate (n measured to ±0.0001) and simple to use, it is limited to a single wavelength of light (Rheims, Koser et al. 1997) and the range of refractive indices that can be measured is limited by the refractive index of the illumination prism. Therefore, a tunable refractometer was designed with similar principles as the Abbe refractometer however, keeping in mind parameters for building a refractometer useful in measuring the refractive index of several solvents at the fundamental and third harmonic wavelengths of the Ti:Sapphire and Yb:KGW lasers. Some important building parameters of a tunable refractometer is discussed in the following section.

2.2.2 Tunable Refractometer

Refractive indices were measured using a UV to near IR refractometer in a temperature-controlled room at 19 °C regulated by a thermostat to 0.5 °C. The light source consisted of a 450 W xenon arc lamp (LH-450, SLM Instruments) which was coupled to a monochromator (MC320/H, SLM Instruments). The stepper motor that controlled the grating in the monochromator was replaced (SM57-66M, Excitron Corporation) and programmed such that a span of wavelengths from 260-1030 nm could be chosen. The light passed through two custom-made optical-grade equilateral yttrium aluminum garnet (YAG) prisms (Red Optronics). The surface quality of the prisms (the deviation between the actual optic and its ideal surface) is 40-20 (scratch-dig) which is standard for scientific research applications and the angle tolerance is ± 6 arcmin. The YAG crystal is grown along the <1 1 1 > crystallographic axis however, since the YAG crystal belongs to a cubic space group, birefringence was not a concern. The refractive index of YAG at both the fundamental and third harmonic wavelengths were calculated from a Sellmeier equation for YAG found in literature (Zelmon, Small et al. 1998). The following refractive indices were used (where n_{ω} and $n_{3\omega}$ are expressed as n_{λ} and $n_{\lambda/3}$): n_{773}= 1.8224 and n_{258}= 1.9431, n_{830}= 1.8204 and n_{277}= 1.9230, n_{1028}= 1.8154 and n_{343}= 1.8805.

Figure 2.2.2 shows a holder for the two prisms which can open and close on a rotation stage was custom-made by the University of Toronto Mississauga (UTM) Academic Machine Shop. The holder consists of an aluminum base which is etched to hold the prisms. One piece of Teflon is shaped to hold one prism and this piece is screwed into the base while another piece of Teflon is placed behind the second prism and this piece of Teflon can be attached to the tightening screw. A spacer separates the two prisms and holds two solutions simultaneously: the

harmonophore solution and a reference solution which included water or solvent used to dissolve the harmonophore. Once the prisms, spacer and second piece of Teflon are in place, a screw moves the second piece of Teflon, pushing the second prism against the spacer and the first prism. The screw is centered on the prism such that the second prism is parallel to the first prism and the path length between the two prisms in both chambers is constant.

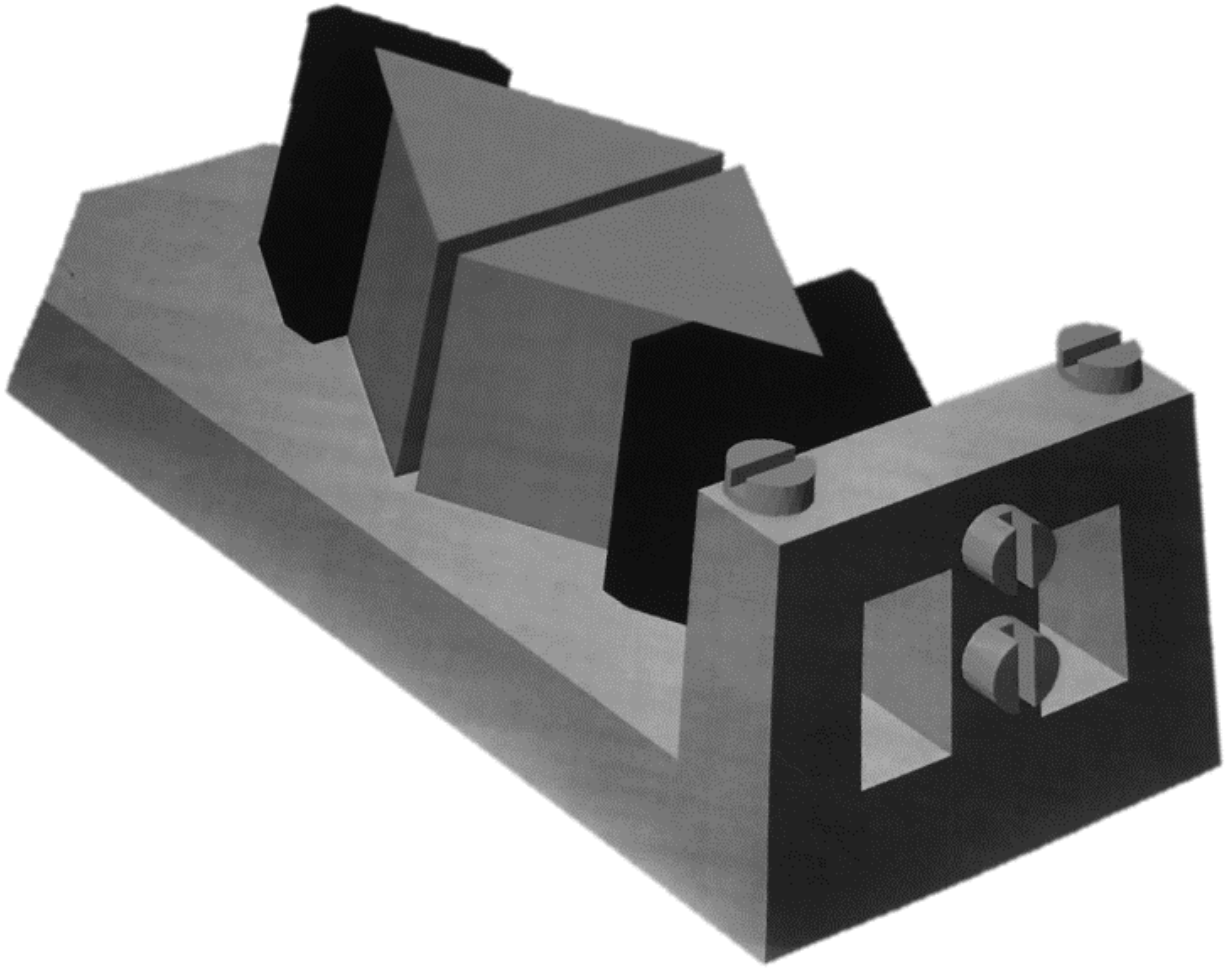

Figure 2.2.2: Design of custom-made sample chamber for the refractometer. Two Teflon pieces are cut to hold the YAG prisms on top of an aluminum base. A screw present on one side of the holder allows for tightening where both prisms are brought close together with a spacer present in between them.

The light from the monochromator is passed through the prisms and collected onto a standard CMOS camera. The light is imaged while the prisms are rotated on a rotation stage (481-A, Newport) until total internal reflection is observed. The angle (ϕ) corresponding to the difference between the critical angle of the reference solution and the harmonophore solution is

recorded. The critical angle of the harmonophore solution (θ_S) could be deduced by adding the critical angle of the reference solution (θ_R) calculated using the known refractive index of the reference solution with equations:

$$\begin{aligned}\theta_S &= \phi + \theta_R \\ \theta_R &= \sin^{-1}\left(n_{YAG}\sin\left(-\pi/3+\sin^{-1}\left(n_R/n_{YAG}\right)\right)\right)\end{aligned} \tag{2.2.1}$$

The refractive index of the solution is then back calculated using Snell's Law by the following equation:

$$n_S = n_{YAG}\sin\left(\pi/3+\sin^{-1}\left(\sin\theta_S/n_{YAG}\right)\right) \tag{2.2.2}$$

Water is used as the ultimate reference when measuring the refractive index of solvents. The refractive index values of water at 19 °C were found by using the Sellmeier equation and date from the literature (Daimon and Masumura 2007).

In general, the refractive index is a complex number where the imaginary refractive index accounts for absorption of the material of interest. With this refractometer, the real refractive index was measured however, since the real and imaginary parts of the refractive index are related by Kramers-Kronig relations, the real refractive index changes when approaching resonance.

Nonlinear refractive indices were not measured and instead, they were assumed to be small and not included in the calculation of γ. Chlorophylls are known to have large nonlinear refractive indices at visible wavelengths (Cervantes, Barboza et al. 1991, Flores and Cervantes 1994, Sun and Wang 2004). Therefore, to validate this assumption the nonlinear refractive index of chlorophylls was estimated at 1028 nm by calculating the nonlinear refractive index from the measured refractive index and $\chi^{(3)}$ value of chlorophylls. It was found that the laser beam intensity (9 GW cm^{-2}) used for THG ratio measurements leads to small refractive index changes on the order of magnitude of 10^{-9}, which is smaller than the error on the refractive index measurements.

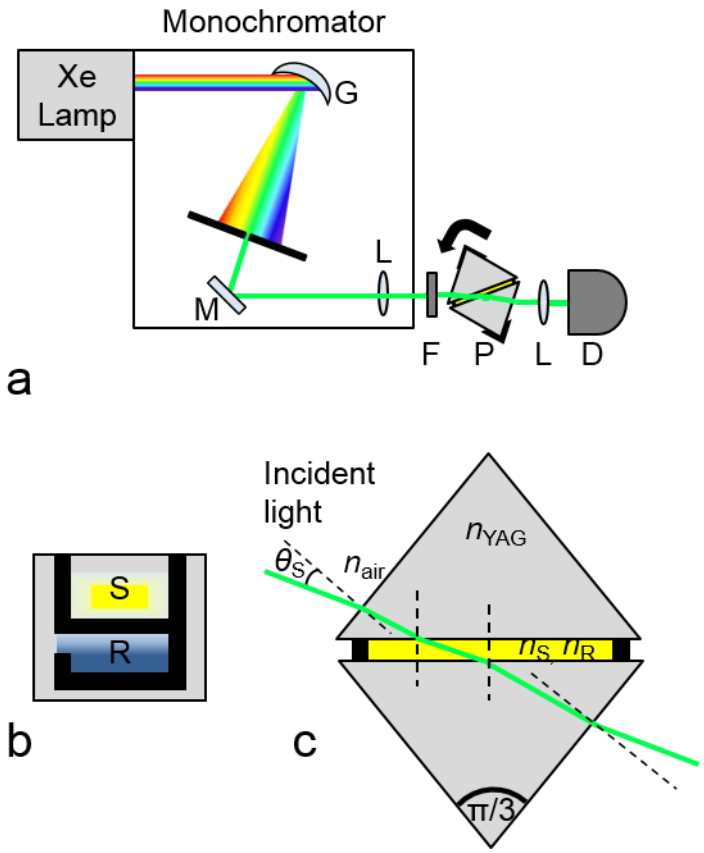

Figure 2.2.3: Tunable refractometer setup. Light from a xenon arc lamp light source (Xe Lamp) travels through a monochromator and the light is transmitted through two YAG prisms (P) containing a spacer to hold the harmonophore and reference solutions (a). Propagated light is focused through a lens (L) onto a CMOS camera (D). For infrared detection, a filter (F) is used before the prisms. Refraction occurs where light is transmitted through the solutions and prisms onto the detector. The prisms are rotated until total internal reflection occurs where light is no longer detected. A spacer placed in between prisms containing harmonophore solution (S) and reference solution (R) is shown in (b). Top view of prisms where light is transmitted through the solution until the critical angle has been reached (c). Figure reprinted with permission (Tokarz, Cisek, et al. 2012).

2.2.3 Tunable Refractometer Program

A LabVIEW program was written in order to aid in performing refractive index measurements. The LabVIEW program has three roles: (i) to control the movement of the stepper motor which in turn, moves the grating in the monochromator and selects particular wavelengths, (ii) to display the CMOS camera image in order to determine the critical angle of the solution and (iii) to calculate the refractive index of the unknown solution.

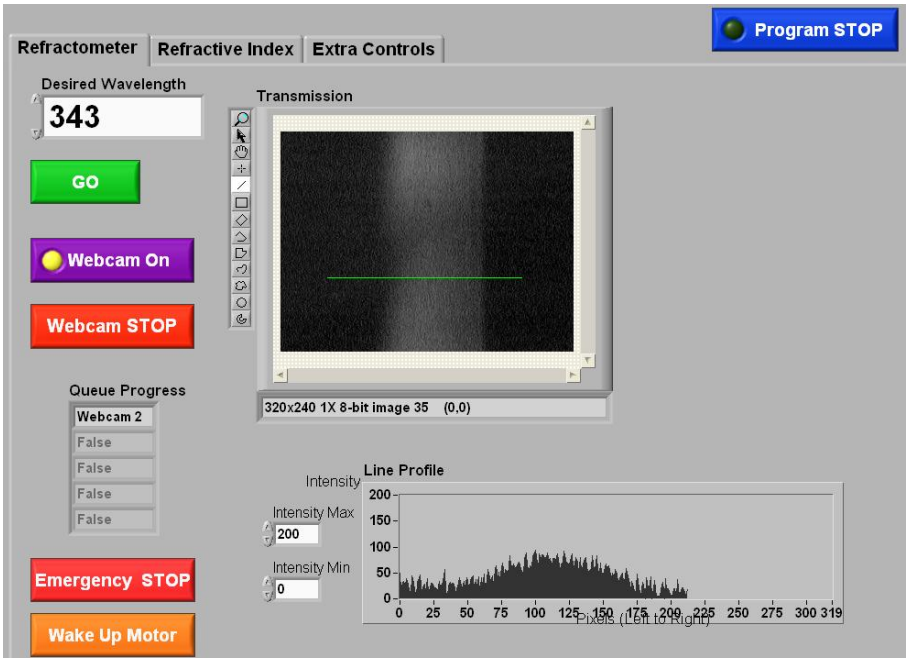

Figure 2.2.4: Tunable refractometer program in LabVIEW. The LabVIEW program controls the movement of the grating by selecting a desired wavelength. Also, the LabVIEW program displays the CMOS camera image to show the transmission of light through two chambers containing solutions.

In order to control the movement of the grating for a desired wavelength, the LabVIEW program was originally written to investigate a number of stepper motor steps. A calibration look-up table was created where with the use of a spectrometer; the number of steps taken with the stepper motor was recorded to achieve a specific wavelength. Accurate wavelengths were desired therefore, the number of steps corresponding to every 2 nm wavelength between 260 nm and 1030 nm were recorded. An algorithm was then developed with this data in order to calculate the number of steps required for a specific wavelength. When a wavelength is selected, the stepper motor will move back to its starting position and then move forward in a specific number of steps to achieve the wavelength of light desired. When the program is set to run, the motor is initialized and set to wake up, however, in case this fails, a button called ‘Wake Up Motor’ can be pressed. Also, if the wrong wavelength is entered and the stepper motor is running, an ‘Emergency STOP’ button was implemented. The ‘Extra Controls’ tab allows for the use of additional controls such as status checks, error readings and movement of the stepper motor only in the forward or backward direction by a specific number of steps.

The CMOS camera is displayed live in LabVIEW by the ‘Webcam On’ button programmed with NI-IMAQ for USB camera driver software. In the ‘Transmission’ window, light transmitted

through two chambers of solutions is seen. The rotation stage is slowly rotated clockwise. A 'Line Profile' plot was added in order to better discriminate the angle at which total internal reflection occurs. The line which displays the intensity of light in the line profile plot is drawn across the CMOS image of light transmitted from one of the chambers of solutions. The intensity which is displayed in the plot can be controlled by indicating the maximum intensity desired in the 'Intensity Max' box as well as the minimum intensity in the 'Intensity Min' box. The minimum intensity chosen is always above the background intensity. In order to minimize background intensity, a black curtain is used to cover the setup and the lights in the room are turned off. The rotation stage is rotated until the point at which the light intensity of the profile plot is the same as the background light intensity.

The position of total internal reflection on the rotation stage is measured by eye by reading the Vernier scale present on the rotation stage. Therefore, refractive index measurements with this technique are limited by the degree by which one can measure the angle of rotation with this stage which is 5 arcmin or 0.08 degrees. This corresponds to a difference in refractive index of 0.0009 and therefore, any two solutions with refractive indices close to one another and below this difference will not be read by the rotation stage. Once the positions of total internal reflection are measured for the unknown solution and a reference solution, these values can be used to calculate the refractive index of the unknown solution. The refractive index is calculated directly in the LabVIEW program under the 'Refractive Index' tab.

The wavelength at which the measurements were made is entered in the 'Wavelength (nm)' box as well as the temperature measured by the thermostat in the room and pressure which is measured by a barometer. These factors play a role in calculating the known refractive indices of air, YAG glass and the reference solution. The critical angles of the reference solution and the unknown solution are also entered into the program. The LabVIEW program then calculates the refractive index of the unknown solution using equation (2.2.2). The LabVIEW program displays the refractive index of the unknown solution along with the refractive indices of the reference solution, YAG glass and air.

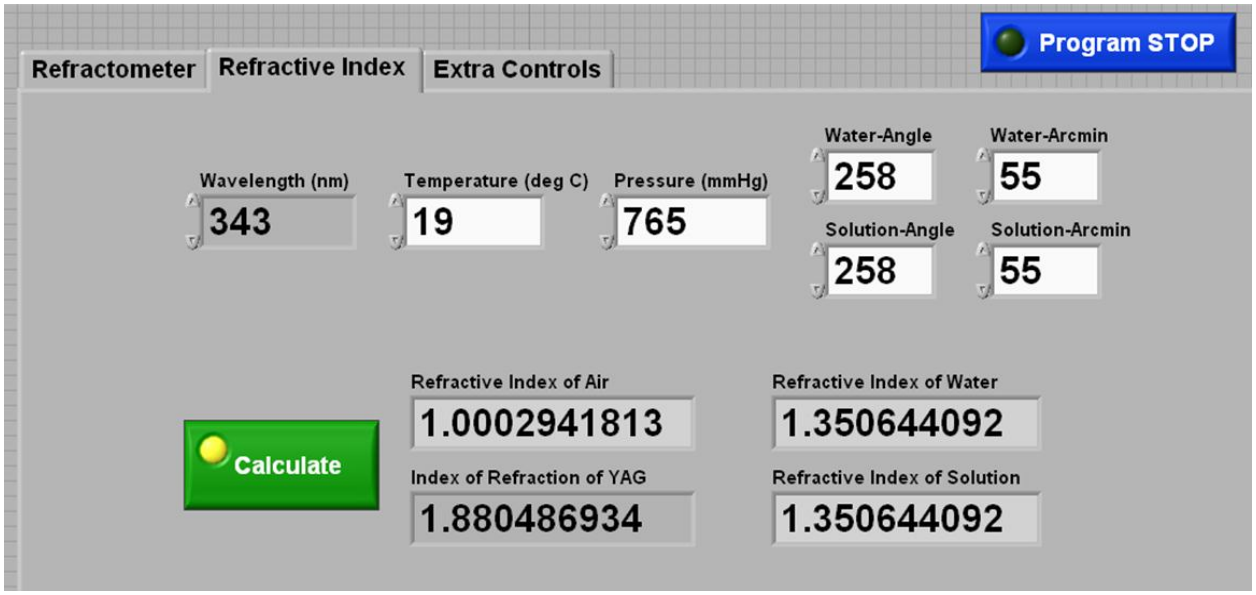

Figure 2.2.5: Calculation of refractive index in LabVIEW. The measurement of the angle at which total internal reflection occurs for a reference solution and the unknown solution are entered into this program. In addition to this, by entering the temperature and pressure, the refractive index of the unknown solution is calculated.

2.2.4 Refractive indices of Non-Absorbing Harmonophores

The accuracy of the refractometer was tested by determining the refractive indices of various concentrations of salts, NaCl (Sigma Aldrich, 99.5%) and KCl (Sigma Aldrich, 99%), as well as sugars, α-D-glucose (Sigma Aldrich, 96%) and sucrose (BioShop Canada Inc., 99.5%) at the fundamental and the third harmonic wavelengths of the Yb:KGW laser. The refractive indices measured with the refractometer were compared to refractive index data reported by A.V. Wolf at the sodium D line (589 nm).

Absorption spectra of the four solutions display no appreciable absorption at 1028 nm, 343 nm and 589 nm. Therefore, it was expected that the index of refraction of aqueous salt and sugar solutions at these three wavelengths should increase in a similar linear fashion with increasing concentrations of solute. As anticipated, the slopes corresponding to the refractive index as a function of concentration for aqueous solutions of salts and sugars at both 1028 nm and 343 nm are within error of the slope found from data given by A.V. Wolf at 589 nm seen in Figure 2.2.6 (Wolf 1966). As well, refractive index measurements of solutions at 589 nm are within error of the refractive index measurements found by A.V. Wolf (Wolf 1966). Therefore, measurements with the refractometer were deemed reliable.

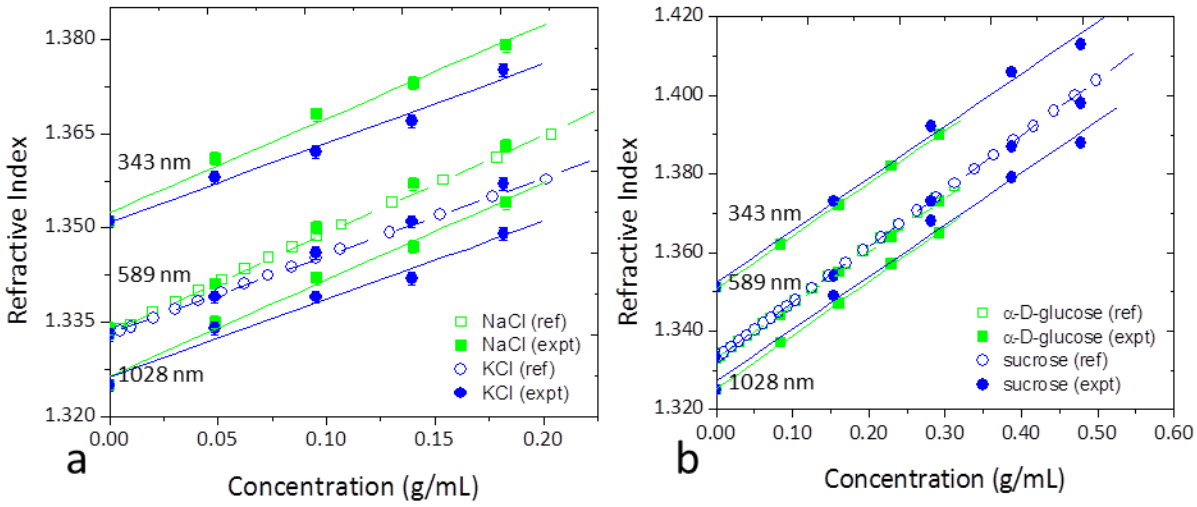

Figure 2.2.6: Refractive index measurements of aqueous solutions of salts and sugars. Refractive index measurements of aqueous solutions of salts, NaCl and KCl (a) and sugars, α-D-glucose and sucrose (b) taken at the third harmonic wavelength (343 nm), the sodium D line (589 nm) and the fundamental wavelength (1028 nm). Measurements at 589 nm were compared to refractive indices reported in literature (Wolf 1966). Note that 'exp' refers to this work and 'ref" to A.V. Wolf (Wolf 1966). Figure reprinted with permission (Tokarz, Cisek, et al. 2012).

To further demonstrate the ability to perform refractive index measurements at several wavelengths, refractive index values were found for 1 M aqueous solutions of NaCl, KCl, α-D-glucose, and sucrose. The data was fit with the following Cauchy equation:

$$n_\lambda = A + \frac{B}{\lambda^2} + \frac{C}{\lambda^4} + \frac{D}{\lambda^6} \tag{2.3.1}$$

where the Cauchy coefficients, *A*, *B*, *C*, and *D* displayed in Table 2.2-1, can be used to determine the refractive index of the aqueous solutions at a certain wavelength.

Table 2.2-1: The Cauchy coefficients obtained from fitting refractive indices of aqueous solutions of NaCl, KCl, α-D-glucose and sucrose with the Cauchy equation.

Aqueous Solution	*A*	*B*	*C*	*D*
NaCl	1.3252±0.0007	0.0080 ±0.0005	(-6.8±0.8)×10^{-4}	(2.8±0.4)×10^{-5}
KCl	1.3271±0.0008	0.0076±0.0006	(-5.9±0.9)×10^{-4}	(2.3±0.4)×10^{-5}
α-D-glucose	1.3467±0.0009	0.0061±0.0007	(-6.6±1.1)×10^{-4}	(3.4±0.5)×10^{-5}
Sucrose	1.370±0.002	0.0018 ±0.0014	(3.9±2.3)×10^{-4}	(-1.2±0.9)×10^{-5}

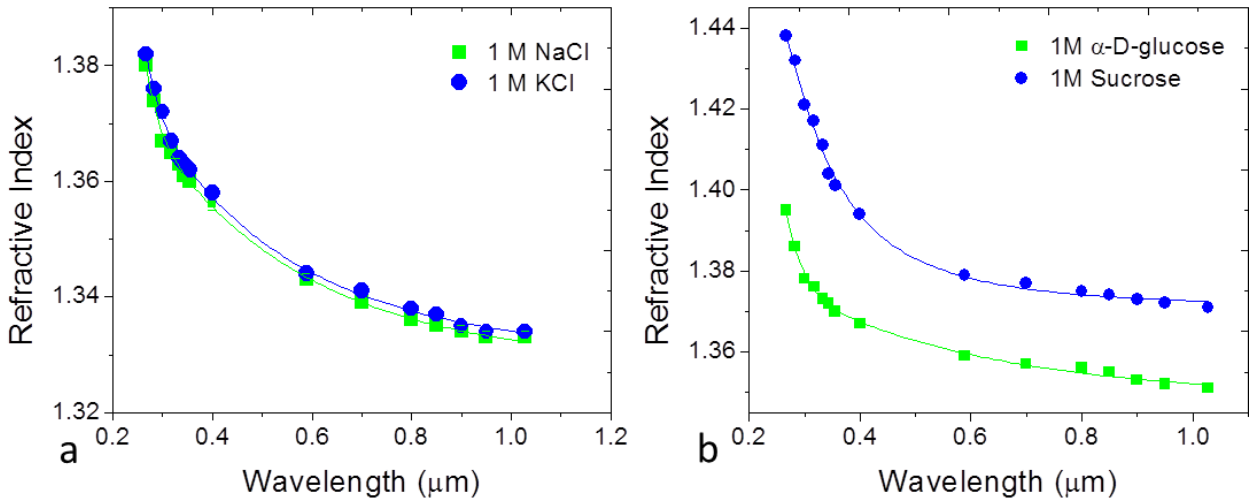

Figure 2.2.7: Refractive index measurements versus wavelength plots for aqueous solutions of salts and sugars. Refractive index measurements of aqueous solutions of NaCl and KCl (a) and α-D-glucose and sucrose (b) fit with a Cauchy equation. The adjusted R-squared values for NaCl and KCl were 0.99870 and 0.99826 while the adjusted R-squared values for α-D-glucose and sucrose were 0.99633 and 0.99533.

2.2.5 γ Values for Non-Absorbing Harmonophores

The THG ratio method was used to find the $\chi^{(3)}$ associated with aqueous solutions of salts and sugars at several concentrations. Since salts and sugars do not absorb at the fundamental and third harmonic wavelengths of the Yb:KGW laser (1028 nm and 343 nm, respectively), the refractive index of the salt and sugar solutions can be assumed to be the same as the refractive index of water. In order to validate the assumption, the refractive indices of aqueous solutions of salts and sugars were measured at 1028 nm and 343 nm. The measured refractive indices were then used with THG intensity data to calculate the corresponding $\chi^{(3)}$ values at several concentrations. An example of this data is shown for aqueous solutions of NaCl in Figure 2.2.8.

Two treatments were used in order to calculate the $\chi^{(3)}$ of salt and sugar solutions: the approximate treatment where only the refractive indices of the solvent (water) were assumed and the accurate treatment where the experimentally measured refractive indices of the solutions were used. Both treatments were plotted as is seen in Figure 2.2.8. There is no significant difference between the two treatments of $\chi^{(3)}$ values with aqueous NaCl solutions. This was also observed for KCl, α-D-glucose and sucrose. The slope of the $\chi^{(3)}$ plots as determined by the approximate method are recorded in Table 2.2-2 and compared to the slope of the $\chi^{(3)}$ plots evaluated by the accurate method. In addition to this, the γ values of salts and sugars using the

accurate method were also calculated and compared to γ values of salts and sugars found using the approximate method.

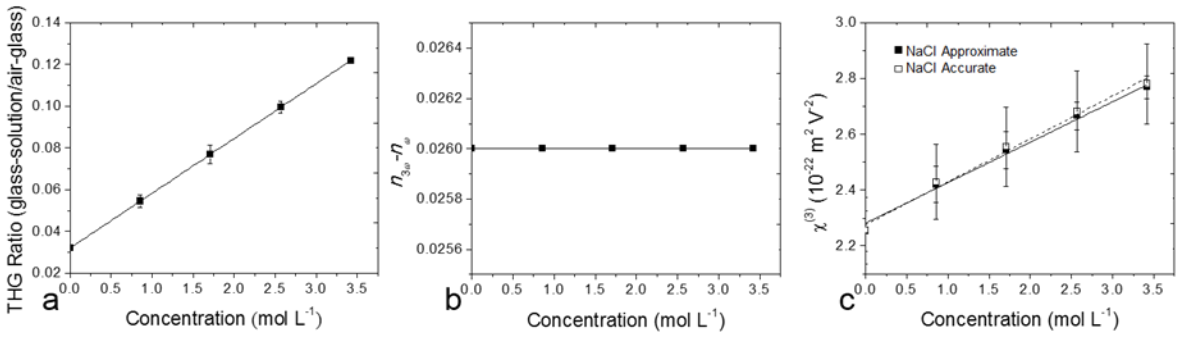

Figure 2.2.8: An example of data collected for aqueous solutions of NaCl used to determine the γ of NaCl. This data includes the THG intensity from NaCl solutions versus concentration (a), the measured difference in refractive index ($n_{3\omega}$- n_{ω}) versus concentration (b) and the values of $\chi^{(3)}$ versus concentration (c) using the approximate treatment (NaCl Approximate) where only the refractive index of water is assumed and the accurate treatment (NaCl Accurate) where the refractive index of the NaCl solution was measured. Figure reprinted with permission (Tokarz, Cisek, et al. 2012).

Table 2.2-2: Comparison of the γ of harmonophores calculated with only the refractive indices of the solvent versus the γ of harmonophores calculated using the refractive index measurements of harmonophore solutions.

Compound	$d\chi^{(3)}/dC$ (10^{-22} m^2V^{-2} $mol^{-1}L$) approximate[a]	γ (10^{-44} m^2V^{-2}) approximate[a]	$d\chi^{(3)}/dC$ (10^{-22} m^2V^{-2} $mol^{-1}L$) accurate[b]	γ (10^{-44} m^2V^{-2}) accurate[b]
NaCl	0.15±0.02	2.1±0.1	0.15±0.02	2.1±0.5
KCl	0.16±0.01	2.4±0.1	0.16±0.02	2.1±0.1
α-D-glucose	0.14±0.01	3.9±0.3	0.14±0.04	3.4±0.7
Sucrose	0.21±0.02	7.4±0.6	0.21±0.04	7±1

[a]Approximate calculation of γ where only refractive indices of the solvent, water, were assumed (n_{1028}=1.325 and n_{343}=1.351).
[b]Accurate calculation of γ where refractive indices of solution were measured and included in the calculation of $\chi^{(3)}$ at a fundamental wavelength of 1028 nm.

Although two different treatments were applied to find the second hyperpolarizability, the change in $\chi^{(3)}$ with changing concentration ($d\chi^{(3)}/dC$) for the two treatments are similar for aqueous solutions of salts and sugars. There is no significant difference between $d\chi^{(3)}/dC$ and the γ values measured using the approximate technique versus the accurate technique because aqueous solutions of salts and sugars do not absorb at the fundamental and third harmonic wavelengths of the Yb:KGW laser. As a result, the difference between the solutions' refractive indices at the third harmonic and the fundamental wavelengths ($n_{3\omega}$-n_{ω}) is constant with

increasing concentration. Since the phase-matching integral in the expression to obtain $\chi^{(3)}$ (equation (2.1.10)) depends on the difference of the aforementioned refractive indices and the difference is both constant and similar to the refractive index difference of the solvent, then the γ values calculated using the approximate and accurate treatments are comparable.

2.3 Polarization-In, Polarization-Out SHG and THG Microscopy

2.3.1 Polarization-Dependent Nonlinear Optical Microscope Measurements

Harmonophore molecules have isotropic orientation in solutions. However, during aggregation, molecules can be associated into ordered crystalline structures. The crystalline aggregates may have a symmetry axis with defined orientation in three-dimensional (3D) space. In the thesis, cylindrical aggregates of harmonophores will be studied. The orientation of the cylindrical axis can be determined with polarization harmonic generation microscopy. Polarization-dependent SHG has been previously used for quantifying organizational changes in collagen (Roth and Freund 1979, Freund, Deutsch et al. 1986, Stoller, Kim et al. 2002, Stoller, Reiser et al. 2002, Brown, McKee et al. 2003, Stoller, Celliers et al. 2003, Williams, Zipfel et al. 2005, Tiaho, Recher et al. 2007, Chen, Nadiarynkh et al. 2012), muscle (Chu, Chen et al. 2004, Plotnikov, Millard et al. 2006, Tiaho, Recher et al. 2007, Chou, Chen et al. 2008, Psilodimitrakopoulos, Santos et al. 2009, Nucciotti, Stringari et al. 2010, Schurmann, von Wegner et al. 2010), microtubules neurons (Dombeck, Kasischke et al. 2003, Psilodimitrakopoulos, Petegnief et al. 2013), starch(Cisek, Prent et al. 2009, Psilodimitrakopoulos, Amat-Roldan et al. 2010, Mazumder, Qiu et al. 2013), and other proteins such as phenylalanine hydroxylase from *Chromobacterium violaceum* (DeWalt, Begue et al. 2013). Polarization-dependent THG has also been applied to study muscle (Chu, Chen et al. 2004), cornea (Olivier, Aptel et al. 2010), and skin (Zimmerley, Mahou et al. 2013).

The nonlinear optical microscope described in section 2.1.4 was modified for polarization-in, polarization-out (PIPO) measurements (Tuer, Krouglov et al. 2011, Tuer, Akens et al. 2012). The PIPO experiment consists of measuring the second harmonic and third harmonic intensity at a number of different linear polarizer (analyzer) positions for a number of different linear polarization orientations of the incoming fundamental laser beam. A linear

polarizer (IR 1100 BC4, Laser Components Inc.) and a half-wave plate (custom flat, Comar) were inserted before the excitation objective. The analyzer (a linear polarizer) for the visible region (10LP-VIS-B, Newport) was placed after the collection objective for determination of the SHG polarization while a linear polarizer for the UV region (10LP-UV, Newport) was placed after the collection objective for determination of the THG polarization.

SHG and THG images were collected at 132 sets of excitation and analyzer angles. The half-wave plate was rotated to 11 different polarization orientations evenly spaced between excitation angles from $-\pi/2$ to $\pi/2$, whereas the analyzer was rotated to 11 different evenly spaced polarization orientation angles from $-\pi/2$ to $\pi/2$ for each excitation polarization angle. Reference frames to monitor fluctuations in SHG and THG intensity due to sample photobleaching were imaged every 11 measurements.

2.3.2 PIPO SHG Fitting Algorithm

A nonlinear susceptibility tensor of a structure containing an arbitrarily oriented cylinder is described within the laboratory frame of reference using Cartesian coordinates, xyz. The orientation of the cylindrical axis can be defined in the extrinsic laboratory frame with proper rotation Euler angles, ψ and Ω. The angle, ψ is measured between the X-axis and the projection of the cylindrical axis onto the XY plane, while the angle Ω is measured between the Z-axis and the cylindrical axis of the structure.

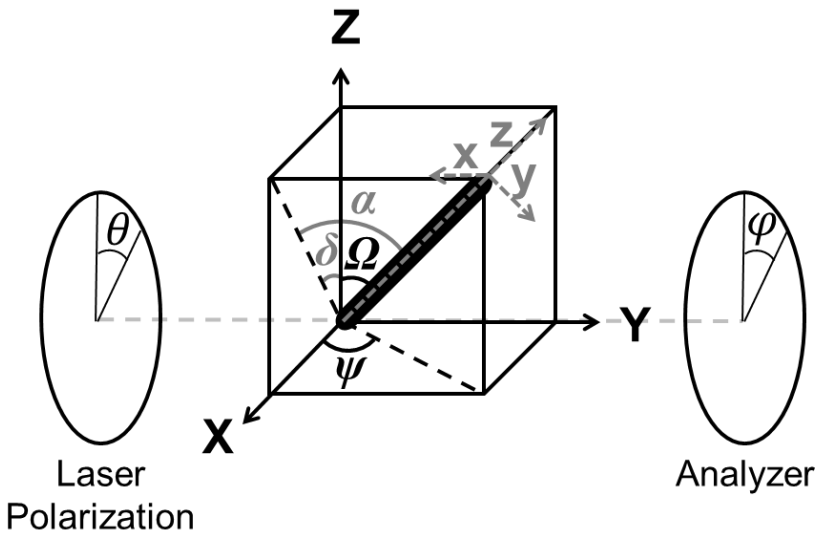

Figure 2.3.1: The orientation of the cylindrical axis, xyz, in the optical laboratory frame of reference, XYZ.

The rotated second-order nonlinear susceptibility ratio was derived by first defining a rotation matrix (R) where angle, Ω, is measured from Z in the YZ plane and the angle, ψ, is measured from X in the XY plane:

$$R = A(\psi)B(\Omega) = \begin{bmatrix} \cos\psi & -\sin\psi & 0 \\ \sin\psi & \cos\psi & 0 \\ 0 & 0 & 1 \end{bmatrix} \begin{bmatrix} \cos\Omega & 0 & \sin\Omega \\ 0 & 1 & 0 \\ -\sin\Omega & 0 & \cos\Omega \end{bmatrix} \tag{2.3.2}$$

Assuming that the sample possesses hexagonal (C_{6v}) symmetry, then the rotated second-order nonlinear susceptibility components ($\chi^{(2)}_{IJK}$') may be represented as:

$$\chi^{(2)}_{IJK}{}' = R_{Ii}R_{Jj}R_{Kk}\chi^{(2)}_{ijk} \tag{2.3.3}$$

where repeated indices imply summation as in the Einstein summation notation, and the indices imply x, y and z components of the tensor.

The second-order nonlinear susceptibility tensor components ($\chi^{(2)}_{IJK}{}'$) in the laboratory frame can be related to the nonlinear susceptibility tensor of the cylinder ($\chi^{(2)}_{ijk}$) rotated by arbitrary Euler angles ψ and Ω. If it is assumed that one dominant nonlinear dipole exists in the z direction then all other elements are small. Thus, it can be assumed that $\chi^{(2)}_{zxx} = \chi^{(2)}_{xzx} = \chi^{(2)}_{xxz}$ (Dick 1985). With this assumption, the second-order nonlinear susceptibility tensor components of the sample are expressed as follows:

$$\chi^{(2)}_{ZZZ}{}' = \chi^{(2)}_{zzz}\cos^3\Omega + 3\chi^{(2)}_{zxx}\cos\Omega\sin^2\Omega \tag{2.3.4}$$

$$\chi^{(2)}_{ZXX}{}' = \cos\Omega\left(\chi^{(2)}_{zzz}\cos^2\psi\sin^2\Omega + \chi^{(2)}_{zxx}\left(1-3\cos^2\psi\sin^2\Omega\right)\right) \tag{2.3.5}$$

$$\chi^{(2)}_{XZZ}{}' = \cos\psi\sin\Omega\left(\chi^{(2)}_{zzz}\cos^2\Omega + \chi^{(2)}_{zxx}\left(1-3\cos^2\Omega\right)\right) \tag{2.3.6}$$

$$\chi^{(2)}_{XXX}{}' = \cos\psi\sin\Omega\left(\chi^{(2)}_{zzz}\cos^2\psi\sin^2\Omega + 3\chi^{(2)}_{zxx}\left(1-\cos^2\psi\sin^2\Omega\right)\right) \tag{2.3.7}$$

Nonlinear microscopic imaging of a sample section containing aggregates of the cylindrical structures provides images that show projections of the cylindrical structures onto the

image plane XZ (Figure 2.3.1). Therefore, it is convenient to define an orientation angle δ and a projection angle α. The orientation angle δ of the cylinder in the projection plane is defined between the laboratory frame axis Z and the projection of the cylinder axis on the XZ plane. The angle α is between the axis of the cylinder and its projection in the XZ plane. The second-order nonlinear susceptibility tensor components related to the projection angles, δ and α, can be derived from Euler angles by using the following expressions:

$$\cos^2\psi = \frac{\sin^2\delta}{\sin^2\delta + \tan^2\alpha} \tag{2.3.8}$$

$$\cos\Omega = \cos\alpha\cos\delta \tag{2.3.9}$$

As a result, the second-order nonlinear susceptibility tensor components represented in equations (2.3.4) to (2.3.7) can be rewritten in terms of δ and α:

$$\chi^{(2)}_{ZZZ}{}' = \cos\alpha\cos\delta\left[\left(\frac{\chi^{(2)}_{zzz}}{\chi^{(2)}_{zxx}} - 3\right)\cos^2\alpha\cos^2\delta + 3\right]\chi^{(2)}_{zxx} \tag{2.3.10}$$

$$\chi^{(2)}_{ZXX}{}' = \cos\alpha\cos\delta\left[\left(\frac{\chi^{(2)}_{zzz}}{\chi^{(2)}_{zxx}} - 3\right)\cos^2\alpha\cos^2\delta + 1\right]\chi^{(2)}_{zxx} \tag{2.3.11}$$

$$\chi^{(2)}_{XZZ}{}' = \cos\alpha\sin\delta\left[\left(\frac{\chi^{(2)}_{zzz}}{\chi^{(2)}_{zxx}} - 3\right)\cos^2\alpha\cos^2\delta + 1\right]\chi^{(2)}_{zxx} \tag{2.3.12}$$

$$\chi^{(2)}_{XXX}{}' = \cos\alpha\sin\delta\left[\left(\frac{\chi^{(2)}_{zzz}}{\chi^{(2)}_{zxx}} - 3\right)\cos^2\alpha\sin^2\delta + 3\right]\chi^{(2)}_{zxx} \tag{2.3.13}$$

In order to identify the orientation of the cylinder axes within a focal volume, the second-order nonlinear susceptibility tensor component ratios are determined from second harmonic generation polarization-in, polarization-out (PIPO) measurements (Tuer, Akens et al. 2012). A general SHG intensity equation for PIPO measurements is derived:

$$I_{2\omega} \propto \left|\sin\varphi\left(\frac{\chi^{(2)}_{XXX}{}'}{\chi^{(2)}_{ZXX}{}'}\sin^2\theta + \sin 2\theta + \frac{\chi^{(2)}_{XZZ}{}'}{\chi^{(2)}_{ZXX}{}'}\cos^2\theta\right) + \cos\varphi\left(\sin^2\theta + \frac{\chi^{(2)}_{XZZ}{}'}{\chi^{(2)}_{ZXX}{}'}\sin 2\theta + \frac{\chi^{(2)}_{ZZZ}{}'}{\chi^{(2)}_{ZXX}{}'}\cos^2\theta\right)\right|^2 \tag{2.3.14}$$

where θ is the angle between the incident polarization and the laboratory Z-axis while φ is the angle between the analyzer and the Z-axis, within the XZ plane.

2.3.3 PIPO THG Fitting Algorithm

Similarly, the third-order nonlinear susceptibility tensor components ($\chi^{(3)}_{IJKL}$ ') of a sample containing an arbitrarily orientated cylinder are related to the susceptibility tensor ($\chi^{(3)}_{ijkl}$) of the cylinder rotated by the Euler angles, ψ and Ω, in the laboratory frame (Figure 2.3.1). If it is assumed that one dominant nonlinear dipole exists in the z direction then all other elements are small. Analogous to SHG, it is assumed that $\chi^{(3)}_{zzxx} = \chi^{(3)}_{xxzz} = \chi^{(3)}_{xzzx} = \chi^{(3)}_{zxxz} = \chi^{(3)}_{zxzx} = \chi^{(3)}_{xzxz}$. With this assumption, the PIPO THG plots can be fit with the following expression:

$$\chi^{(3)}_{ZZZZ}{}' = \chi^{(3)}_{zzzz}\cos^4\Omega + 6\chi^{(3)}_{zzxx}\sin^2\Omega\cos^2\Omega + \chi^{(3)}_{xxxx}\sin^4\Omega \tag{2.3.15}$$

$$\begin{aligned}\chi^{(3)}_{ZZXX}{}' = {} & \sin^2\Omega\left(\cos^2\psi\cos^2\Omega + \frac{1}{3}\sin^2\psi\right)\chi^{(3)}_{xxxx} + \cos^2\psi\sin^2\Omega\cos^2\Omega\chi^{(3)}_{zzzz} \\ & + \left[\sin^2\psi\cos^2\Omega + \cos^2\psi\left(1 - 6\sin^2\Omega\cos^2\Omega\right)\right]\chi^{(3)}_{zzxx}\end{aligned} \tag{2.3.16}$$

$$\begin{aligned}\chi^{(3)}_{XXXX}{}' = {} & \chi^{(3)}_{xxxx}\left(\cos^4\psi\cos^4\Omega + 2\cos^2\psi\cos^2\Omega\sin^2\psi + \sin^4\psi\right) \\ & + 6\chi^{(3)}_{zzxx}\cos^2\psi\sin^2\Omega\left(\cos^2\Omega\cos^2\psi + \sin^2\psi\right) + \chi^{(3)}_{zzzz}\cos^4\psi\sin^4\Omega\end{aligned} \tag{2.3.17}$$

The third-order nonlinear susceptibility tensor components can be related to the projection angles, δ and α, from substitution with equations (2.3.8) and (2.3.9).

The third-order nonlinear susceptibility tensor component ratios deduced from third harmonic generation polarization-in, polarization-out (PIPO) measurements can be expressed by a general THG intensity equation:

$$I_{3\omega} \propto \left| \frac{\left(\chi^{(3)}_{XXXX}{}'\right)^2}{16} \left(\begin{aligned} & \sin\varphi\sin\theta\left(\frac{\cos^2\theta\left(\chi^{(3)}_{XXZZ}{}' - \chi^{(3)}_{XXXX}{}' + \chi^{(3)}_{XZXZ}{}' + \chi^{(3)}_{XZZX}{}'\right)}{\chi^{(3)}_{XXXX}{}'} + 1 \right) \\ & + \cos\varphi\cos\theta\left(\frac{\chi^{(3)}_{ZXXZ}{}' + \chi^{(3)}_{ZXZX}{}' + \chi^{(3)}_{ZZXX}{}'}{\chi^{(3)}_{XXXX}{}'} \right) - \cos\varphi\cos^3\theta\left(\frac{\chi^{(3)}_{ZXXZ}{}' + \chi^{(3)}_{ZZXX}{}' - \chi^{(3)}_{ZZZZ}{}'}{\chi^{(3)}_{XXXX}{}'} \right) \end{aligned} \right)^2 \right| \tag{2.3.18}$$

For each 2 × 2 pixel area, the variation in SHG and THG intensity as a function of the polarizer angle, θ, and the analyzer angle, φ, was fit using equation (2.3.14) for SHG and equation (2.3.18) for THG where θ and φ were replaced with $\theta+\langle\delta\rangle$ and $\varphi+\langle\delta\rangle$ where $\langle\delta\rangle$ is the average angle of harmonophores in a pixel.

Firstly, $\chi^{(2)}_{ZZZ}$ and $\langle\delta\rangle$ were fit with the assumption that $\chi^{(2)}_{ZXX}=1$ and $\chi^{(2)}_{XXX}=\chi^{(2)}_{XZZ}=0$ where the *R*-squared value determined the optimal fitting parameters. Secondly, $\chi^{(2)}_{ZZZ}$ and $\langle\delta\rangle$ were used as initial parameters with tight bounds in order to fit $\chi^{(2)}_{XXX}$ and $\chi^{(2)}_{XZZ}$ to account for asymmetry in the PIPO plot. If fitting with $\chi^{(2)}_{XXX}$ and $\chi^{(2)}_{XZZ}$ showed no improvement to the overall fit, then the results of the initial fit were used. Similarly, fitting of PIPO THG data was performed by allowing $\chi^{(3)}_{ZZZZ}/\chi^{(3)}_{XXXX}$ and $\langle\delta\rangle$ to be fit as free parameters and fixing $\chi^{(3)}_{ZZXX}/\chi^{(3)}_{XXXX}$ between -2 and 2. Calibration of the orientation in the nonlinear optical microscope was performed with collagen extracted from rat tail tendon (Tuer, Krouglov et al. 2011, Tuer, Akens et al. 2012).

The intensity expressions for SHG (equation (2.3.14)) and THG (equation (2.3.18)) will be used to fit polarization-dependent SHG and THG data of crystalline aggregates in the following chapters.

2.4 Summary and Outlook

A harmonic generation microscope with the implemented THG ratio technique can be used to find absolute values of third-order nonlinear susceptibilities of solvents with an accuracy that is comparable to other techniques. However, $\chi^{(3)}$ values are sensitive to the difference in refractive index at the fundamental and third harmonic wavelength and as a result, the development of a refractometer was necessary in order to accurately determine $\chi^{(3)}$ values. For solutions that do not absorb at the third harmonic and fundamental wavelengths, the refractive index of the solvent can be used to find the $\chi^{(3)}$ of the solution. However, when the harmonophores solution absorbs at either the fundamental or third harmonic wavelength of the laser, this assumption is no longer valid. In order to determine accurate $\chi^{(3)}$ and γ values of such compounds, measurement of the refractive index is essential. This will be shown in the following two chapters which concentrate on determining the γ values of carotenoids and chlorophylls both of which absorb at the third harmonic wavelengths of the Ti:Sapphire and Yb:KGW lasers.

Further, polarization optics were introduced in the harmonic generation microscope in order to perform polarization-dependent SHG and THG measurements. Equations pertaining to the second-order and third-order nonlinear susceptibility tensor components of cylindrical crystalline structures were developed and as a result, the orientation of the cylindrical axis can be determined with PIPO measurements. PIPO SHG and PIPO THG will be used in Chapter 3 and 5 to determine the orientation of carotenoid molecules in carotenoid-containing aggregates.

Chapter 3
Carotenoids[2]

3.1 An Introduction to Carotenoids

3.1.1 The Molecular Structure of Carotenoids

Carotenoids belong to the chemical class of organic compounds known as polyenes. Carotenoids are polyunsaturated structures containing 40 carbon atoms. There are over 600 naturally occurring carotenoids synthesized by plants, algae and photosynthetic bacteria which range from having between 3 to 13 conjugated double bonds. From Chapter 1, it was noted that conjugated structures tend to produce large nonlinear optical responses in particular, third harmonic generation. It has been reasoned that π electrons in conjugated double bonds are less tightly bound and thus are able to respond more freely to an applied optical field (Boyd 2008). Researchers have concentrated their previous studies of the third-order nonlinear optical properties of polyenes on β-carotene (Hermann, Ricard et al. 1973, van Beek, Kajzar et al. 1991, Beljonne, Cornil et al. 1997, Marder, Torruellas et al. 1997, Tokarz, Cisek et al. 2012). This carotenoid belongs to one class of carotenoids that does not contain oxygen functional groups referred to as carotenes. β-carotene is an unsaturated hydrocarbon molecule with eleven conjugated double bonds. The γ values of β-carotene, as well as other additional carotenoids seen in Figure 3.1.1 were characterized in this study.

With the exception to β-carotene, all the other carotenoids studied belong to a class of carotenoids which contain oxygen functional groups known as xanthophylls. Violaxanthin and neoxanthin both contain 9 conjugated double bonds; however, violaxanthin has two epoxide groups and two hydroxyl groups, while neoxanthin has one epoxide group and three hydroxyl groups. Lutein and zeaxanthin both have two hydroxyl groups; however, lutein has one less conjugated double bond than zeaxanthin (10 versus 11). Violaxanthin, neoxanthin, lutein and zeaxanthin naturally occur in fruits, vegetables and other plants.

---

[2]Reproduced (and adapted) from Tokarz, D., Cisek, R., Garbaczewska, M., Sandkuijl, D., Qiu, X., Stewart, B., Levine, J.D., Fekl, U., and Barzda, V. (2012) "Carotenoid based bio-compatible labels for third harmonic generation microscopy," Physical Chemistry Chemical Physics **14**(30): 10653-10661 with permission from the PCCP Owner Societies. The specific contributions made by all authors are presented in the Statement of Contributions section on page 142.

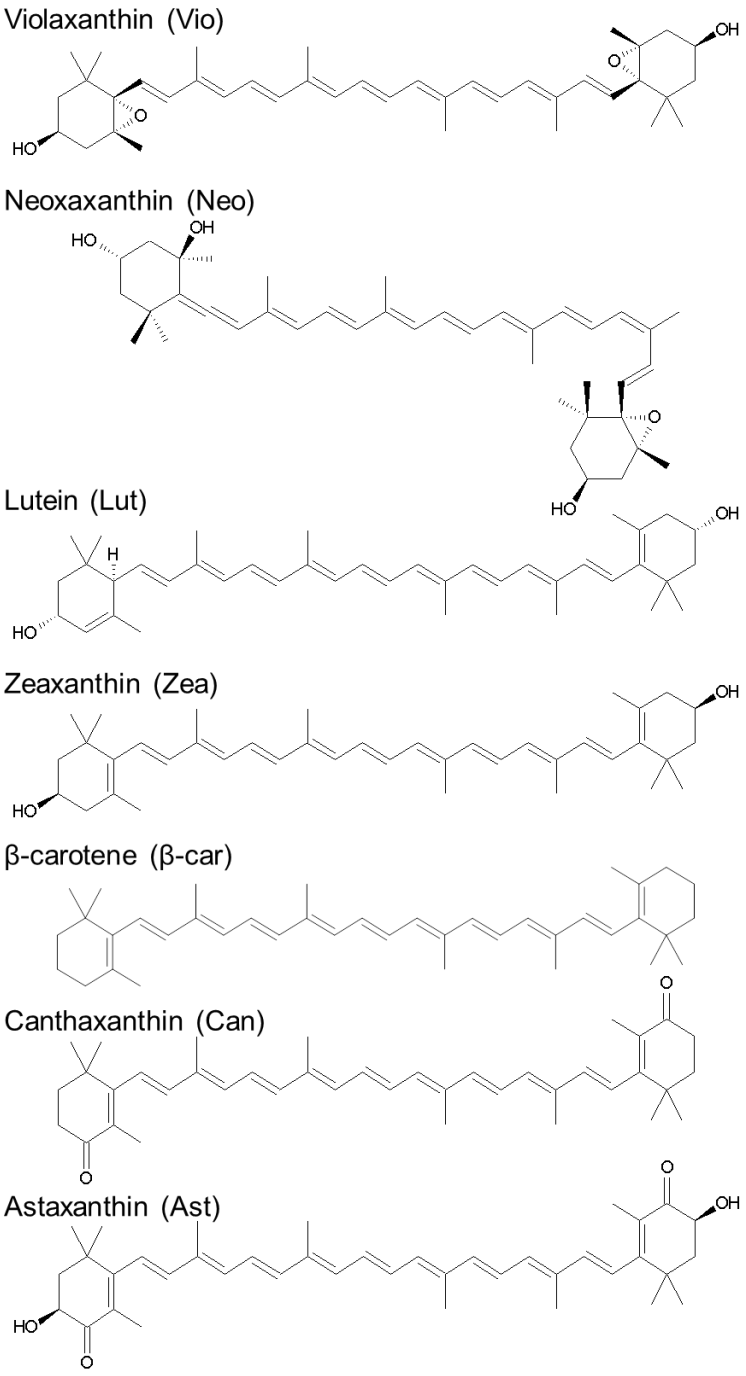

Figure 3.1.1: The molecular structures of specific carotenoids.

In addition to these carotenoids, canthaxanthin and astaxanthin were also investigated. These two carotenoids naturally occur in plants, green algae and crustaceans. Both canthaxanthin and astaxanthin are amongst the longest naturally occurring carotenoids, containing 13 conjugated double bonds, where both have two ketone functional groups, and astaxanthin has an additional two hydroxyl groups.

3.1.2 The Absorbance Properties of Carotenoids

Carotenoids absorb in the visible region between 400 nm and 600 nm as a result of a strongly allowed transition from the ground state, S_0 ($1^1A_g^-$), to the second excited state, S_2 ($1^1B_u^+$). This transition is typically split into several vibronic transitions resulting in a series of 3 absorption bands. Since carotenoids belong to the C_{2h} symmetry point group, the first excited state, S_1 ($2^1A_g^-$) has the same inversion symmetry as the ground state. As a result, the S_1 state is optically forbidden by a single photon transition from the ground state.

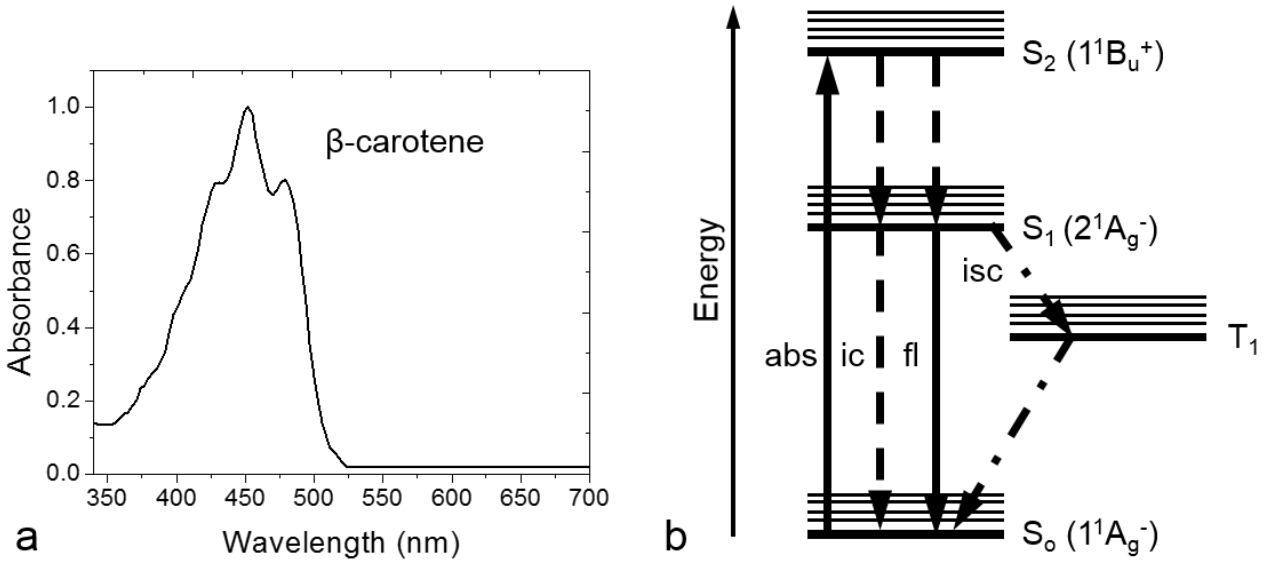

Figure 3.1.2: Normalized absorption spectrum of β-carotene as well as a typical energy level diagram of carotenoids. The absorption spectrum of β-carotene in acetone taken at room temperature (a) and the energy level diagram used to describe the possible processes that can occur (b). Note the abbreviations: abs, absorption; ic, internal conversion; fl, fluorescence and isc, intersystem crossing.

A diagram showing the energy levels and different types of transitions that can occur between electronic states is presented in Figure 3.1.2. Absorption of blue light corresponds to the second excited state (S_2). From the second excited state, vibrational decay to the lowest vibrational level of this state can occur and excitation energy can be dissipated as heat (internal conversion) to the ground state. Alternatively, fluorescence can occur from the second excited state (S_2) to the ground state or the first excited state (S_1) to the ground state. As the conjugated length of the carotenoid increases, the fluorescence emission from S_2 to S_0 versus S_1 to S_0 increases. For example, the fluorescence emission yield from S_1 to S_0 for β-carotene is very low ($<10^{-5}$) (Frank and Christensen 2008).

Intersystem crossing can also occur from an excited singlet state to a triplet state causing the spin of the excited electron to flip. However, phosphorescence emission is negligible as the rate of nonradiative relaxation from T_1 to S_0 is efficient.

The triplet states energies of certain carotenoids are even lower than the energy of singlet oxygen. Therefore, carotenoids are efficient quenchers of singlet oxygen ($^1O_2$). This is specifically important in plants where carotenoids known as xanthophylls protect singlet oxygen from damage to the photosynthetic apparatus (Telfer, Pascal et al. 2008).

3.2 Determination of γ for Carotenoids

The carotenoids presented in Figure 3.1.1 were dissolved in acetone in order to perform second hyperpolarizability measurements. The THG intensities from carotenoid solution-glass and glass-air interfaces were collected along with the refractive indices of the carotenoid solutions at the third harmonic wavelength and the fundamental wavelength. The THG intensity ratio (Figure 3.2.1 (a, d, g)) and the difference in refractive index (Figure 3.2.1 (b, e, h)) at the third harmonic wavelength versus the fundamental wavelength ($n_{3\omega}$-n_{ω}) is shown in Figure 3.2.1 for three laser wavelengths: 773 nm, 830 nm and 1028 nm.

As seen in Figure 3.2.1, the THG intensity ratio for carotenoids in acetone decreases with increasing concentration at all fundamental wavelengths studied while the difference in refractive index decreases with increasing concentration at Ti:Sapphire wavelengths and the refractive index difference increases with increasing concentration at 1028 nm. At 773 nm and 830 nm, $n_{3\omega}$-n_{ω} decreases with increasing concentration because acetone and the carotenoids absorbs immensely at the third harmonic of the Ti:Sapphire wavelengths whereas at the third harmonic wavelength of 1028 nm, acetone does not absorb.

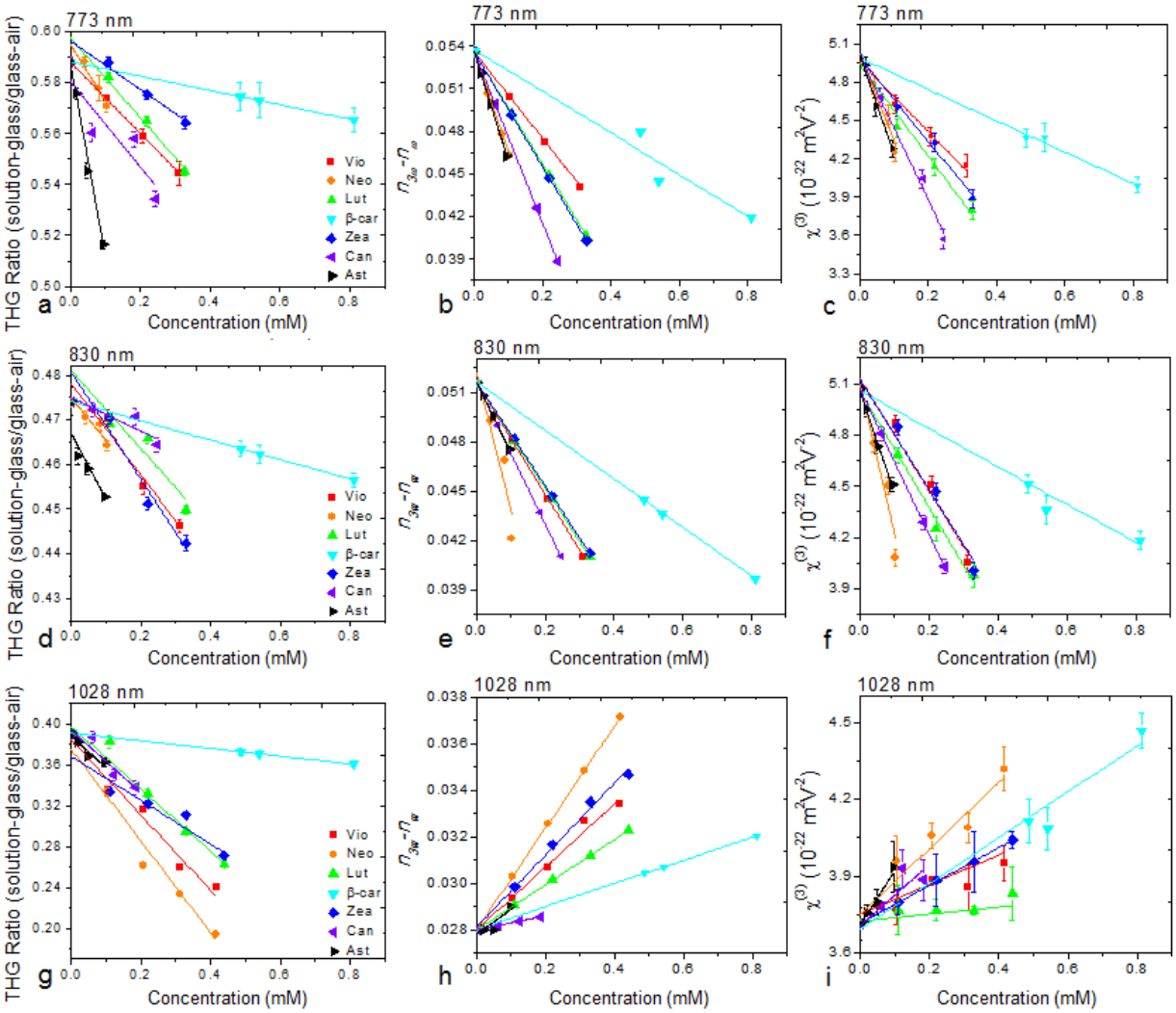

Figure 3.2.1: Data collected for the calculation of the second hyperpolarizability of carotenoids at 3 different fundamental wavelengths. The THG intensity ratio, the difference in refractive index and the third-order nonlinear optical susceptibility for carotenoids as a function of concentration is shown at excitation wavelengths: 773 nm (a through c), 830 nm (d through f) and 1028 nm (g through i). Figure adapted with permission (Tokarz, Cisek, et al. 2012).

Since the refractive index difference is not constant like it is with aqueous solutions of salts and sugars this demonstrates that the refractive index of the solvent cannot be used as an approximation to find $\chi^{(3)}$ as was used in Chapter 2. Using the THG intensity ratios and the measured refractive indices, $\chi^{(3)}$ values were calculated and they are shown in Figure 3.2.1 (c, f, i). The $\chi^{(3)}$ plots show a declining trend with increasing concentration at 773 nm and 830 nm whereas at 1028 nm, the $\chi^{(3)}$ plot increases with increasing concentration. The sign of the second hyperpolarizability for carotenoids is determined from their $\chi^{(3)}$ plots. This is evidence that the sign of γ is negative for carotenoids at 773 nm and 830 nm while the sign of γ is positive for

carotenoids at 1028 nm. The sign of γ is determined for carotenoid molecules with respect to acetone. Since acetone absorbs strongly at 773 nm and 830 nm, the change in sign may occur due to the change in sign of acetone generated THG, or due to a change of sign for the γ value of carotenoids.

Table 3.2-1: The second hyperpolarizability values for carotenoids at 773 nm, 830 nm, and 1028 nm.

Carotenoid	Conjugated double bonds	γ (10^{-41} m^2V^{-2}) (773 nm)	γ (10^{-41} m^2V^{-2}) (830 nm)	γ (10^{-41} m^2V^{-2}) (1028 nm)
Violaxanthin	9	-16.2 ± 0.1	-20 ± 2	+3.1 ± 0.6
Neoxanthin	9	-43 ± 5	-58 ± 6	+8 ± 2
Lutein	10	-22 ± 1	-21 ± 2	+1.4 ± 0.3
β-carotene	11	-7.1 ± 0.4	-7 ± 1	+4.9 ± 0.8
Zeaxanthin	11	-17.5 ± 0.3	-20 ± 2	+5 ± 1
Canthaxanthin	13	-34 ± 3	-26 ± 3	+11 ± 1
Astaxanthin	13	-45 ± 4	-36 ± 3	+14 ± 2

In general, the magnitude of the γ values at 773 nm and 830 nm are larger for all the carotenoids than the γ values at 1028 nm excitation. The larger values are indicative of more resonance enhancement of THG at Ti:Sapphire third harmonic and second harmonic wavelengths than at 1028 nm.

In Table 3.2-1, violaxanthin and neoxanthin have a larger γ value at 830 nm than at 773 nm. Figure 3.2.1 (e) shows that both violaxanthin and neoxanthin demonstrate a larger difference between $n_{3\omega}$ and n_{ω} at 830 nm than at 773 nm seen in Figure 3.2.1 (b). The wavelength region at which there are maximum absorbance peaks in the UV for violaxanthin and neoxanthin are very similar as seen in Figure 3.2.2. This wavelength is slightly shifted for lutein and zeaxanthin. The large difference in refractive index likely occurs between the third harmonic wavelengths of 773 nm and 830 nm (258 nm and 277 nm) for violaxanthin and neoxanthin since they are on opposite sides of an absorbance peak. The γ values for lutein and zeaxanthin do not vary as much between 773 nm and 830 nm. The difference between $n_{3\omega}$ and n_{ω} at both these wavelengths are very similar.

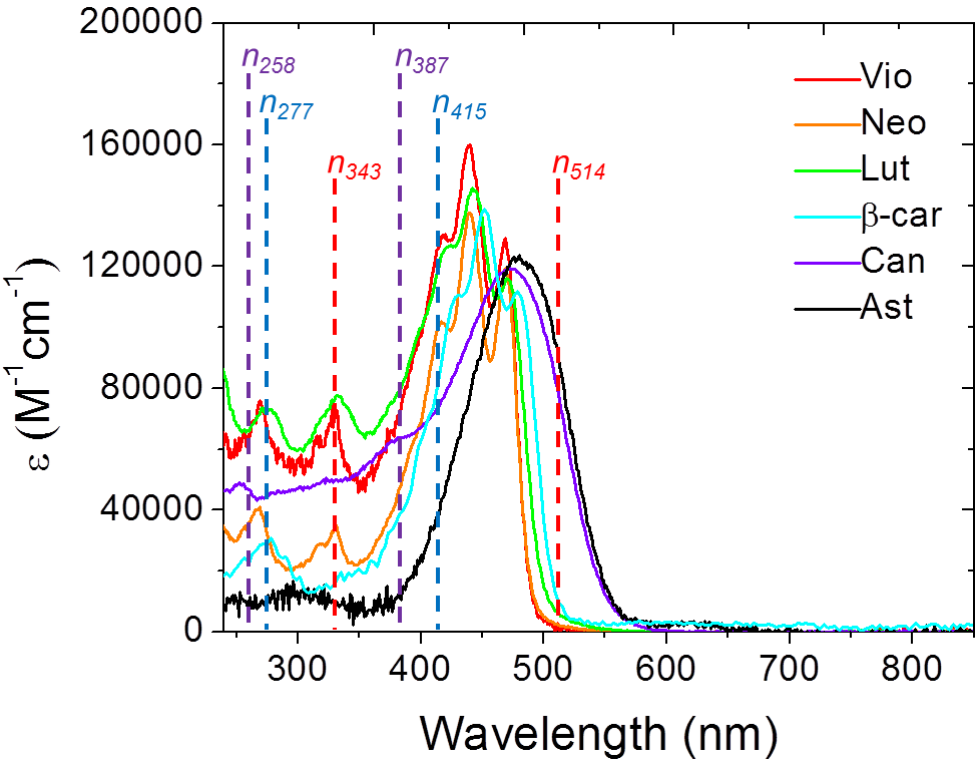

Figure 3.2.2: Absorption plot of violaxanthin, neoxanthin, lutein, β-carotene, canthaxanthin and astaxanthin. All the carotenoids were dissolved in ethanol except β-carotene which was dissolved in hexane. Molar extinction coefficients were taken from literature (Jeffrey 1997). Figure reprinted with permission (Tokarz, Cisek, et al. 2012).

Canthaxanthin and astaxanthin have a larger γ value at 773 nm than at 830 nm. Figure 3.2.1 (b) shows that both canthaxanthin and astaxanthin exhibit a larger difference between $n_{3\omega}$ and n_{ω} at 773 nm than at 830 nm seen in Figure 3.2.1 (b, e). Just below the third harmonic wavelength of 773 nm, there is a slight absorption peak for both canthaxanthin and astaxanthin which may contribute to a larger refractive index value at 773 nm than at 830 nm. The γ value for all the carotenoids at 773 nm or 830 nm versus 1028 nm excitation are at least double with exception to β-carotene where at all three wavelengths, $|n_{3\omega} - n_{\omega}|$ for β-carotene are very similar.

The carotenoids are ordered by increasing number of conjugated double bonds in Figure 3.2.3. Previous studies with polyenes have shown an enhancement of γ with increasing length of the conjugated chain due to the presence of delocalized π electrons (Hermann and Ducuing 1974). In general, a linear increase of the second hyperpolarizability with increasing conjugated double bonds exists for all wavelengths studied where violaxanthin and neoxanthin are outliers. Specifically, violaxanthin has a higher γ value than lutein. Although lutein has an additional double bond, the presence of epoxide functional groups on violaxanthin is attributed to the

higher nonlinear optical response. Similarly, neoxanthin has a higher γ value than lutein, violaxanthin and zeaxanthin likely due to the presence of an epoxide as well as increased asymmetry within the molecule (Marder, Torruellas et al. 1997). This trend suggests that the epoxide enhances the optical nonlinearity of a molecule more than the addition of an extra double bond.

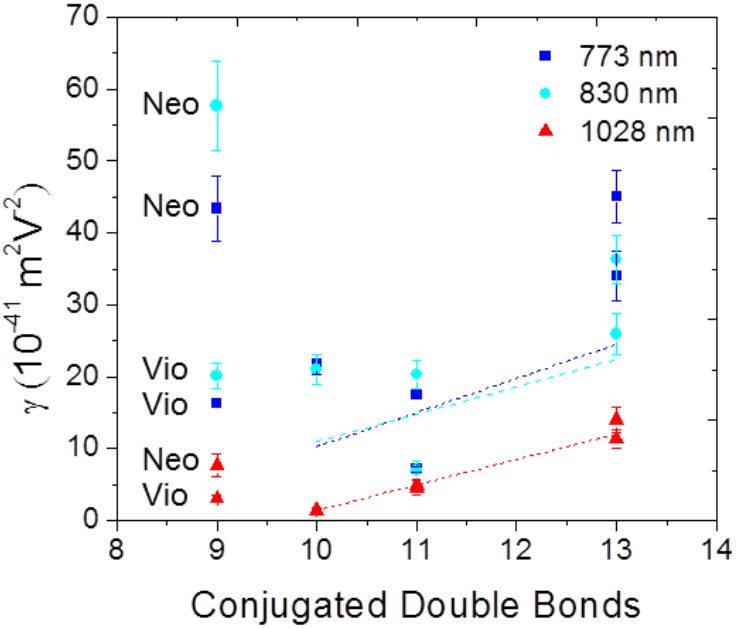

Figure 3.2.3: The dependence of the second hyperpolarizability on conjugation for several carotenoids. The number of conjugated double bonds of carotenoids versus their second hyperpolarizability values was plotted for 3 laser wavelengths: 773 nm, 830 nm, and 1028 nm. The γ values at 10 conjugated double bonds corresponds to lutein while at 11 conjugated double bonds both β-carotene and zeaxanthin are represented while 13 conjugated double bonds corresponds to canthaxanthin and astaxanthin. Figure reprinted with permission (Tokarz, Cisek, et al. 2012).

The measured γ values of carotenoids emphasize the importance of a conjugated structure as a characteristic for a good harmonophore. These results also demonstrate that functional groups can influence the nonlinear optical characteristics of the conjugated backbone. Due to the absorbance of carotenoids and THG resonance enhancement, refractive indices of carotenoids at the third harmonic and the fundamental wavelength are necessary in order to determine γ values and compare at several wavelengths.

3.3 Carotenoid Containing Liposomes as Harmonophores

3.3.1 Introduction

As seen from the previous section, the γ values of carotenoids are large compared to the γ values of salts and sugars. In the literature, carotenoids are recognized as having large second hyperpolarizability values (Marder, Torruellas et al. 1997). As well, carotenoids are non-toxic and at certain concentrations, even advantageous to one's health. However, carotenoids have not been exploited as potential labels for THG microscopy. The reason for this is likely due to the fact that most carotenoids are hydrophobic and therefore, carotenoids cannot be easily employed as water soluble dyes for labeling biological structures. Alternatively, carotenoids incorporated into liposomes can be used for labeling purposes. The following section will focus on THG studies of carotenoid liposomes for labeling applications while biological labeling examples will be demonstrated in Chapter 6.

3.3.2 Carotenoid Liposome Preparation

In order to prepare carotenoid incorporated liposomes, 2.5 mmol of a phospholipid, DL-α-phosphatidylcholine, dipalmitoyl (DPPC) (Sigma Aldrich, 99%), and varying concentrations of β-carotene (0.05, 0.25, 0.5, and 1.25 mmol) were dissolved in chloroform. The solutions were evaporated to dryness by use of nitrogen gas. The lipid film was suspended in 0.5 ml of distilled water. The lipid suspension was then sonicated at about 45 °C for 30 min. The sonicated lipid suspension was transparent indicative of multilamellar vesicle formation (Crowe and Crowe 1988, Nagase, Ueda et al. 1999). The procedure was repeated a second time with 0.25 mmol of neoxanthin instead of β-carotene.

Liposomes were immobilized in polyacrylamide gel containing 1.1 M acrylamide (Sigma Aldrich, 99%), 13.8 mM N,N'-methylenebisacrylamide (Sigma Aldrich, 99%), 32.3 mM ammonium persulfate (Sigma Aldrich, 98%), and 33.2 mM tetramethylethylenediamine (Sigma Aldrich, 99%), for ease in scanning with the nonlinear optical microscope.

3.3.3 THG Intensities of Carotenoid Liposomes

Initially, DPPC liposomes containing various concentrations of carotenoids were investigated. The liposomes containing carotenoids were imaged with the nonlinear optical microscope. The signal intensities at different laser powers were recorded and a cubic dependence was

demonstrated verifying that obtained signals were generated due to the third-order optical nonlinearity.

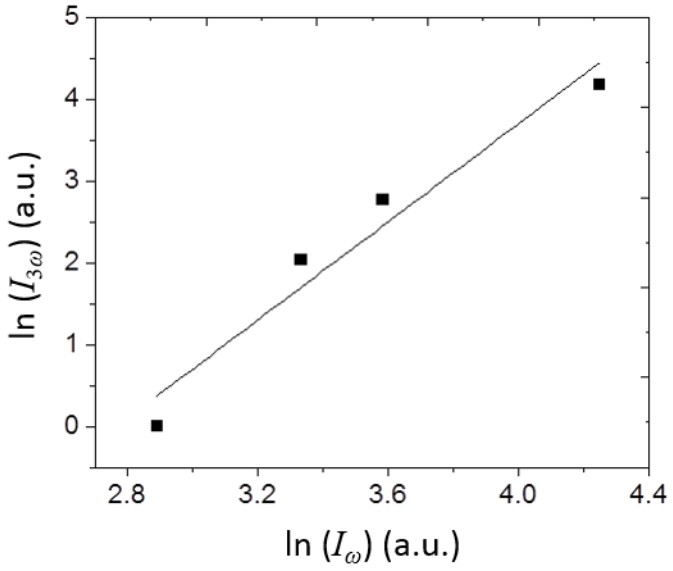

Figure 3.3.1: The THG intensity dependence on fundamental intensity. A log-log plot of the THG intensities ($I_{3\omega}$) of β-carotene liposomes with 1028 nm excitation at different fundamental laser intensities (I_{ω}) is shown. The slope of the fit line was 3.0+/0.5. This verifies that the signal collected was generated due to the third-order nonlinearity. Figure reprinted with permission (Tokarz, Cisek, et al. 2012).

Four concentrations of β-carotene were chosen and the molecules were incorporated into liposomes. The average THG intensity per liposome was plotted against the number of moles of β-carotene. In equation (1.2.4), the third-order nonlinear polarization is proportional to the number of moles. Since THG intensity is proportional to the third-order nonlinear polarization squared thus, it is expected that the THG intensity measured from liposomes containing a homogeneous distribution of β-carotene should have a square power dependence with β-carotene concentration as is seen in Figure 3.3.2.

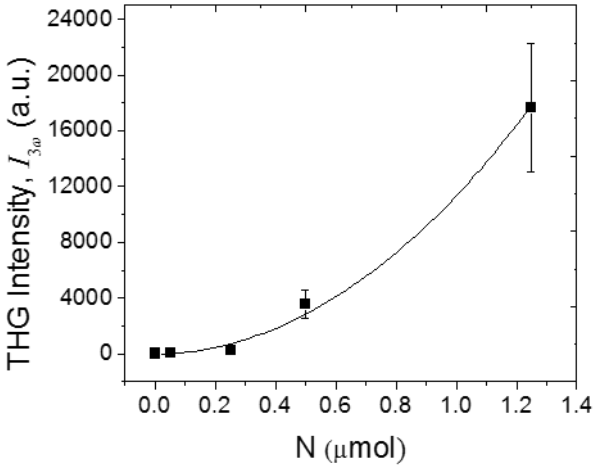

Figure 3.3.2: THG signal intensity dependence on the concentration of β-carotene in liposomes. The black squares are experimental data points while the curve represents the fit of THG intensity ($I_{3\omega}$) proportional to the square number of moles of β-carotene taken at 1028 nm. Figure reprinted with permission (Tokarz, Cisek, et al. 2012).

Further, 0.25 μmol of neoxanthin was incorporated into DPPC liposomes and the THG intensities were compared with the THG intensities of 0.25 μmol β-carotene DPPC liposomes as seen in Fig. 3.3-3. Although canthaxanthin and astaxanthin have higher γ values than neoxanthin, liposomes were incorporated with neoxanthin because canthaxanthin and astaxanthin aggregate at very low concentrations and therefore, it was difficult to determine whether liposomes or aggregates were being imaged (Sujak, Gabrielska et al. 2005).

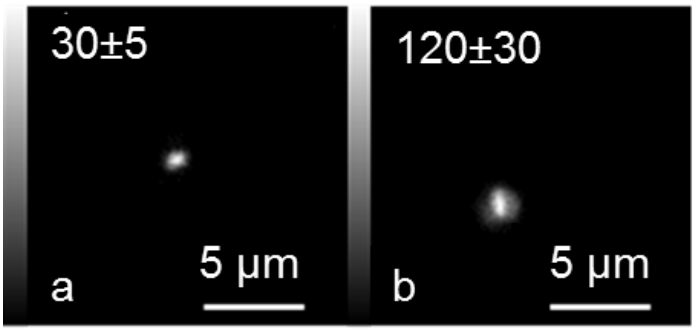

Figure 3.3.3: THG images of 0.25 μmol of β-carotene (a) and 0.25 μmol of neoxanthin (b) incorporated into a liposome. The numbers in the upper left corner indicate average photon counts in a pixel taken by selecting a region where the THG intensity is higher or equal to 1/e and dividing the mean THG intensity by the area of the region. The grey scale bar on the left side of the images ranges from 0 to the maximum signal intensity. Figure reprinted with permission (Tokarz, Cisek, et al. 2012).

Second hyperpolarizability values experimentally measured for β-carotene and neoxanthin show about a factor of 2 difference. Therefore, since THG intensity is proportional to the γ value squared, it is expected that liposomes with neoxanthin should be much brighter than β-carotene liposomes. This indeed was observed in the neoxanthin liposomes (see the average number of photon counts in respective images of Figure 3.3.3). However, the ratio of THG intensities for β-carotene and neoxanthin incorporated in liposomes is less than the ratio of the γ values squared for β-carotene and neoxanthin. One reason as to why these ratios are not equal is due to the fact that the γ values for β-carotene and neoxanthin were measured in solvent and therefore, the carotenoids were arranged isotropically whereas carotenoid molecules in liposomes are partially aligned in the bilayer membrane. β-carotene and neoxanthin tend to orient differently in the lipid bilayer (Gruszecki 2009). The orientation of carotenoids in a lipid membrane depends on the functional groups present at the ends of the carotenoid as well as the ability for these functional groups to form hydrogen bonds within the lipid membrane (Gruszecki 2009). Nonpolar carotenoids such as β-carotene freely orient with respect to the lipid membrane when incorporated in liposomes as seen in Figure 3.3.4 (a) whereas polar carotenoids form hydrogen bonds with the lipid membrane headgroups and water at the membrane interface, and thus, polar carotenoids tend to align vertically with the alkyl lipid chains as seen in Figure 3.3.4 (b) (Gruszecki 2009). Therefore, differences observed between the ratio of γ values of β-carotene and neoxanthin and the ratio of THG signal intensities may be due to differences in orientation between β-carotene and neoxanthin in lipid bilayers which may affect the refractive indexes.

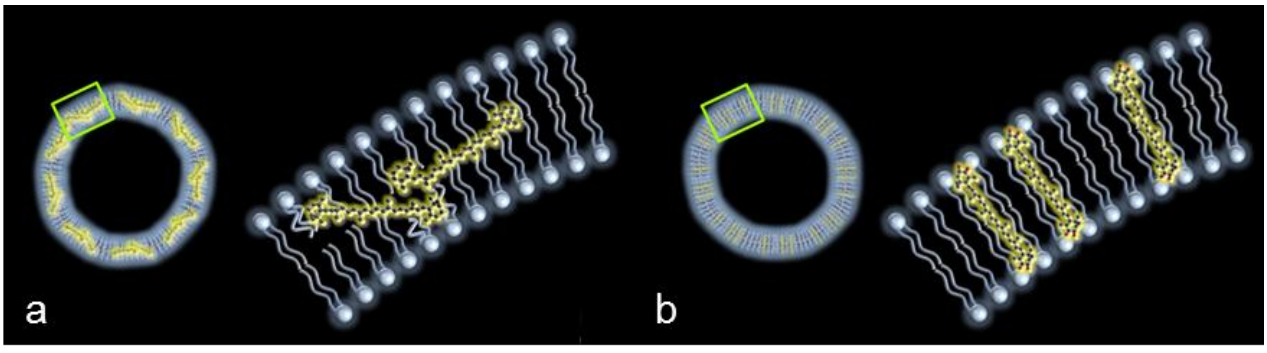

Figure 3.3.4: The organization of nonpolar and polar carotenoids in a lipid membrane. Examples of non-polar carotenoids (a) and carotenoids with polar functional groups (b) organized in liposomes.

3.3.4 Optimizing Parameters for Photobleaching-Free Imaging with Carotenoid Harmonophores

The ability to use carotenoids as harmonophore probes in THG microscopic imaging was assessed by investigating the photobleaching of carotenoid liposomes at different laser intensities.

With 773 nm excitation at 0.6 nJ pulse energy and a scanning pixel dwell time of 4.6 µs, β-carotene liposomes photobleached with a half-life of 13 min whereas at 0.4 nJ pulse energy, the β-carotene liposomes did not photobleach for 20 min as seen in Figure 3.3.5. Further, at 830 nm, the β-carotene liposomes did not photobleach for 20 min with less than 0.2 nJ pulse energy. β-carotene liposomes with 1028 nm excitation at 1.0 nJ pulse energy photobleached with the 1/e lifetime of 6.6 min. At 0.5 nJ pulse energy and lower, β-carotene liposomes did not photobleach.

At 0.5 nJ pulse energy and 1028 nm excitation, neoxanthin liposomes photobleached where the 1/e point was found to be 3.0 min. At 0.3 nJ pulse energy and imaging for 20 min, neoxanthin liposomes did not bleach.

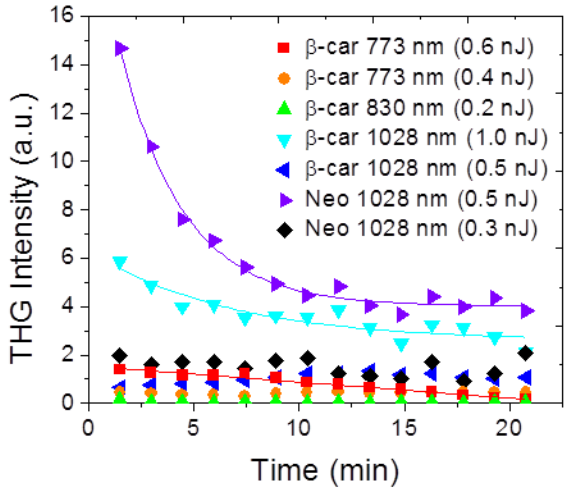

Figure 3.3.5: Photobleaching curves for 0.25 µmol of β-carotene and 0.25 µmol of neoxanthin incorporated into liposomes. β-carotene liposomes with 773 nm and 830 nm excitation did not photobleach at 0.4 nJ and 0.2 nJ pulse energy, respectively. Fitting was performed with exponential decay functions where the 1/e point with 1028 nm excitation was found to be 6.6 min for β-carotene liposomes at 1.0 nJ pulse energy and 3.0 min for neoxanthin liposomes at 0.5 nJ. Figure reprinted with permission (Tokarz, Cisek, et al. 2012).

As a result, neoxanthin liposomes may be used for imaging at considerably lower laser pulse energies than the imaging of β-carotene liposomes at 1028 nm excitation. Although neoxanthin liposomes photobleach at high laser pulse energies, they may be used if experiments only require using beacons for THG labeling as even after imaging for 20 min, the THG intensity of neoxanthin liposomes remains greater than the THG intensity of β-carotene liposomes.

3.3.5 Conclusions

The third-order nonlinear optical properties of violaxanthin, neoxanthin, lutein, β-carotene, zeaxanthin, canthaxanthin and astaxanthin, were measured. The difference in chain length and the presence of epoxide functional groups revealed that the second hyperpolarizability is influenced more by the presence of epoxides than the increase in the length of the conjugated π electron system of polyenes within the range of 9 to 13 conjugated double bonds. Furthermore, photobleach-free imaging of lipid vesicles with incorporated carotenoids was performed to demonstrate that labeling of biological structures is feasible and induces high contrast in the nonlinear optical microscope.

Overall, this study demonstrates that the THG enhancement by natural carotenoids can serve as the basis for the development of nontoxic labels of biological structures for *in vivo* imaging applications using third harmonic generation microscopy. The next section will focus on studying biological structures that naturally contain carotenoids in the form of aggregates.

3.4 Carotenoid Aggregates as Harmonophores

3.4.1 Introduction

Many examples of carotenoid aggregates exist in nature. For instance, within the chromoplasts of orange carrots (*Daucus carota* subspecies *sativus*) and *Narcissus* flowers, the concentration of β-carotene can be so high that β-carotene crystallizes (Köhn, Kolbe et al. 2008). Similarly, in red tomatoes (*Solanum lycopersicum*), large crystals of lycopene form in the chromoplasts. Crystallization occurs inside the lumen of thylakoids and therefore, the β-carotene or lycopene crystals remain enveloped by a membrane (Köhn, Kolbe et al. 2008). Chromoplasts have been found to range in structure from globular, tubular, reticulotubular, membranous, and crystalline types however, it is difficult to evaluate the structure of aggregates present in chromoplasts since a variety of carotenoid aggregates may exist in the same chromoplast (Köhn, Kolbe et al. 2008).

The following discussion is focused on studying the nonlinear optical properties of carotenoid aggregates including H and J aggregates of astaxanthin as well as β-carotene aggregates found naturally in carrots. Further, structural studies of H and J aggregates as well as β-carotene aggregates in carrot were also performed with polarization-dependent SHG and THG microscopy techniques.

3.4.2 H and J Aggregates

Hydrophobic carotenoids are able to form aggregates when present in polar solvent. The formation of carotenoid aggregates is entropy driven where carotenoid aggregates reduce the surface area exposed to water and minimize disruption of the solvation shell of water (Köhn, Kolbe et al. 2008).

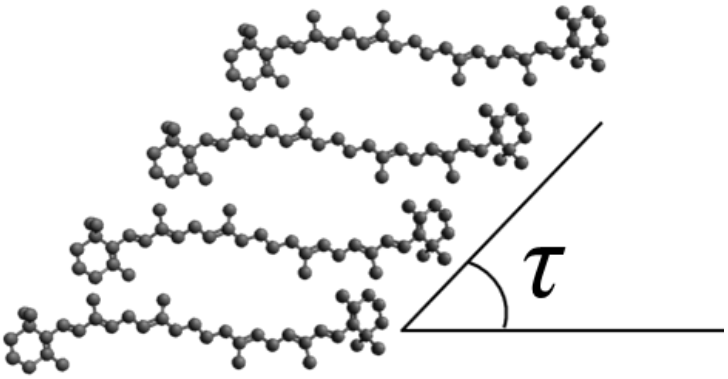

Figure 3.4.1: Possible carotenoid aggregate structure. The formation of H versus J aggregates depend on the slip angle (τ) where structures with τ <32° form J-type aggregates with a bathochromic shift in the absorption spectrum and τ >32° form H-type aggregates with a hypsochromic shift.

The aggregation of carotenoids can be characterized by changes in their absorbance spectra. Carotenoids are able to form H aggregates, descriptive of blue-shifted absorbance bands (hypsochromic) and the loss of vibrational structure of the S_2 excited state (Köhn, Kolbe et al. 2008). The blue shift results from excitonic interaction between carotenoids (Köhn, Kolbe et al. 2008). The carotenoids are closely packed and stacked with the conjugated chains oriented parallel to one another (card-packed arrangement). Carotenoids are also able to form J aggregates, named after E.E. Jelly, one of the first scientists to observe aggregates characterized by red-shifted absorbance bands. Within the J aggregate, the conjugated chains of carotenoids are arranged head-to-tail forming a more loosely packed aggregate. A slip angle (τ) seen in

Figure 3.4.1. of less than 32° describes J aggregates and a slip angle larger than 32° defines H aggregates (Köhn, Kolbe et al. 2008).

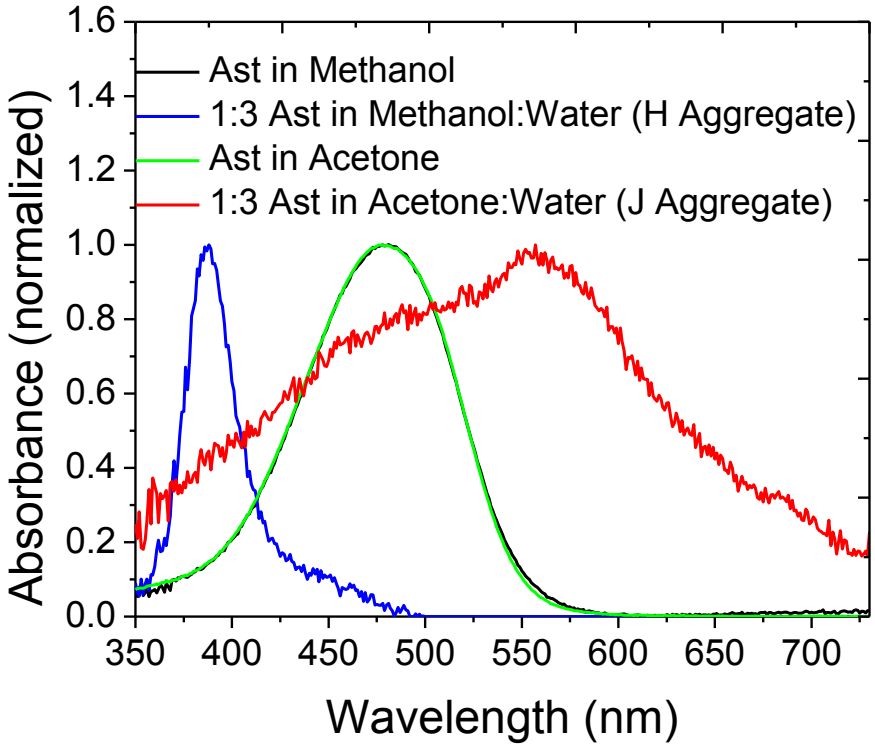

Figure 3.4.2: Normalized absorbance spectra of astaxanthin in methanol and acetone, as well as astaxanthin aggregates. The absorbance spectra of 50 μM astaxanthin in methanol and acetone mixed with water in a ratio of 1:3. Astaxanthin dissolved in methanol and mixed with water results in the formation of H aggregates (Giovannetti, Alibabaei et al. 2009) while astaxanthin dissolved in acetone and mixed with water primarily forms J aggregates (Mori, Yamano et al. 1996).

Using the same concentrations of astaxanthin in two different solvent mixtures (methanol/water and acetone/water), H and J aggregates were produced. As seen in Figure 3.4.2, pure H aggregates were achieved however; both J and H aggregates were present in the acetone/water mixture. The two samples were scanned and simultaneously signals at SHG and THG wavelengths were detected. Therefore, it was assumed that images measured in Figure 3.4.3 originated from SHG and THG signals.

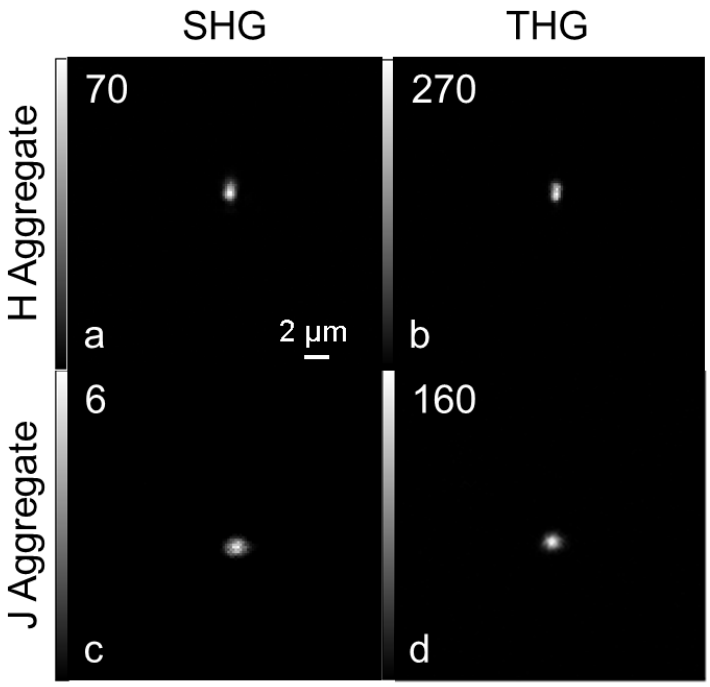

Figure 3.4.3: H and J aggregates of astaxanthin. An H aggregate of astaxanthin imaged with SHG (a) and THG (b) microscopy compared to a J aggregate of astaxanthin imaged with SHG (c) and THG microscopy (d). SHG and THG signals of the aggregates were assumed to be measured.

In general, it was observed that both the H and J aggregate samples generated more THG signal than SHG signal further demonstrating that astaxanthin is a good harmonophore for THG microscopy. The H aggregates seemed to generate more SHG and THG signal than the J aggregates however; further studies such as aggregate size would need to be performed in order to determine whether the interaction between astaxanthin molecules in the H aggregate structure enhance nonlinear optical signals.

3.4.3 Structure of H and J Aggregates

The crystal arrangement of both H and J aggregates of astaxanthin has been previously investigated and both aggregates demonstrate centrosymmetric packing arrangements (Bartalucci, Coppin et al. 2007). Therefore, SHG signal should not be generated from these structures. Since low SHG signal is observed (Figure 3.4.3), most probably it originates from the quadrupole effect (Boyd 2008).

In order to further investigate the organizational structure of astaxanthin within H and J aggregates, the PIPO THG technique was performed. PIPO THG data of an H aggregate of

astaxanthin which is comparable to data also seen for J aggregates of astaxanthin is summarized by contour plots in Figure 3.4.4.

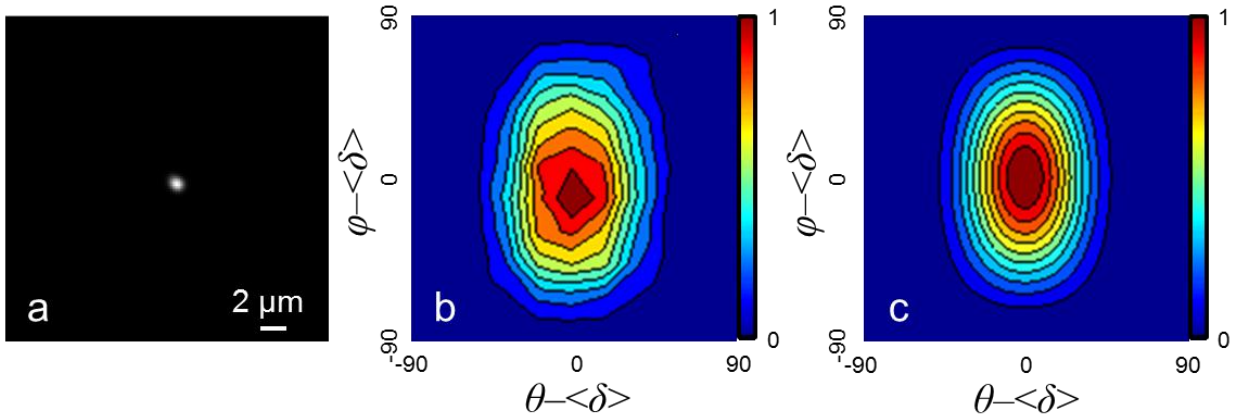

Figure 3.4.4: PIPO THG of an H aggregate of astaxanthin. THG image of an astaxanthin H aggregate (a) along with the measured PIPO THG data (b) and the PIPO THG fit (c).

Fitting of the PIPO THG data was performed with equation (2.3.18). Amongst a number of PIPO THG scans, the values of $\chi^{(3)}_{zzxx}/\chi^{(3)}_{xxxx}$ were found to be small. Since the two ratios, $\chi^{(3)}_{zzxx}/\chi^{(3)}_{xxxx}$ and $\chi^{(3)}_{zzzz}/\chi^{(3)}_{xxxx}$, depend on one another, the value of $\chi^{(3)}_{zzxx}/\chi^{(3)}_{xxxx}$ was fixed between -2 and 2 while $\chi^{(3)}_{zzzz}/\chi^{(3)}_{xxxx}$ was set as a free fitting parameter. The third-order nonlinear optical susceptibility ratios for the astaxanthin H aggregate shown in Figure 3.4.4 were found to be $\chi^{(3)}_{zzxx}/\chi^{(3)}_{xxxx} = 1 \pm 0.4$ and $\chi^{(3)}_{zzzz}/\chi^{(3)}_{xxxx} = 16 \pm 5$ (R-squared value of 0.964). The $\chi^{(3)}_{zzzz}/\chi^{(3)}_{zzxx}$ ratio can be found by fitting for parameters $\chi^{(3)}_{zzzz}/\chi^{(3)}_{xxxx}$ and $\chi^{(3)}_{zzxx}/\chi^{(3)}_{xxxx}$, and subsequently dividing $\chi^{(3)}_{zzzz}/\chi^{(3)}_{xxxx}$ by $\chi^{(3)}_{zzxx}/\chi^{(3)}_{xxxx}$. Therefore, $\chi^{(3)}_{zzzz}/\chi^{(3)}_{zzxx}$ was found to be 16 ± 8. The error was determined by setting bounds such that the overall difference in the R-squared value was 0.001. PIPO THG results suggest that the astaxanthin molecules within an aggregate are very well oriented and each molecule can be approximated by one dominant THG dipole. The values for H aggregates were within error of the values found from fitting PIPO THG data of J aggregates. Therefore, significant differences between the two types of aggregates were not distinguishable. From Figure 3.4.4, it is hypothesized that the structural organization of both H and J aggregates should have one dominant THG dipole however; it is unclear whether coupling between carotenoids would lead to large differences in their third-order nonlinear optical susceptibility axial and cross term components. For instance, in H aggregates, the carotenoids are closely packed and thus, the carotenoids may strongly interact, whereas in J aggregates, the carotenoids are more loosely associated with one another. Further studies are

needed with well characterized and pure aggregates in order to conclude whether nonlinear optical polarization properties of H and J aggregates are discernible from each other.

3.4.4 β-carotene Aggregates in Orange Carrots

β-carotene crystalline aggregates were imaged in thin slices of carrot simultaneously with SHG and THG microscopy as shown in Figure 3.4.5 (a, b, d, e). The β-carotene crystalline aggregates demonstrate high SHG and THG signal intensities where the structures in both images correlate. From these images, it is observed that there is a heterogeneous morphological distribution of β-carotene crystalline aggregates where most of these aggregates are long and thin while others are more spherical in shape.

In order to verify that SHG and THG emission was observed from β-carotene crystalline aggregates, thin slices of orange carrot were submerged in ethanol for 4 hours after which the carrot tissue became transparent and the carotenoids originally present in the carrot had dissolved in ethanol. Imaging of the transparent carrot tissue was performed simultaneously with SHG and THG microscopy seen in Figure 3.4.5 (g, h, j, k). It was observed that the SHG and THG intensities from the transparent carrot tissue are significantly lower than the SHG and THG intensities from the orange carrot tissue, but as well, the SHG and THG signals from the transparent carrot tissue do not correlate. There are spherical structures present in SHG likely due to the presence of starch granules, while in THG, the cell walls can be seen.

Thin slices of orange carrot were boiled for 10 min at 100 °C and imaged with SHG and THG microscopy. Previous experiments with thermally treated samples of sweet potato determined that the sizes and shapes of β-carotene crystalline aggregates did not significantly change from β-carotene crystalline aggregates present in raw sweet potato (Brackmann, Bengtsson et al. 2011). The SHG signal of other structures present in sweet potato such as starch granules decreased due to a loss of crystallinity (Slepkov, Ridsdale et al. 2010, Brackmann, Bengtsson et al. 2011, Cisek 2012). SHG and THG images of β-carotene crystalline aggregates present in raw and boiled orange carrot were not significantly different, however, a loss of SHG signal from starch granules was observed. Starch granules were recognizable due to their shape and very low THG signals (Cisek, Spencer et al. 2009, Cisek 2012).

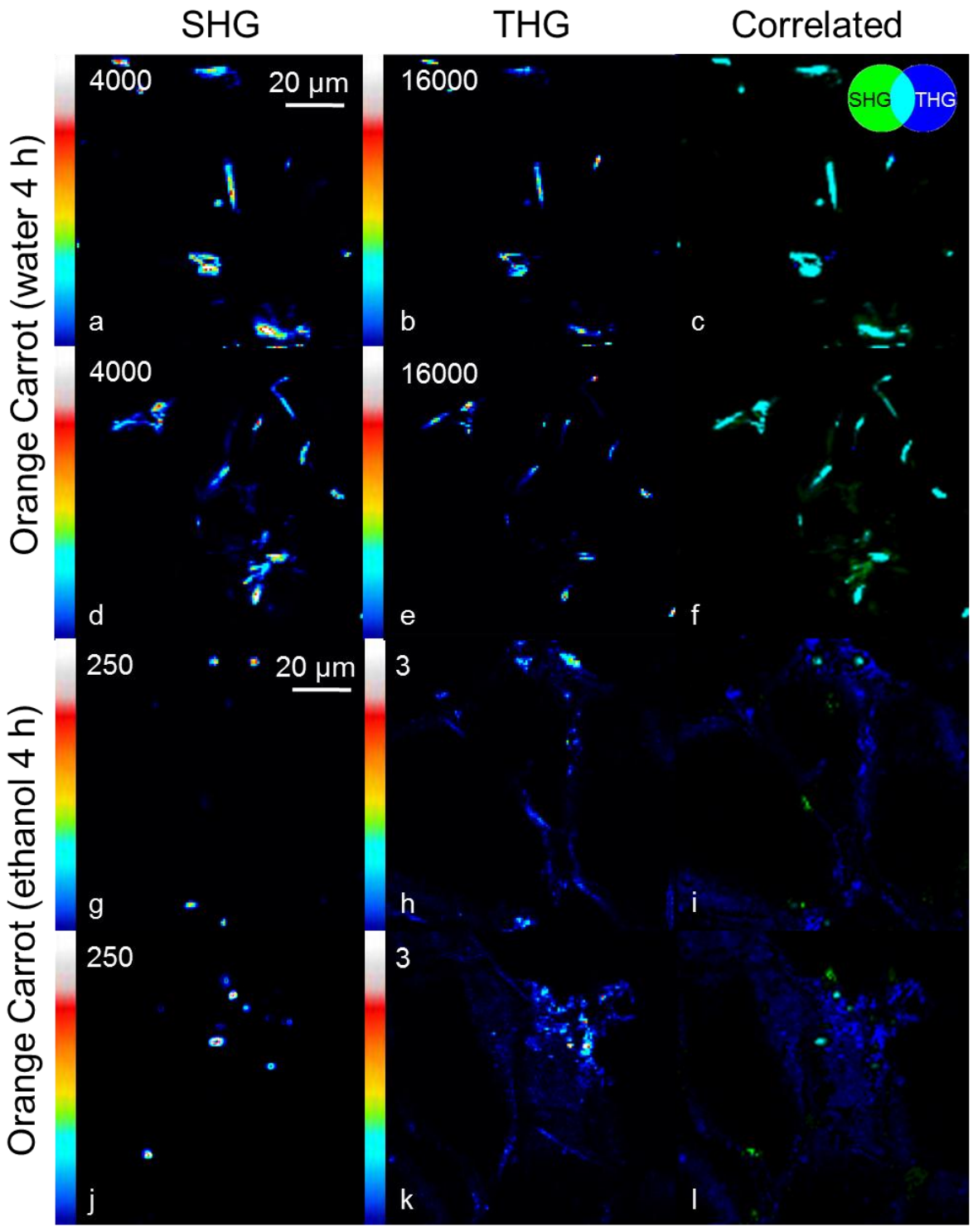

Figure 3.4.5: SHG and THG images of orange carrot immersed in water and ethanol. SHG (a, d), THG (b, e) and their correlated images (c, f) of carrot contained in water for 4 hours and SHG (g, j), THG (h, k) and their correlated images (i, l) of carrot contained in ethanol for 4 hours.

In order to confirm that the SHG signal from the carrot was not due to fluorescence, fluorescence lifetime imaging of the carrot was performed with the SHG filter as well as a bandpass filter between 525 nm to 630 nm (Semrock). This validation was necessary as the maximum fluorescence emission wavelength of trans β-carotene from the S_2 to the S_0 state has been measured in literature at 522±2 nm in *n*-hexane, 535±2 nm in toluene and 565±5 nm in carbon disulfide (Bondarev and Knyukshto 1994). As a result, the maximum fluorescence emission wavelength of trans β-carotene from the S_2 to the S_0 state is highly dependent upon the environment of the carotenoids.

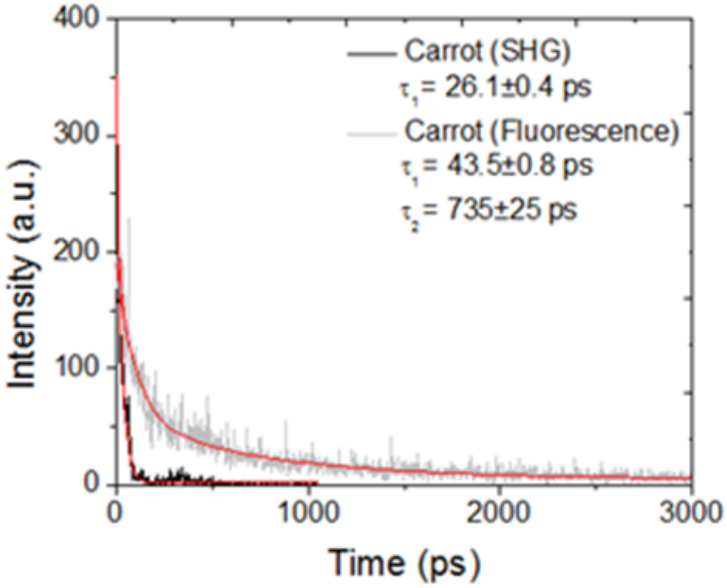

Figure 3.4.6: Fluorescence lifetime imaging exponential decay plots for carrot measured with the SHG filter (509.5-519.5 nm) and a bandpass filter (525-630 nm). The carrot SHG data was fit with a single exponential decay curve while the carrot fluorescence data was fit with a two-exponential decay function. The fluorescence lifetime of the carrot SHG data was 26.1±0.4 ps (R-squared value of 0.96547) while the fluorescence lifetime of the carrot fluorescence data was 43.5±0.8 ps and 735±25 ps (R-squared value of 0.93399).

The 26.1±0.4 ps lifetime of the signal obtained when using the SHG filter was comparable to the instrument response time. When fluorescence lifetime imaging of the carrot was performed with a bandpass filter between 525 nm and 630 nm, the corresponding data could be fit with a two-exponential decay function with two distinct lifetimes, one comparable to the instrument response (43.5±0.8 ps) and a longer lifetime (735±25 ps) attributed to fluorescence. Therefore, the strong signal at the SHG wavelength was in fact due to SHG, whereas the

wavelength of fluorescence emission for trans β-carotene in carrot is shifted more to the red region.

It is surprising that trans β-carotene crystals in carrot produce SHG seeing that trans β-carotene contains an inversion center while structures that give rise to SHG signal should be noncentrosymmetric. Brackmann et al. also demonstrated SHG signal from β-carotene crystals in sweet potato and carrot (Brackmann, Bengtsson et al. 2011). The crystal packing of β-carotene (trans or cis) in a crystal reveals a space group symmetry with an inversion center (Sly 1964, Sterling 1964, Sterling 1964, Senge, Hope et al. 1992, Bartalucci, Delroy et al. 2008). Thus, one possible explanation as to why trans β-carotene crystals in carrots produce SHG signal is that the β-carotene crystals in carrot are not purely composed of β-carotene, but contain carotenoid-protein complexes. Isolation of the carotenoid-protein complexes has been previously performed (Milicua, Juarros et al. 1991, Bryant, Mccord et al. 1992, Zhou, Gugger et al. 1994). Thus, it is possible that the binding of carotenoids to proteins in the carrot causes distortion of the carotenoid molecules. At the moment, this is not known as the carotenoid's conformation in carrot aggregates has yet to be identified. Alternatively, if β-carotene crystals in carrot are inversion symmetric, then β-carotene crystals could induce SHG as a result of the quadrupole effect (Boyd 2008).

3.4.5 Structure of β-carotene Aggregates Investigated by SHG and THG Microscopy

PIPO SHG and THG microscopy was used to investigate the organizational structure of β-carotene crystals in carrot. PIPO measurements were performed on a thin slice of orange carrot. PIPO SHG data is summarized by contour plots shown in Figure 3.4.7.

Fitting of the PIPO SHG data was performed with equation (2.3.14). The $\chi^{(2)}_{ZZZ}/\chi^{(2)}_{ZXX}$ ratio for the β-carotene crystalline aggregates studied in areas of strong SHG signal (Figure 3.4.7 (e, f, g, h)) was found and is shown in Table 3.4-1. The error was determined by setting bounds such that the overall difference in the R-squared value was 0.01.

The $\chi^{(2)}_{ZZZ}/\chi^{(2)}_{ZXX}$ ratio is above 20 for regions of intense SHG signal. Large error values were placed on $\chi^{(2)}_{ZZZ}/\chi^{(2)}_{ZXX}$ in Table 3.4-1 because the fitting of $\chi^{(2)}_{ZZZ}/\chi^{(2)}_{ZXX}$ values above 20 has low sensitivity to the second-order nonlinear optical susceptibility ratios. Nevertheless, ratios

above 20 indicate that excitation along the Z-axis results in a large $\chi^{(2)}$ component along the Z-axis while excitation along the X-axis results in a small $\chi^{(2)}$ component along the Z-axis. This signifies that the alignment of β-carotene molecules is uniaxial where it is presumed that the dominating molecular nonlinear dipole for trans β-carotene is along the conjugated backbone (van Beek, Kajzar et al. 1991). As a result, it can be assumed that a single trans β-carotene molecule is cylindrically symmetric.

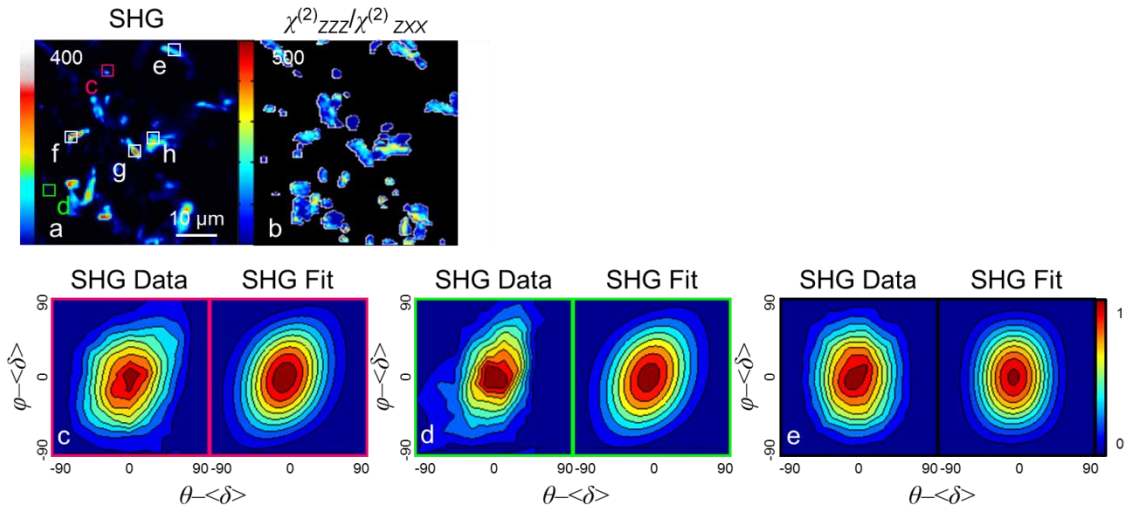

Figure 3.4.7: PIPO plots corresponding to the SHG image of β-carotene aggregates present in carrot. SHG image of β-carotene crystalline aggregates present in carrot (a). The corresponding $\chi^{(2)}_{ZZZ}/\chi^{(2)}_{ZXX}$ values for image (a) where the color bar ranges from a ratio between 1 and 500 (b). Different regions were analyzed to produce PIPO data contour plots. Fits were performed with equation (2.3.14). The contour plots representing regions (c) and (d) are typical of areas which do not demonstrate intense SHG signal, whereas the contour plot shown in (e) is representative of an area of intense SHG signal such as (f, g, h).

The $\chi^{(2)}_{ZZZ}/\chi^{(2)}_{ZXX}$ ratio was found to be below 10 for regions of low SHG signal intensity (Figure 3.4.7 (c, d)). The $\chi^{(2)}_{ZZZ}/\chi^{(2)}_{ZXX}$ ratio changes as a result of the orientation of trans β-carotene molecules to the image plane (Tuer, Krouglov et al. 2011). Regions of high harmonic signal are indicative of trans β-carotene molecules oriented along the scanning plane whereas regions of low harmonic signal are representative of trans β-carotene molecules tilted out of the scanning plane.

Fitting of the PIPO THG data was also performed in the same areas as the PIPO SHG data with equation (2.3.18). The values of $\chi^{(3)}_{ZZXX}/\chi^{(3)}_{XXXX}$ were found to be small for regions of intense SHG and THG signal (Figure 3.4.7 (d, e, f, g)). Similar to the PIPO THG fits of H

aggregates, the value of $\chi^{(3)}_{zzxx}/\chi^{(3)}_{xxxx}$ was fixed between -2 and 2 while $\chi^{(3)}_{zzzz}/\chi^{(3)}_{xxxx}$ was set as a free fitting parameter.

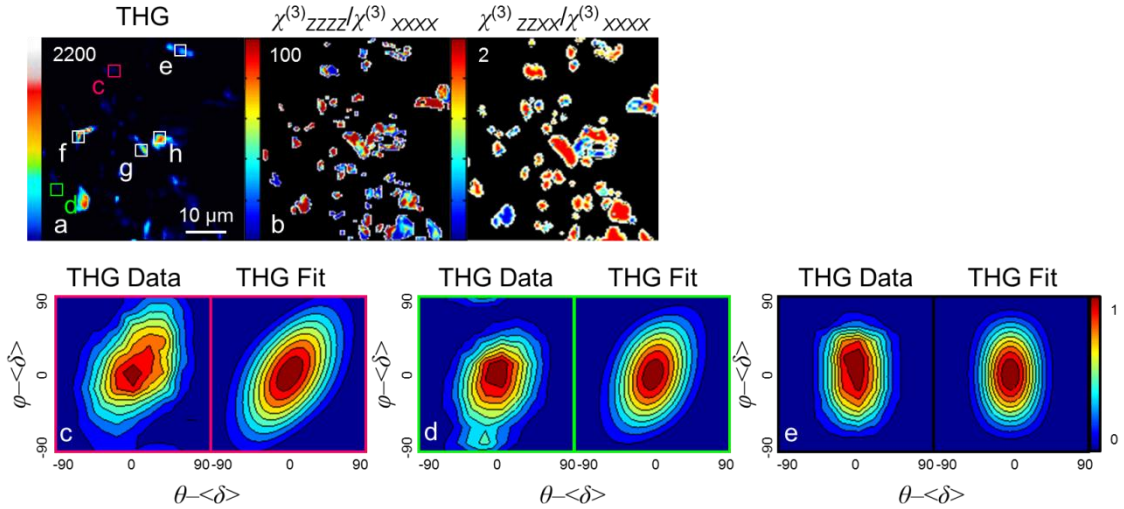

Figure 3.4.8: PIPO plots corresponding to the THG image of β-carotene crystalline aggregates present in carrot. THG image of β-carotene crystalline aggregates present in carrot (a). The corresponding $\chi^{(3)}_{zzzz}/\chi^{(3)}_{xxxx}$ values for image (a) where the color bar ranges from a ratio between 1 to 100 as well as the $\chi^{(3)}_{zzxx}/\chi^{(3)}_{xxxx}$ values where the color bar ranges from a ratio between -2 and 2 (b). Different regions were analyzed to produce PIPO data contour plots. Fits were performed with equation (2.3.18). The contour plots representing regions (c) and (d) are typical of areas, which do not demonstrate intense THG signal whereas the contour plot shown in (e) is representative of an area of intense THG signal such as (f, g, h).

A large $\chi^{(3)}_{zzzz}/\chi^{(3)}_{xxxx}$ ratio value indicates that excitation along the Z-axis results in a large $\chi^{(3)}$ component along the Z-axis while excitation along the X-axis results in a small $\chi^{(3)}$ component along the X-axis. Similar to the PIPO SHG data, this signifies that the alignment of trans β-carotene molecules is uniaxial. Although the molecular dipoles are oriented in Z, a nonzero contribution in X is expected and is additive with several trans β-carotene molecules. Therefore, a smaller but substantial ($\chi^{(3)}_{xxxx}$) is expected. As a result, the cross term, $\chi^{(3)}_{zzxx}$, represents coupling between the two axes. From the fits, $\chi^{(3)}_{zzxx}/\chi^{(3)}_{xxxx}$ is small and $\chi^{(3)}_{zzzz}/\chi^{(3)}_{zzxx}$ is large.

For areas in Figure 3.4.8 where the THG signal is low (Figure 3.4.8 (c, d)), the values of $\chi^{(3)}_{zzxx}/\chi^{(3)}_{xxxx}$ were found to be small. Again, the $\chi^{(3)}_{zzxx}/\chi^{(3)}_{xxxx}$ values were fixed between -2 and 2 while $\chi^{(3)}_{zzzz}/\chi^{(3)}_{xxxx}$ was set as a free fitting parameter. In Figure 3.4.8 (c, d), the $\chi^{(3)}_{zzzz}/\chi^{(3)}_{xxxx}$ values were found to be smaller than the values found in Figure 3.4.8 (e, f, g, h). The lower $\chi^{(3)}_{zzzz}$ component signifies that the average orientation of trans β-carotene molecules

in the focal volume are not oriented along the scanning plane. As a result, the cross term, $\chi^{(3)}_{zzxx}$, is larger and overall, the $\chi^{(3)}_{zzzz}/\chi^{(3)}_{zzxx}$ ratio was found to be smaller than the same ratio in regions of higher SHG and THG signal.

Table 3.4-1: Summary of fitting parameters from PIPO SHG and PIPO THG. R-squared values for SHG fits were at least 0.92 and R-squared values for THG fits were at least 0.93.

Sample Spot	$\chi^{(2)}_{zzz}/\chi^{(2)}_{zxx}$	$\chi^{(3)}_{zzzz}/\chi^{(3)}_{xxxx}$	$\chi^{(3)}_{zzzz}/\chi^{(3)}_{zzxx}$	$\chi^{(3)}_{zzxx}/\chi^{(3)}_{xxxx}$
c	3.8±0.8	5±3	5.0±3.6	1±0.4
d	7.5±1.3	7±4	7.0±4.9	1±0.4
e	190±170	27±11	-90±130	-0.3±0.4
f	250±230	42±31	42±35	1±0.4
g	120±110	23±11	23±14	1±0.4
h	220±200	15±6	-50±140	-0.3±0.4

The nonlinear optical susceptibility ratios were determined from contour plots which were shifted to the center assuming ψ=90°. The $\chi^{(3)}_{zzxx}/\chi^{(3)}_{xxxx}$ parameter was fixed between -2 and 2, and $\chi^{(3)}_{zzzz}/\chi^{(3)}_{xxxx}$ was set as a free fitting parameter.

Isolated chromoplasts from carrot were also studied with PIPO SHG and PIPO THG. Isolated chromoplasts demonstrated similar PIPO SHG and PIPO THG plots to that of carrot with similar second-order and third-order nonlinear optical susceptibility ratios.

3.4.6 Three-dimensional Orientation of Trans β-carotene Molecules in Carrots

The average orientation of β-carotene molecules within a focal volume was extracted from polarization-dependent SHG (Figure 3.4.9 (a, g)) and THG (Figure 3.4.9 (d, j)) carrot images where data only with an R-squared value of 0.8 and greater was considered because the fitting uncertainty was sufficiently low for meaningful analysis. Calibration of the orientation was performed with collagen from a rat tail tendon (Tuer, Akens et al. 2012).

An example of the orientation of β-carotene molecules in crystalline aggregates found in a slice of orange carrot is shown in Figure 3.4.9 (b) regions (i) and (ii) for SHG and Figure 3.4.9 (e) regions (i) and (ii) for THG. In region (i), the orientation of β-carotene molecules was found to be about 13°±2° away from the aggregate axis in the SHG image and 15°±2° away in the THG image. In region (ii), the orientation of β-carotene molecules was found to be about 11°±2° away from the aggregate axis in the SHG image and 10°±2° away in the THG image.

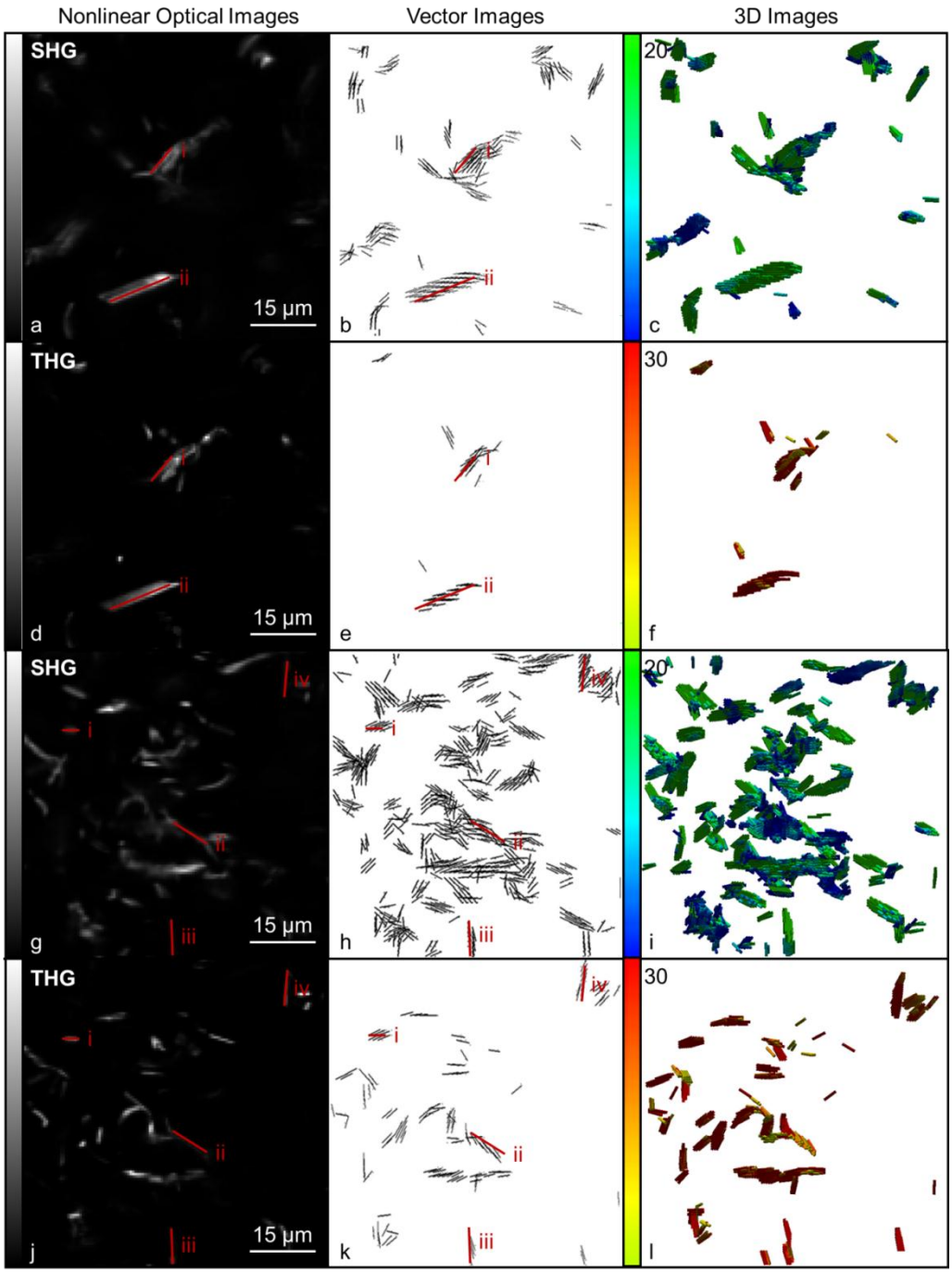

Figure 3.4.9: Vector image and 3D representations of the average orientation of β-carotene molecules in a focal volume in crystalline aggregates. SHG images (a, g) and the corresponding THG images (d, j) of thin slices of orange carrot containing trans β-carotene crystalline aggregates. A vector image of the average orientation of trans β-carotene molecules in a focal volume is represented for SHG (b, h) and THG (e, k). A 3D representation of the average orientation of trans β-carotene molecules in a focal volume is also shown for SHG (c, i) and THG (f, l).

A second example is shown in Figure 3.4.9 (h) regions (i), (ii), (iii), and (iv) for SHG and Figure 3.4.9 (k) regions (i), (ii), (iii), and (iv) for THG. In region (i), the orientation of β-carotene molecules was found to be about 24° away from the aggregate axis in the SHG image and 25°±2° away in the THG image. In region (ii), the orientation of β-carotene molecules was found to be about 21°±2° away from the aggregate axis in the SHG image and 19°±2° away in the THG image. In region (iii), the orientation of β-carotene molecules was found to be about 24°±2° away from the aggregate axis in the SHG image and 25°±2° away in the THG image while in region (iv), the orientation of β-carotene molecules was found to be about 12°±2° away from the aggregate axis in the SHG image and 14°±2° away in the THG image.

The orientation of β-carotene molecules from the aggregate axis varies largely. In rare occasions (samples are not shown), the orientation of β-carotene molecules from the aggregate can be as high as 70°. According to Frey-Wyssling and Schwegler, trans β-carotene molecules in carrots arrange to form sheets (Frey-Wyssling and Schwegler 1965). The growth of sheets in a single direction can cause the formation of narrow ribbons referred to as needles whereas more broad-like ribbons can elongate and wind into coils forming helical tubes (Frey-Wyssling and Schwegler 1965). The reason why different angles are observed for the orientation of β-carotene molecules from the aggregate axis is due to the fact that sheets of β-carotene molecules are folded in a different way and have a different twist with respect to their projection on the image plane. If multiple sheets that are folded appear in the same focal volume, then β-carotene molecules may be oriented in several directions. Therefore, due to coherent summation of the nonlinear dipoles at different orientations, the resulting cylindrical axis of the voxel may assume various orientations with respect to the apparent axis of the aggregate (Tuer, Akens et al. 2012).

From the vector images in Figure 3.4.9, it is difficult to assess the overall structure of the carrot aggregates however; a three-dimensional representation may be constructed from knowledge of the second-order nonlinear optical susceptibility ratio ($\chi^{(2)}_{ZZZ}/\chi^{(2)}_{ZXX}$) by applying equation (2.3.10), the third-order nonlinear optical susceptibility ratio ($\chi^{(3)}_{ZZZZ}/\chi^{(3)}_{XXXX}$) by applying equation (2.3.15) and extracting the angle α as shown in Figure 2.3.1.

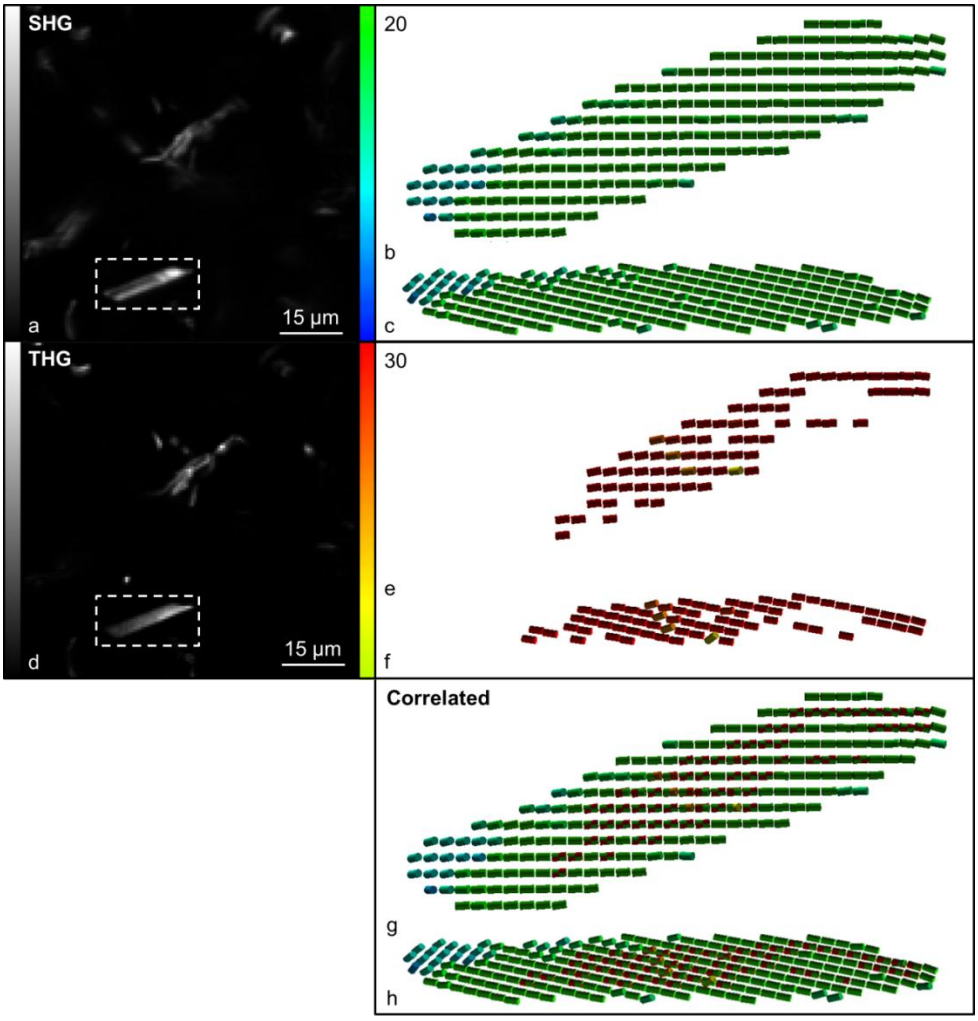

Figure 3.4.10: A 3D representation of the average orientation of β-carotene molecules in a crystalline aggregate demonstrating a ribbon shape. SHG image (a) and the corresponding THG image (d) of trans β-carotene crystalline aggregates present in carrot. A specific area is selected (indicated by a white box) and the close-up of the 3D representation of the average orientation of trans β-carotene molecules in a focal volume corresponding to the aggregate lying flat (b) and sideways (c) is shown from analysis of PIPO SHG. The color bar represents $\chi^{(2)}_{ZZZ}/\chi^{(2)}_{ZXX}$ ratios ranging between 1 and 20. The equivalent 3D representation from PIPO THG data is shown for the aggregate lying flat (e) and sideways (f). The color bar represents $\chi^{(3)}_{ZZZZ}/\chi^{(3)}_{XXXX}$ ratios ranging between 0 and 30. The correlated 3D representation for the aggregate lying flat (g) and sideways (h) are shown.

The colored scale bar in Figure 3.4.9 for the 3D images generated from SHG (Figure 3.4.9 (c, i) indicates the $\chi^{(2)}_{ZZZ}/\chi^{(2)}_{ZXX}$ ratio for each voxel where the voxel is represented as a cylinder. A maximum $\chi^{(2)}_{ZZZ}/\chi^{(2)}_{ZXX}$ ratio of 20 was chosen as the fitting of $\chi^{(2)}_{ZZZ}/\chi^{(2)}_{ZXX}$ values above 20 has low sensitivity to the susceptibility ratios. As a result, voxels with $\chi^{(2)}_{ZZZ}/\chi^{(2)}_{ZXX}$ ratios of 20 and over are represented by dark green cylinders which are oriented flat on the XZ

plane. All $\chi^{(2)}_{ZZZ}/\chi^{(2)}_{ZXX}$ ratios between 1 and 20 are represented by cylinders which are tilted out of the XZ plane. It should be further noted that since the equations for the ratios $\chi^{(2)}_{ZZZ}/\chi^{(2)}_{ZXX}$ and $\chi^{(3)}_{ZZZZ}/\chi^{(3)}_{XXXX}$ are even functions, a degeneracy exists between the sign of α and therefore, Figure 3.4.9 (c) only demonstrates one possible tilt of the cylindrical axis out of the image plane for each pixel (Tuer, Akens et al. 2012). The 3D images constructed from PIPO THG fits (Figure 3.4.9 (f, l)) indicate the $\chi^{(3)}_{ZZZZ}/\chi^{(3)}_{XXXX}$ ratio for each voxel. A maximum $\chi^{(3)}_{ZZZZ}/\chi^{(3)}_{XXXX}$ ratio of 30 was chosen as the highest values $\chi^{(3)}_{ZZZZ}/\chi^{(3)}_{XXXX}$ seen in Table 3.4-1 was about 30. A close-up of the 3D orientation of a specific aggregate from Figure 3.4.9 (i, l) was chosen and is shown in Figure 3.4.10.

The correlated 3D image in Figure 3.4.10 (g, h) resembles a ribbon structure where there are regions within the aggregate that are lying flat in the XZ plane represented by the green cylinders in Figure 3.4.10 (b, c) for SHG and red cylinders in Figure 3.4.10 (e, f) for THG. Areas within the aggregate where the β-carotene molecules are tilted out of the XZ plane analogous to the crinkling of a ribbon are represented by lower ratio values and thus blue cylinders in Figure 3.4.10 (b, c) for SHG and the yellow cylinders in Figure 3.4.10 (e, f) for THG. However, in THG, only structures which are in or tilted slightly out of the XZ plane are seen. The reason for this is because as the aggregate structure rotates more out of the XZ plane, the THG signal decreases faster than the SHG signal. This is exemplified in Figure 3.4.11 where for SHG (Figure 3.4.11 (a)), at half the initial $\chi^{(2)}_{ZZZ}/\chi^{(2)}_{ZXX}$ value, the corresponding α angle is about ~45° whereas for THG (Figure 3.4.11 (b)), at half the initial $\chi^{(3)}_{ZZZZ}/\chi^{(3)}_{XXXX}$ value, the angle α is about ~34°. Thus, if the aggregate structure is too much out of the plane, it is no longer observed in THG and, as a result, SHG shows a larger range of the tilt angles.

As mentioned earlier, Frey-Wyssling and Schwegler proposed that trans β-carotene molecules in carrots arrange to form sheets and subsequently ribbons (Frey-Wyssling and Schwegler 1965). In Figure 3.4.10 (g, h) images corresponding to the correlated 3D SHG and THG data is shown and these images are believed to resemble a ribbon. From Figure 3.4.10 (h) it is believed that the β-carotene molecules are mostly lying flat in the XZ plane except in the far left region of the ribbon at which point, the molecules are pointing about 40° out of the XZ plane.

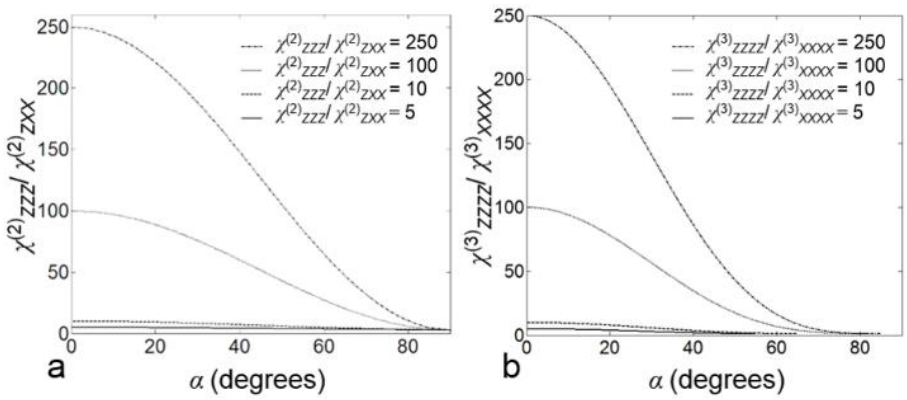

Figure 3.4.11: The effect on $\chi^{(2)}_{zzz}/\chi^{(2)}_{zxx}$ (a) and $\chi^{(3)}_{zzzz}/\chi^{(3)}_{xxxx}$ (b) as the angle α changes. The angle α represents the angle between the projection of a β-carotene molecule on the XZ plane seen earlier in Figure 2.3.1.

For many regions, the 3D representation of the average orientation of trans β-carotene molecules in a focal volume generated from PIPO SHG data agreed with the 3D representation generated from PIPO THG data. However, certain areas did show disagreement such as the β-carotene crystalline aggregate seen in Figure 3.4.12 (a, d).

In the correlated 3D image of the average orientation of trans β-carotene molecules in a focal volume (Figure 3.4.12 (g)), there are certain areas where the orientation (both the α and δ angles) determined by PIPO SHG do not agree with the orientation determined by PIPO THG. Since β-carotene molecules in carrots arrange to form sheets and subsequently ribbons, then these areas where the orientations do not match are likely regions where the ribbons fold. In Figure 3.4.12 (e, f), the areas represented by red cylinders also match the orientation of the same areas seen in Figure 3.4.12 (b, c). These areas in general, are long and can be thought of as a single ribbon. However, the orientation of the yellow cylinders seen in Figure 3.4.12 (e, f) do not match the corresponding areas in Figure 3.4.12 (b, c). This region could be imagined as a region where a ribbon folds underneath or overtop of itself, changing direction, resulting in a voxel that contains two ribbon layers spaced apart, with an angle between the layers. The second-order and third-order nonlinear optical susceptibility tensor components describing such a voxel are the results of the coherent summation of the tensor components, and hence the orientation and phase differences due to the distance between the layers influence the orientation and symmetry. It has been previously found that asymmetry as determined by a PIPO SHG plot exists for overlapping collagen fibers within the same voxel (Tuer, Akens et al. 2012). However, the signal-to-noise ratio in the example β-carotene crystalline aggregate shown in Figure 3.4.12 was too low to

determine asymmetry within the PIPO SHG data. Further, this aspect should be investigated to determine whether asymmetry would also occur with PIPO THG. Future controlled experiments should be performed where PIPO SHG and PIPO THG data is collected from a sample of a single β-carotene crystalline aggregate that is tilted with respect to the XZ plane at known angles in order to better interpret PIPO data from β-carotene crystalline aggregates *in vivo*.

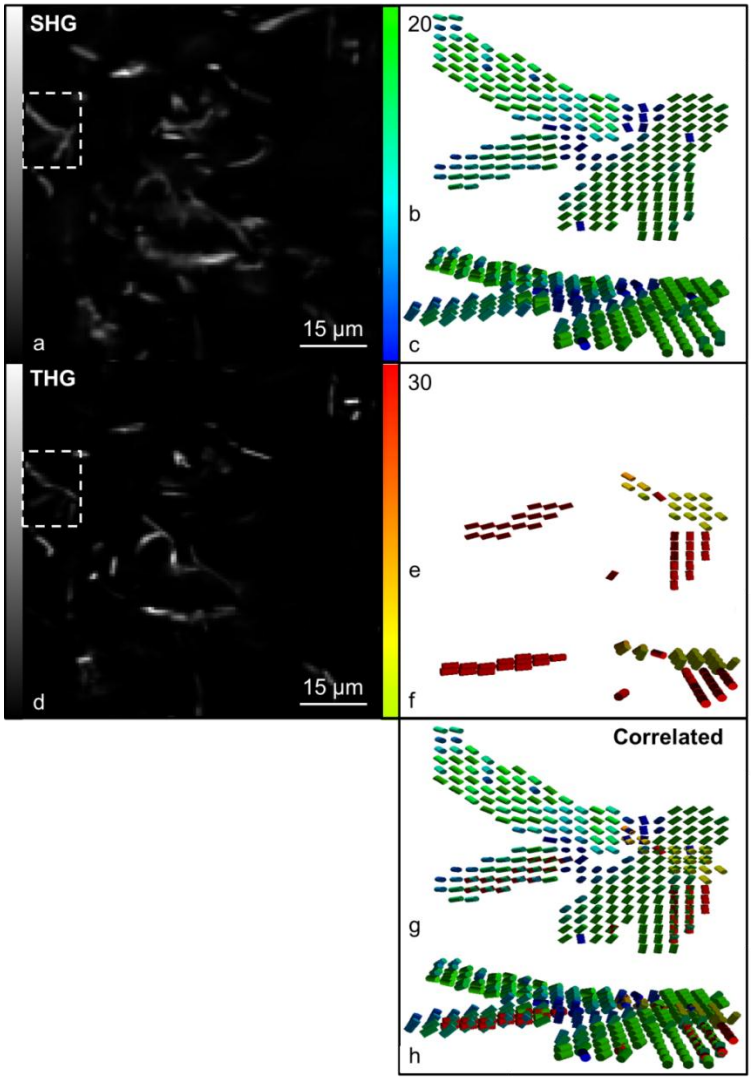

Figure 3.4.12: A 3D representation of the average orientation of β-carotene molecules in a crystalline aggregate demonstrating inconsistencies between 3D representations obtained from PIPO SHG data versus PIPO THG data. SHG image (a) and the corresponding THG image (d) of trans β-carotene crystalline aggregates found in orange carrot. A specific area is indicated by a white frame and the 3D representation of the average orientation of trans β-carotene molecules in a focal volume is shown. The aggregate is shown lying flat (b, e, g) and sideways (c, f, h) generated from PIPO SHG, PIPO THG and correlated data.

In a large number of cases, the β-carotene axis orientation is almost along the ribbon axis. For example, in Figure 3.4.9, all the angles measured in the designated areas were found to be less than 32°. As was mentioned in section 3.4.2, these slip angles are indicative of J aggregates. An absorption spectrum of isolated chromoplasts containing β-carotene crystalline aggregates was taken to verify this observation.

The absorption spectrum seen in Figure 3.4.13 demonstrates that the β-carotene found in chromoplasts has an absorption band that is red shifted as compared to β-carotene dissolved in acetone. Previously, the 0-0 absorption band of crystalline β-carotene has also been shown to be red shifted when compared to β-carotene dissolved in hexane (Gaier, Angerhofer et al. 1991). Therefore, β-carotene predominantly forms J aggregates in orange carrot chromoplasts.

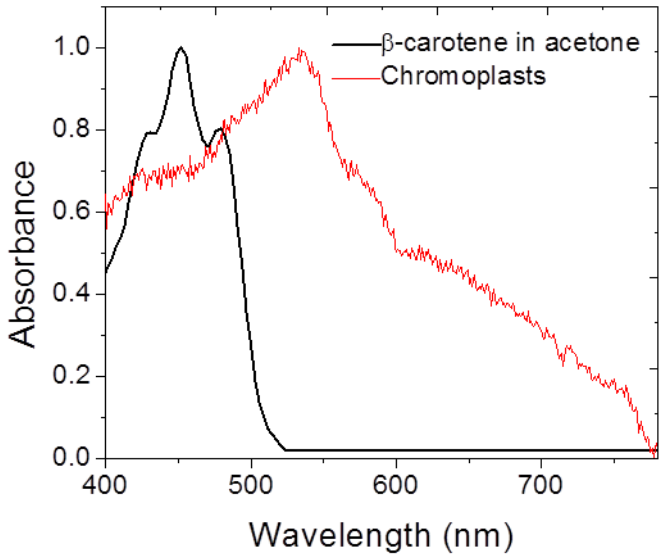

Figure 3.4.13: Absorption spectra of β-carotene and isolated chromoplasts from orange carrots. Isolated chromoplasts from orange carrot have an absorption band that is red shifted compared to β-carotene dissolved in acetone.

3.4.7 Conclusions

Polarization-dependent SHG and THG microscopy can be used to investigate the organizational structure of carotenoids in biological samples. Specifically, SHG and THG microscopy was used to study the orientation of β-carotene molecules within an aggregate contained in the chromoplast of carrots. Polarization-dependent SHG and THG studies of carrot revealed one dominant SHG and THG dipole signifying that molecular orientation can be studied in these aggregates. Similarly, PIPO THG studies of astaxanthin H and J aggregates also revealed that the

molecules are oriented along a single axis. This technique may be beneficial in structural studies of molecular aggregates with cis or trans isomers of carotenoids. The structural characterization of carotenoid aggregates can be applied for the study of carotenoid morphologies. An example includes the characterization of carotenoid morphologies in vegetables since it has been suggested that carotenoids are absorbed easier by humans when the chromoplast adopts a round structure versus the crystalline structure found in carrots (de Pee, West et al. 1998, Brackmann, Bengtsson et al. 2011).

3.5 Summary and Outlook

The third-order nonlinear optical properties of a number of carotenoids were explored. The large second hyperpolarizability values and the non-toxicity make them attractive for the application of harmonophore labeling. Due to the hydrophobic nature of carotenoids, liposomes containing carotenoids were explored as potential labels. Continuous photobleach-free imaging of the carotenoid incorporated liposomes was demonstrated for over 20 minutes. Thus, carotenoid liposomes are appealing harmonophore carriers and application of these harmonophores for labeling will be demonstrated in Chapter 6.

Natural carotenoid aggregates as well as H and J aggregates were also studied. Crystalline β-carotene aggregates found in orange carrot was imaged with both SHG and THG microscopy. Polarization-dependent SHG and THG microscopy was used to identify the organizational structure of β-carotene crystalline aggregates in carrot. Polarization-dependent SHG and THG studies revealed that β-carotene molecules are very well oriented with one dominant nonlinear dipole. Future studies should focus on assessing carotenoid aggregate morphology in different fruits and vegetables by SHG and THG microscopy where it has been suggested that carotenoids are more bioavailable when the chromoplast adopts a round structure versus the crystalline structure found in carrots.

Chapter 4
Chlorophylls[3]

4.1 An Introduction to Chlorophylls

4.1.1 The Molecular Structure of Chlorophylls

The term chlorophyll was introduced in 1818 (Pelletier and Caventou, 1818) to describe the pigments extracted from leaves with organic solvents. Chlorophyll is of Greek origin and means the green (*chloros*) of leaves (*phyllos*). These green pigments belong to a distinct group of cyclic tetrapyrrole compounds which may consist of the porphyrin, chlorin or bacteriochlorin. In addition to the macrocyclic tetrapyrrole, chlorophylls also contain an additional fifth isocyclic ring, as well as a long phytol chain. Lastly, chlorophylls typically contain a central magnesium ion within the tetrapyrrole.

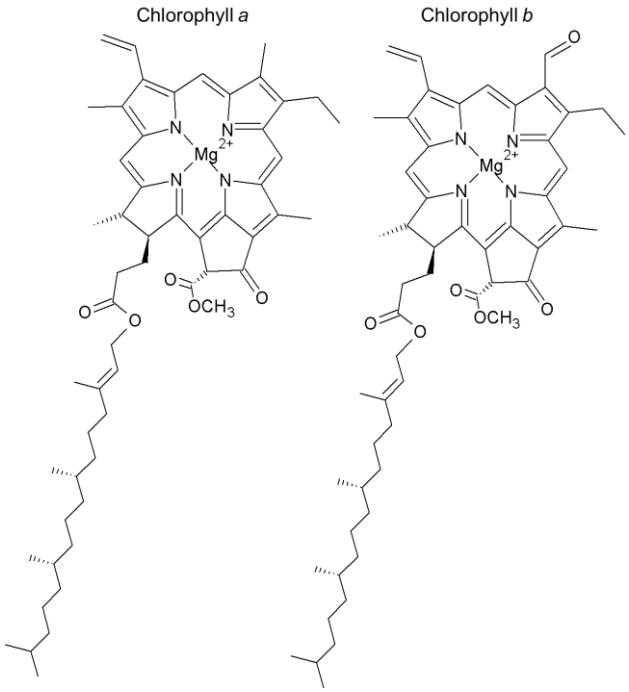

Figure 4.1.1: The molecular structure of chlorophylls *a* and *b*.

[3]Parts of the following chapter were adapted from a published paper. Reprinted from Analytica Chimica Acta, 755, Tokarz, D., Cisek, R., Prent, N., Fekl, U., and Barzda, V. Measuring the molecular second hyperpolarizability in absorptive solutions by the third harmonic generation ratio technique, 86-92, Copyright (2012), with permission from Elsevier. The specific contributions made by all authors are presented in the Statement of Contributions section on page 142.

Nearly 100 different chlorophylls are known today however, this chapter will concentrate on two specific chlorophylls including chlorophyll *a* and chlorophyll *b*, which are present in abundance in pigment-protein complexes of photosynthetic organisms. Chlorophylls *a* and *b* are very similar in structure where the only difference is a methyl substituent on the chlorin macrocycle of chlorophyll *a* versus a formyl substituent at this position for chlorophyll *b*. These small changes in structure lead to large spectral differences which will be explored in the next section.

4.1.2 The Absorbance Properties of Chlorophylls

The main features of the absorption spectra of chlorophylls consists of two-strongly allowed transitions in the blue spectral region referred to as the Soret band (B band) and two weaker transitions in red or near IR region referred to as the Q band. These bands arise from π to π* transitions of four frontier orbitals. A band of each pair is polarized along the X-axis defined as the pathway between rings B and D seen in Figure 4.1.2 resulting in B_x, and Q_x, as well as the Y-axis defined as the pathway between rings A and C resulting in B_y and Q_y (Kobayashi, Akiyama et al. 2010).

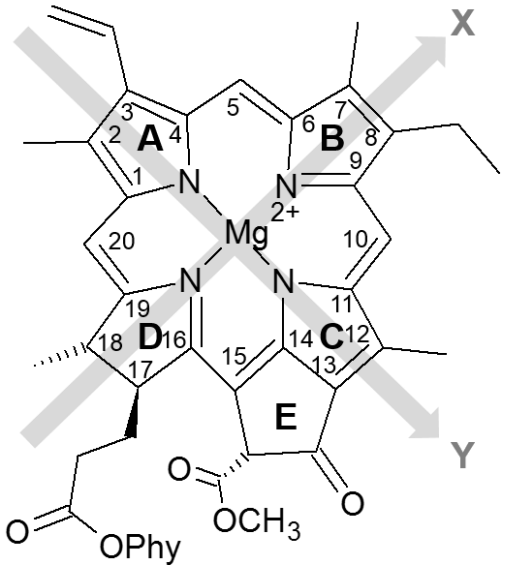

Figure 4.1.2: The X and Y polarization axes of a chlorophyll molecule. An example of the molecular structure of chlorophyll *a* where the arrows represent the direction of the X and Y polarization axes. The carbon atoms are numbered according to IUPAC-IUB nomenclature and Phy refers to the phytol chain.

In chlorophyll *a*, the absorption spectrum is characterized by two strong overlapping Soret bands at about 430 nm and a relatively strong Q_y band near 680 nm with a weak Q_x band near 550 nm. Although chlorophyll *a* and *b* possess the same chlorin macrocycle and long chain alcohol at carbon 17 of the phtyol chain, chlorophyll *a* and *b* possess different substituents on ring B. Compared with chlorophyll *a*, the Soret bands of chlorophyll *b* are red-shifted (at 460 nm) and its Q_y band is blue-shifted (at 650 nm) due to the presence of a formyl substituent on carbon 7 within the chlorin macrocycle of chlorophyll *b*. In addition to this, the ratios of the Soret/Q_y band intensities show remarkable differences between chlorophyll *a* and *b* where this ratio is 1.3 for chlorophyll *a* and 2.8 for chlorophyll *b*.

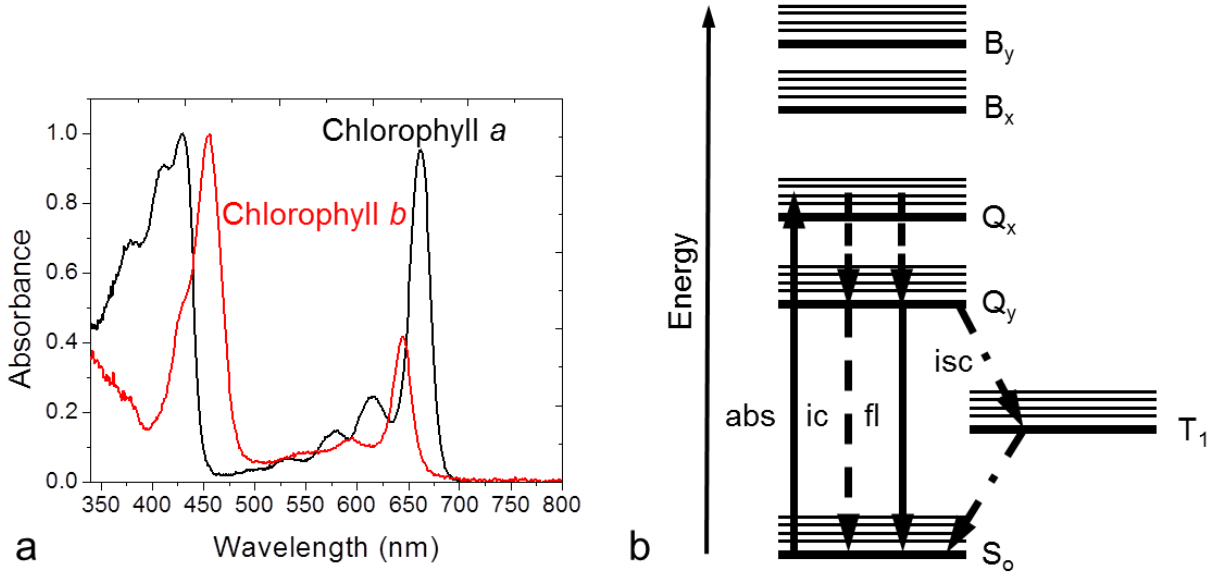

Figure 4.1.3: Absorption spectrum of chlorophylls as well as a typical energy level diagram of chlorophylls. The absorption spectra of chlorophyll *a* and chlorophyll *b* in acetone (a). The energy level diagram used to describe the possible processes that can occur. Note the abbreviations: abs, absorption; ic, internal conversion; fl, fluorescence and isc, intersystem crossing (b).

A diagram of the energy levels and different types of transitions that can occur between electronic states is shown in Figure 4.1.3. Four electronic energy states corresponding to the Soret bands and Q bands are shown. Absorption of blue light corresponds to a transition from the ground state to the Soret states while the absorption of red light corresponds to a transition from the ground state to the Q states.

From both Soret states, excitation energy can be dissipated as heat through internal conversion to the ground state. Similarly, from both Q states, internal conversion to the ground state can also occur. Alternatively, fluorescence can be emitted from the lowest Q state (Q_y). The chlorophyll *a* Q_y state decays largely via fluorescence where the quantum yield is 0.30 in acetone, whereas chlorophyll *b* demonstrates less fluorescence with a 0.09 quantum yield in acetone (Weber and Teale 1957, Seely and Connolly 1986).

4.2 Determination of γ for Chlorophylls

The THG intensities from chlorophyll solution-glass and glass-air interfaces were collected along with the refractive indices of the chlorophyll solutions at the third harmonic wavelength and the fundamental wavelength. The THG intensity ratio (Figure 4.2.1 (a, d)) and the difference in refractive index (Figure 4.2.1 (b, e)) at the third harmonic wavelength versus the fundamental wavelength ($n_{3\omega}$-n_{ω}) is shown in Figure 4.2-1 for two laser wavelengths: 830 nm and 1028 nm.

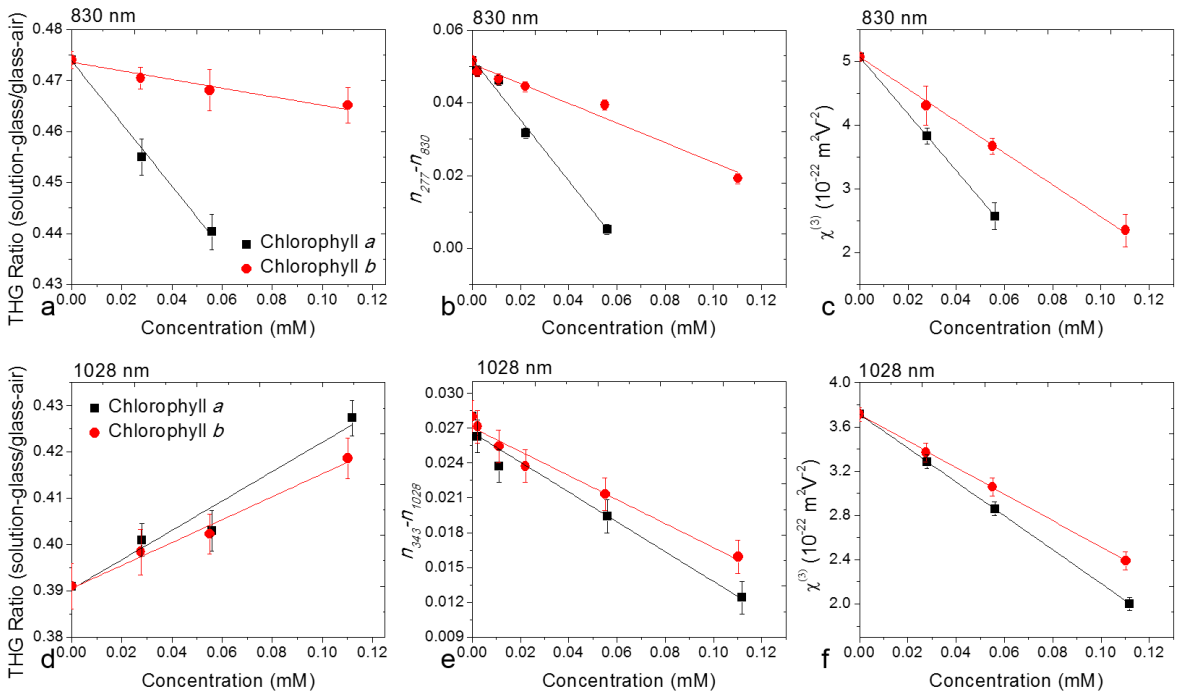

Figure 4.2.1: Data collected for the calculation of the second hyperpolarizability of chlorophylls in acetone at two different fundamental wavelengths. The THG intensity ratio, the difference in refractive index and the third-order nonlinear optical susceptibility for all chlorophylls as a function of concentration is shown for the fundamental wavelength of 830 nm (a, b, c) and 1028 nm (d, e, f).

As seen in Figure 4.2.1 (a, d), the THG intensity ratio for chlorophylls in acetone decreases with increasing concentration at 830 nm excitation while the THG intensity ratio increases with increasing concentration at 1028 nm excitation. At both excitation wavelengths, the difference in refractive index at the third harmonic wavelength and the fundamental wavelength decreases with increasing concentration (Figure 4.2.1 (b, e)).

From data of the THG intensity ratios and the measured refractive indices, the $\chi^{(3)}$ values were calculated and they are shown in Figure 4.2.1 (c, f). As demonstrated in Section 3.2, the sign of the second hyperpolarizability is determined from $\chi^{(3)}$ plots. Since the $\chi^{(3)}$ values of chlorophylls show a declining trend with increasing concentration at both 830 nm and 1028 nm, this means that the phase of the THG emitted from chlorophylls is opposite with respect to the phase of the THG emitted from acetone and the sign of the γ values at both wavelengths is negative. Therefore, at 830 nm, both carotenoids and chlorophylls have negative γ values, but at 1028 nm, the sign of γ changes for carotenoids and as a result, the γ values of carotenoids and chlorophylls are opposite in sign at this wavelength. The γ values for individual chlorophylls at 830 nm and 1028 nm are summarized in Table 4.2-1.

Table 4.2-1: The second hyperpolarizability values for chlorophylls *a* and *b* at 830 nm and 1028 nm.

Chlorophyll	γ (10^{-41} m^2V^{-2}) (830 nm)	γ (10^{-41} m^2V^{-2}) (1028 nm)
Chlorophyll *a*	-270 ± 70	-100 ± 20
Chlorophyll *b*	-150 ± 40	-80 ± 10

The γ values of the chlorophylls are about two orders of magnitude larger than the γ values of the carotenoids. The γ values of chlorophylls are also expected to change for a different solvent. Previous reports of porphyrins demonstrated an increase in the γ value of three to five times when in an acidic medium compared to a neutral medium (Kandasamy, Shetty et al. 1999). Further, in nonpolar solvents, chlorophyll *a* may form oligomers where electronic coupling between chlorophyll rings may lead to increased γ values (Chen 1993). In comparison to polyenes that were discussed in the previous chapter, large changes in γ do not occur upon change of solvent. Previous studies have shown that the γ values for polyenes are not largely affected by changes in solvent polarity unless the polyenes have donor-acceptor functional groups (Marder, Perry et al. 1993).

4.3 The Significance of a Negative γ Value

Several research groups have recognized that it is sufficient for explaining the sign and magnitude of γ if only the ground state as well as two or three excited states in a sum-over-states analysis are considered (Meyers, Marder et al. 1994, Marder, Torruellas et al. 1997, Gubler, Spreiter et al. 1998, Flom 2003). The second hyperpolarizability can be simplified as consisting of 3 terms; one negative term (N) associated with multiple transitions to the one-photon state, a two-photon term (TP) associated with two-photon resonances, and a dipolar term (D) which is zero for centrosymmetric molecules (Marder, Torruellas et al. 1997, Gubler, Spreiter et al. 1998, Flom 2003):

$$\gamma = 24\left(-N + TP + D\right)$$
$$N = \mu_{ge}^4 E_{ge}^{-3}; TP = \sum_{e'} \mu_{ge}^2 \mu_{ee'}^2 E_{ge}^{-2} E_{ge'}^{-1}; D = \mu_{ge}^2 \left(\mu_{ee} - \mu_{gg}\right)^2 E_{ge}^{-3} \quad (4.3.1)$$

where in this expression, *g* represents the ground state, *e* and *e'* represent two excited states, μ is the transition dipole moment and *E* is the transition energy between states.

In one dimensional π electron systems such as centrosymmetric carotenoids, the N term has been shown to be smaller than the two-photon term (Marder, Torruellas et al. 1997). As a result, the γ value of centrosymmetric carotenoids tends to be positive when far from resonance (Marder, Torruellas et al. 1997). However, literature results of both symmetrical and asymmetrical porphyrins have demonstrated that the negative term dominates (Díaz-García, Ledoux et al. 1994, Sastre, Díaz-García et al. 1997, Del Rey, Keller et al. 1998, Rojo, de la Torre et al. 1999). It is believed that this is also the case for chlorophylls which are similar in structure to the porphyrins previously studied as chlorophylls have been proven to have negative γ values. Little information on two-photon states in chlorophylls is available in literature, which is necessary for a detailed understanding of the origin of the optical nonlinearity of chlorophylls.

4.4 Data for Negative and Positive γ Values

Both the THG intensity ratio and the difference in refractive index are measured for the calculation of $\chi^{(3)}$ values and the overall γ value of the harmonophore. In order to better understand how THG intensity ratios and differences in refractive index dictate whether the sign

of the γ value will be positive or negative, a three-dimensional plot was produced where the $\chi^{(3)}$ is plotted versus the THG ratio intensity and the difference in refractive index.

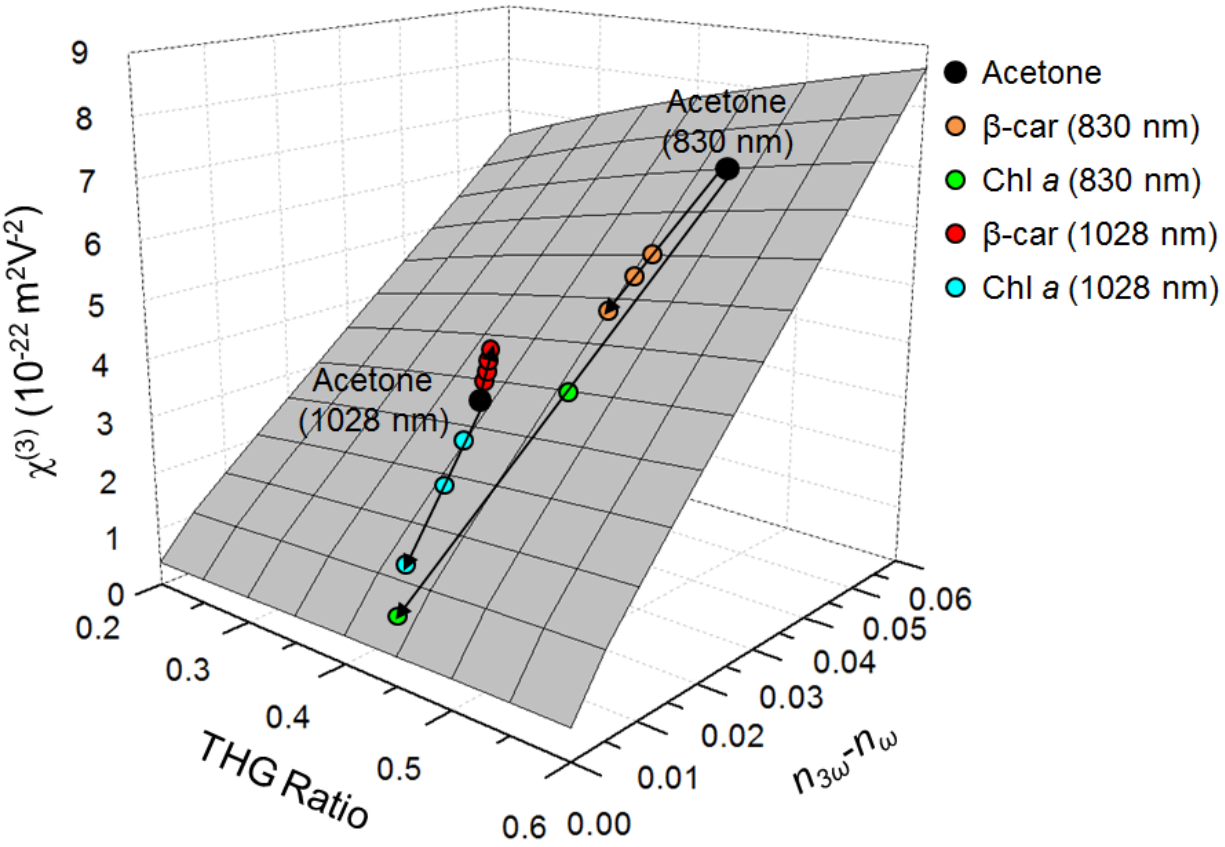

Figure 4.4.1: A three-dimensional plot of $\chi^{(3)}$ versus the THG ratio and the difference in refractive index at the third harmonic wavelength and the fundamental wavelength. As an example, $\chi^{(3)}$ values corresponding to measurements of acetone, and a number of concentrations of β-carotene and chlorophyll *a* were plotted at two fundamental wavelengths: 830 nm and 1028 nm.

In Figure 4.4.1, the $\chi^{(3)}$ values corresponding to acetone, and a number of concentrations of β-carotene and chlorophyll *a* were plotted. At 830 nm, the values of $n_{3\omega}$-n_{ω} for acetone are larger than the corresponding $n_{3\omega}$-n_{ω} values for β-carotene and chlorophyll *a*. As a result, the three-dimensional plot of $\chi^{(3)}$ values from acetone to β-carotene and chlorophyll *a* demonstrate a downward slope. Therefore, with respect to acetone, the γ values of β-carotene and chlorophyll *a* are negative. At 1028 nm, the value of $n_{3\omega}$-n_{ω} for chlorophyll *a* remains smaller than the value of $n_{3\omega}$-n_{ω} for acetone however, the $n_{3\omega}$-n_{ω} value for β-carotene is larger. Therefore, with respect to acetone at 1028 nm, chlorophyll *a* still has a negative γ value, but β-carotene now has a positive γ value.

The difference in refractive index for acetone changes between 830 nm and 1028 nm however, the change in the sign of the γ value for β-carotene between these two wavelengths is not a reflection of the difference in refractive index of acetone changing, but rather results from optical properties of β-carotene. A small amount of β-carotene results in a large change in the value of $n_{3\omega}$-n_{ω}. If one were to extrapolate these points to find the $n_{3\omega}$-n_{ω} for pure β-carotene, the difference between $n_{3\omega}$-n_{ω} at 830 nm versus 1028 nm would be much larger than the difference seen with acetone. This large difference for β-carotene exists because β-carotene absorbs at the third harmonic wavelength of both 830 nm and 1028 nm. Thus, due to resonance, $n_{3\omega}$-n_{ω} changes for β-carotene in line with Kramers-Kronig relations. Therefore, the $n_{3\omega}$-n_{ω} of β-carotene dictates the sign of the γ value. Similarly, at both wavelengths, the $n_{3\omega}$-n_{ω} of chlorophyll *a* changes largely due to absorption at the third harmonic wavelength at both 830 nm and 1028 nm in line with Kramers-Kronig relations however, the γ value of chlorophyll *a* remains negative at both wavelengths.

From Figure 4.4.1, it is obvious that the change in THG ratio has a smaller effect on the calculated $\chi^{(3)}$ value than the change in the difference in refractive index. This was exemplified previously in Chapter 2 Figure 2.2.8 where the concentration of aqueous NaCl was varied from 0 to 3.5 M. The resulting difference in the THG ratio at these concentrations was 0.1 while the corresponding $n_{3\omega}$-n_{ω} values measured at Yb:KGW wavelengths remained constant. As a result, the $\chi^{(3)}$ value of the 3.5 M solution of NaCl only increased by 0.5×10^{-22} m^2V^{-2}.

4.5 Summary and Outlook

The third-order nonlinear optical properties for chlorophyll *a* and chlorophyll *b* were explored. In comparison with data from Chapter 3, both carotenoids and chlorophylls have negative γ values at 830 nm however, at 1028 nm, chlorophylls still have negative γ values while carotenoids have positive γ values. This is consistent with previous reports of negative γ values for metal-containing chlorins and porphyrins (Singh, Vijaya et al. 2001). Since the γ values of chlorophylls were shown to be two orders of magnitude larger than the γ values of carotenoids therefore, chlorophylls may act as better harmonophores for sample labeling in nonlinear optical microscopy.

In plants, carotenoids and chlorophylls are often found together and both play a role in harvesting solar energy. The third-order nonlinear optical properties as a result of the interaction

between carotenoids and chlorophylls will be studied in the following chapter. The third-order nonlinear optical properties of a solution mixture containing carotenoids and chlorophylls, molecules that contain carotenoid-like and chlorophyll-like molecules covalently bonded to one another, as well as photosynthetic pigment-protein complexes will be investigated.

Chapter 5
Interaction Between Carotenoids and Chlorophylls[4]

5.1 Solution Mixture of Carotenoids and Chlorophylls

The $\chi^{(3)}$ values at a number of concentrations were found for a number of carotenoids (demonstrated in Chapter 3) and a couple of chlorophylls (presented in Chapter 4) dissolved in acetone. The $\chi^{(3)}$ values of carotenoids increased with increasing concentration while the $\chi^{(3)}$ values of chlorophylls decreased with increasing concentration at 1028 nm. Thus, in acetone, carotenoids have positive γ values while chlorophylls have negative γ values. This means that the phase of the THG emitted from carotenoids is in phase with the THG emitted from acetone while the phase of the THG emitted from chlorophylls is out of phase with the THG emitted from acetone. This suggests that at a specific concentration of carotenoids and chlorophylls in acetone, the contribution of the THG signal from carotenoids should cancel with the contribution of the THG signal from chlorophylls. In order to explore this effect, different ratios of chlorophyll *a* and β-carotene were mixed in acetone solution. These experiments served as a control by which one can observe that in a solution, the second hyperpolarizabilities of chlorophyll and β-carotene are additive.

In Figure 5.1.1, the THG ratio of pure chlorophyll *a* in acetone increases with increasing concentration. At a ratio of 1:0.27 (15:4) chlorophyll *a* (Chl *a*) to β-carotene (β-car), the THG ratio also increases and shows no significant difference to pure chlorophyll *a*. This ratio corresponds to the number of chlorophylls to carotenoids found in the light-harvesting chlorophyll *a*/*b* pigment-protein complex of photosystem II (LHCII), which will be further discussed in section 5.4.5.

When the mixture contains a ratio of 1:10 chlorophyll *a* to β-carotene, the THG ratio also increases with increasing chlorophyll *a* concentration however; the slope of this line is more

---

[4]Parts of the following chapter were adapted from a published paper. Reprinted (adapted) with permission from Tokarz, D., Cisek, R., Fekl, U., and Barzda, V. (2013) "The molecular second hyperpolarizability of the light-harvesting chlorophyll *a*/*b* pigment-protein complex of photosystem II," Journal of Physical Chemistry B **117**(38): 11069-11075. Copyright (2013) American Chemical Society. The specific contributions made by all authors are presented in the Statement of Contributions section on page 142.

gradual than the slope of pure chlorophyll *a*. Therefore, at this ratio, the effective γ value of the mixture is smaller than the γ value of pure chlorophyll *a*. At a ratio of 1:20 chlorophyll *a* to β-carotene, the THG ratio remains constant. Since the γ values are the same in magnitude, but opposite in sign, THG generated from chlorophyll *a* cancels with the THG generated from β-carotene molecules and the overall THG intensity ratio remains the same as the solvent. This experiment confirms that at 1028 nm, the magnitude of the γ value for 1 chlorophyll *a* molecule corresponds to the magnitude of the γ value for 20 β-carotene molecules. At high concentrations of β-carotene such as at a ratio of 1:42 chlorophyll *a* to β-carotene, the THG ratio decreases with increasing chlorophyll *a* concentration. This trend is reminiscent of the THG ratio of pure β-carotene seen in Figure 3.2.1.

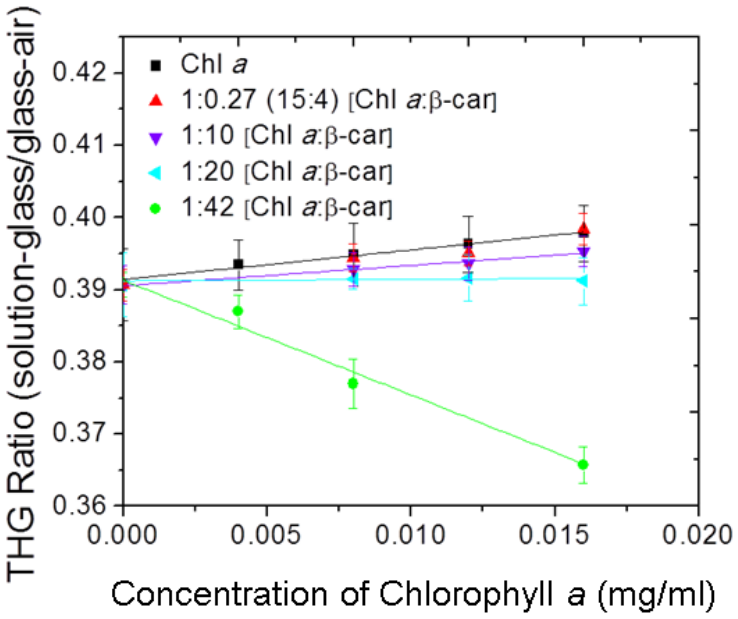

Figure 5.1.1: The THG intensity ratio for a solution of chlorophyll *a* (Chl *a*) in acetone, and a mixture of β-carotene (β-car) and chlorophyll *a* in acetone as plotted against chlorophyll *a* concentration measured at 1028 nm. The ratio of Chl *a* to β-car was kept the same to obtain each experimental curve: 1:0.27 (15:4) Chl *a* to β-car in solution is representative of the number of carotenoids to chlorophylls in LHCII. At a ratio of 1:10 Chl *a* to β-car, the THG ratio increases while at a ratio of 1:20, the THG ratio remains constant and at a ratio of 1:42, the THG ratio decreases. Figure reprinted with permission (Tokarz, Cisek et al. 2013).

Overall, THG ratio studies of a mixture of carotenoids and chlorophylls further demonstrate that the γ value of carotenoids and chlorophylls are opposite in sign and as well, the γ value of chlorophylls are much larger than carotenoids. Therefore, it is predicted that larger γ values should be observed in pigment-protein complexes that contain only chlorophyll pigments.

5.2 Carotenoid and Phthalocyanine Dyads

5.2.1 Introduction to Carotenoid and Phthalocyanine Dyads

In an isotropic solution containing a mixture of carotenoids and chlorophylls, the harmonophores do not interact and therefore, the resultant $\chi^{(3)}$ value of the mixture is the additive sum of the individual $\chi^{(3)}$ values of the carotenoids and chlorophylls. However, it is unclear whether this is the case for chlorophylls and carotenoids when they are bound and interaction is present between the moieties. In order to investigate this, the γ values of covalently bound carotenoid and chlorophyll-like molecules were investigated. Specifically, two carotenoids; one carotenoid with 9 double bonds (9 db carotenoid) and one carotenoid with 10 double bonds (10 db carotenoid) as well as a zinc phthalocyanine molecule and two dyads; one dyad containing the 9 db carotenoid covalently linked to the zinc phthalocyanine molecule (9 db dyad) and one dyad containing the 10 db carotenoid covalently linked to the zinc phthalocyanine molecule (10 db dyad) were studied. The samples were provided by Professors Tom and Ana Moore (Arizona State University).

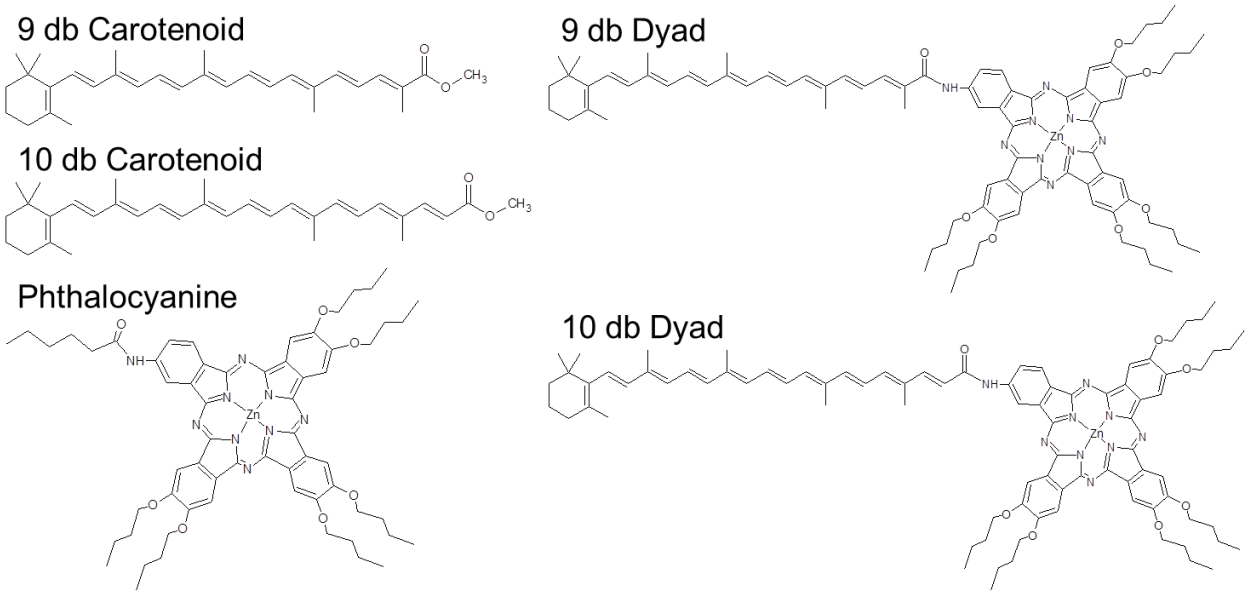

Figure 5.2.1: Covalently bound carotenoid and chlorophyll-like molecules. The molecular structures of 9 double bond (9 db) and 10 double bond (10 db) carotenoids, a zinc phthalocyanine, as well as the 9 db and the 10 db carotenoid covalently linked to the phthalocyanine (9 db dyad and 10 db dyad, respectively).

The synthesis of carotenoid and phthalocyanine dyads are described by Berera, R., et al. (Berera, Herrero et al. 2006). Briefly, in order to synthesize the 9 db dyad, 0.11 mmol of 8'-apo-

β-caroten-8'-oic acid was dissolved in a 3:1 mixture of toluene and pyridine containing one drop of thionyl chloride. The mixture was stirred for 15 min under N_2 and then, the solvent was evaporated. The remaining residue was dissolved in 1:2.4 mixture containing pyridine and chloroform. Then, 0.1 mol of aminophthalocyanine was dissolved in chloroform and added to the acid chloride solution and stirred overnight under N_2. The final product was diluted with chloroform, washed with water, and dried under vacuum. The 10 db dyad was synthesized in a similar fashion (Berera, Herrero et al. 2006).

5.2.2 γ Values

The third harmonic generation intensity ratio from a solution-glass interface and a glass-air interface was measured for the two carotenoids (9 db and 10 db), the phthalocyanine model and the two dyads (9 db and 10 db) dissolved in acetone at 1028 nm (see Figure 5.2.2). The THG intensity ratio of both carotenoids decreases with increasing concentration similar to previous data measured for β-carotene and xanthophylls. The THG intensity ratio of the phthalocyanine model increases with increasing concentration in line with THG intensity ratio data of chlorophylls *a* and *b*. Interestingly, the THG intensity ratio of the dyad decreases with increasing concentration.

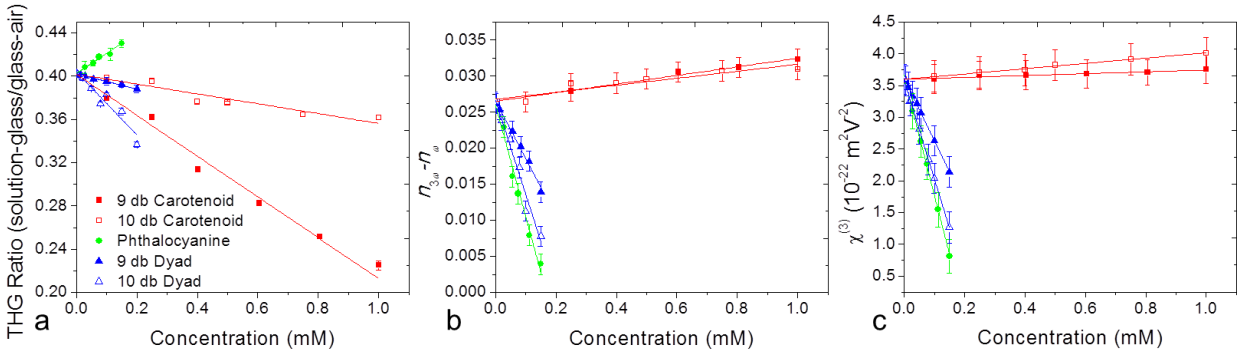

Figure 5.2.2: Determination of the third-order nonlinear optical susceptibility of carotenoids, phthalocyanine and their corresponding dyads in acetone. The THG intensity ratio dependence on concentration (a), the difference in refractive index ($n_{3\omega}$-n_{ω}) versus concentration (b), and the third-order nonlinear optical susceptibility ($\chi^{(3)}$) values versus concentration (c) were plotted.

Refractive index measurements of the solutions were made at the fundamental wavelength of the Yb:KGW laser, 1028 nm, and the third harmonic wavelength, 343 nm. The difference in refractive index, $n_{3\omega}$-n_{ω}, was plotted (Figure 5.2.2 (b)). The $n_{3\omega}$-n_{ω} of the carotenoids increases with increasing concentration similar to previous data measured for β-

carotene and xanthophylls. The $n_{3\omega}$-n_{ω} of the phthalocyanine model and the dyads decreases with increasing concentration similar to previous data measured for chlorophylls *a* and *b*.

From the THG intensity ratio and $n_{3\omega}$-n_{ω}, the third-order nonlinear optical susceptibility values were calculated (Figure 5.2.2 (c)). The $\chi^{(3)}$ values of the carotenoids increases with increasing concentration similar to previous data measured for β-carotene and xanthophylls while the $\chi^{(3)}$ values of the phthalocyanine model and the dyads decreases with increasing concentration.

The second hyperpolarizability values were extracted from the $\chi^{(3)}$ plots and they are shown in Table 5.2-1. The carotenoids have a positive γ value while the phthalocyanine model and the dyads both have large negative γ values.

Table 5.2-1: The γ values of a phthalocyanine, 9 double bonds and 10 double bonds carotenoid models, and the corresponding 9 double bonds and 10 double bonds dyad models.

Compound	γ (10^{-41} m^2V^{-2})
carotenoid (9 db) model	+0.9 ± 0.1
carotenoid (10 db) model	+2.7 ± 0.2
phthalocyanine model	-109 ± 23
dyad (9 db model)	-60 ± 9
dyad (10 db model)	-97 ± 13

The magnitude of the γ value of both the 9 db and the 10 db dyad is smaller than the magnitude of the phthalocyanine, indicating that γ is a combination of the γ values of the two separate molecules; a carotenoid and a phthalocyanine. There is a discrepancy within the dyads: the magnitude of the γ value for the 9 db dyad is smaller than the magnitude of the γ value for the 10 db dyad, which is surprising as one would expect the magnitude of the γ value of the 9 db dyad to be greater than the 10 db dyad as the magnitude of the γ value of the 9 db carotenoid is smaller and thus, would not contribute as much to the overall magnitude of the γ value of the 9 db dyad.

In Figure 5.2.3, it is observed that the absorbance band of the 10 db carotenoid and the 10 db dyad are spectrally shifted to the red as compared to the 9 db carotenoid and the 9 db dyad. As a result, the 10 db carotenoid and the 10 db dyad absorb more at the second harmonic wavelength (514 nm) of the Yb:KGW laser used for THG measurements than the 9 db carotenoid and 9 db dyad. The absorbance of the phthalocyanine was not plotted as no shift was

observed in comparison to the 9 db and 10 db dyads. Since the 10 db carotenoid absorbs more at the SHG wavelength, it is expected that the 10 db carotenoid would be more resonantly enhanced than the 9 db carotenoid. Similarly, the 10 db dyad is also expected to be more resonantly enhanced than the 9 db dyad. At the moment, it is unclear as to why the γ value of the 9 db dyad is more influenced by its carotenoid than the 10 db dyad. It is speculated that the contribution of the γ value from the carotenoid is increased, or from phthalocyanine is decreased due to molecular coupling. Further studies at different fundamental wavelengths are needed to gain more insight into this observation.

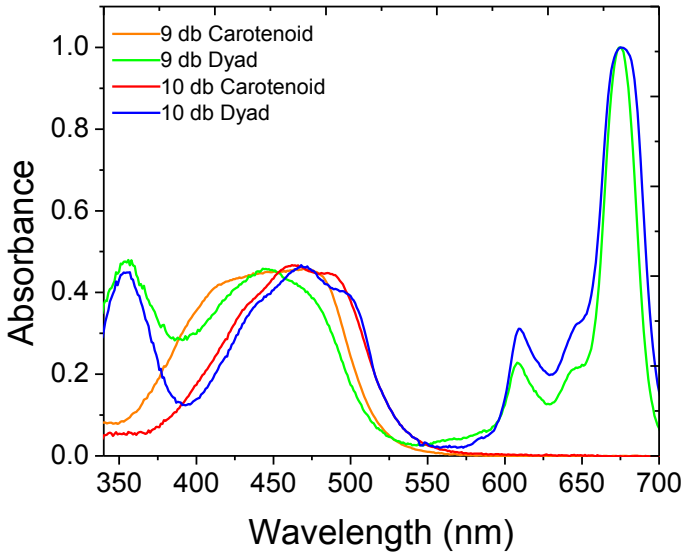

Figure 5.2.3: Absorption spectra in acetone for both the 9 db and10 db carotenoid and dyad models.

5.3 An Introduction to Photosynthetic Complexes

Although the earlier chapters highlighted carotenoids and chlorophylls independently, both carotenoids and chlorophylls are present in photosynthetic pigment-protein complexes and together they increase the light-harvesting efficiency in photosynthetic organisms. Carotenoids and chlorophylls are non-covalently bound to proteins located in photosynthetic membranes. Both carotenoids and chlorophylls serve specific roles where carotenoids function as light-harvesting pigments covering a region of the visible spectrum where chlorophylls have less absorption, they protect the photosynthetic apparatus against excessive light by quenching chlorophyll triplet states and lastly, carotenoids have a structural role in stabilizing the pigment-

protein complexes (Scheer 2003). The chlorophylls also serve as light-harvesting pigments and transfer excitation energy to reaction centers (Scheer 2003).

The difference in the sign of γ between carotenoids and chlorophylls at 1028 nm found in Chapter 4 indicates that if both carotenoids and chlorophylls are mixed at a certain concentration in solution, the THG generated from both molecules should experience cancellation. This was demonstrated in section 5.1 above. This is particularly interesting for nonlinear optical microscopy of photosynthetic organisms containing various types of pigment-protein complexes that serve as antennas for light-harvesting (Barzda 2008, Cisek, Spencer et al. 2009). For example, proteins within the Light-Harvesting Complex superfamily as well as the Peridinin-chlorophyll *a* protein contain both chlorophylls and carotenoids (Green, Anderson et al. 2003). Chlorosomes, as well as, bacterial light-harvesting antenna systems, light-harvesting complex 1 (LH1) and light-harvesting complex 2 (LH2), all contain bacteriochlorophyll and carotenoids while the Fenna-Matthews-Olson bacteriochlorophyll *a* protein of green sulfur bacteria contains bacteriochlorophyll only (Green, Anderson et al. 2003). From the results shown for the γ values of mixtures with chlorophylls and carotenoids, it is expected that the THG intensities from these pigment-protein complexes will vary depending on the pigment content and the interaction between the pigments. The proteins containing both (bacterio)chlorophylls and carotenoids may have reduced THG signal compared to the proteins containing only bacteriochlorophyll pigments.

In this section, the most abundant pigment-protein complex in chloroplasts, the light-harvesting chlorophyll *a*/*b* pigment-protein complex of photosystem II (LHCII) (Thornber 1975) was taken as a model system of a pigment-protein complex and the γ value of an LHCII trimer was measured by employing the THG ratio technique along with refractive index measurements. The obtained γ value of an LHCII trimer can serve as a reference when characterizing the THG intensity from other pigment-protein complexes. The comparison of the γ values from photosynthetic proteins, which contain different organizations of chlorophylls and carotenoids, can further provide information about the pigment interactions within the pigment-protein complexes.

5.4 LHCII Aggregates

5.4.1 LHCII

In green plants, solar energy is harvested by highly organized pigment-protein complexes such as LHCII in the thylakoid membranes of chloroplasts. LHCII is located at the periphery of the light-harvesting antenna of photosystem II and is involved in the regulation of the absorbed energy flow to the reaction center (van Grondelle, Monshouwer et al. 1996, van Amerongen and van Grondelle 2001, van Grondelle and Novoderezhkin 2006, Scholes, Fleming et al. 2011). X-ray crystallographic studies have shown that LHCII exists as a trimer in thylakoid membranes and contains eight chlorophyll *a*, six chlorophyll *b*, and four xanthophyll molecules (two lutein, one neoxanthin, and one other xanthophyll carotenoid) per monomer (Liu, Yan et al. 2004, Standfuss, van Scheltinga et al. 2005). In dark-adapted samples, the other xanthophyll is violaxanthin. However, under high light conditions, violaxanthin is converted into zeaxanthin through the xanthophyll cycle where the removal of the epoxide group on each β-ring is achieved by the enzyme, violaxanthin de-epoxidase (Telfer, Pascal et al. 2008). The reverse reaction is catalyzed by zeaxanthin epoxidase at a slower rate (Telfer, Pascal et al. 2008).

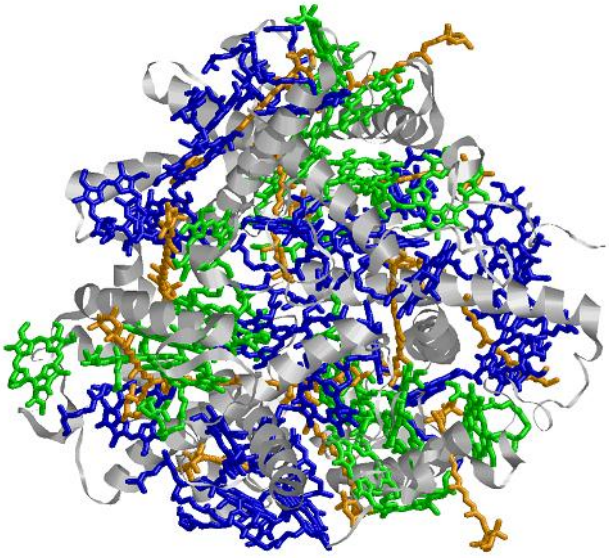

Figure 5.4.1: LHCII trimer crystallized from pea (*Pisum sativum*). Under most isolation conditions, LHCII is trimeric where each monomer consists of three membrane-spanning helices (gray) which are able to bind to chlorophylls (chlorophyll *a* is colored blue while chlorophyll *b* is colored green) and carotenoids (orange). The image was made in RasMol using the protein data bank file 2BHW provided by reference (Standfuss, van Scheltinga et al. 2005).

LHCII trimers aggregate to form disordered, highly ordered crystalline and multilamellar aggregates where the state of aggregation of LHCII can be controlled by the concentration of detergent and salts in a suspension containing LHCII (Barzda, Mustardy et al. 1994, Simidjiev, Barzda et al. 1997). Therefore, this provided us with an opportunity to study the efficiency of THG signal from LHCII aggregates, trimers and monomers. First, the nonlinear optical properties of LHCII aggregates were investigated with MPF, SHG and THG microscopy then, THG signals influenced by the aggregation state of LHCII was studied and lastly, the γ value of LHCII trimers was found and compared to the γ values of individual pigments.

5.4.2 Experimental Method

LHCII was isolated from leaves of two week old pea (*Pisum sativum*) plants as described by Simidjiev et al. (Simidjiev, Barzda et al. 1997). Briefly, isolated thylakoid membranes were solubilized with 0.8% of a 20% Triton X-100 solution buffered with 20 mM Tricine/NaOH at pH 7.8, and centrifuged at 30 000 g for 40 min to remove the insoluble pellet. LHCII was subsequently precipitated with 20 mM of $MgCl_2$ and 100 mM KCl, and purified by centrifugation of the LHCII suspension layered above a 0.5 M sucrose layer. The sediment of LHCII aggregates was resuspended with a concentration of 0.9 mg/ml chlorophyll *a* + *b* by Arnon (Arnon 1949) and then solubilized with 1.0% of a 10% Triton X-100 solution buffered with 15 mM Tricine/KOH at pH 7.8, and precipitated with 20 mM of $MgCl_2$ and 100 mM KCl, and purified by centrifugation of the LHCII suspension layered above a 0.5 M sucrose layer. Final purification was performed via further aggregation with 20 mM of $MgCl_2$ and 100 mM KCl, and purified by centrifugation of the LHCII suspension layered above a 100 mM sorbitol layer followed by repeated washing to obtain a chlorophyll *a*/*b* ratio between 1.1 and 1.2. The chlorophyll concentration was measured according to the method developed by Arnon (Arnon 1949). The UV-Vis spectral measurements were performed with an OLIS-14 upgraded Cary-14 spectrophotometer. Samples were stored at 4 °C in the dark and were used within one week after isolation.

In order to ensure that the suspension contained only trimers of LHCII, the LHCII aggregates with a concentration of 20 μg/ml chlorophyll *a* + *b* were solubilized with the critical micelle concentration of Triton X-100 which corresponded to 0.025% v/v and the aggregation

state was verified with circular dichroism (CD) spectroscopy (Aviv 215 circular dichroism spectrometer) (Barzda, Mustardy et al. 1994).

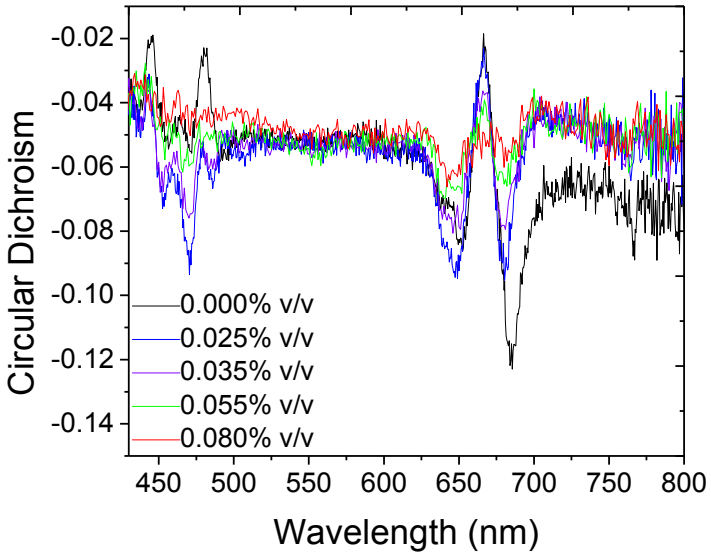

Figure 5.4.2: Circular dichroism spectra of LHCII with a concentration of 20 µg/ml chlorophyll *a* + *b* as a function of Triton X 100 concentration (% v/v).

5.4.3 Nonlinear Optical Microscopy of LHCII Aggregates

LHCII aggregates isolated from *Pisum sativum* leaves were investigated with multicontrast MPF, SHG, and THG microscopy (Figure 5.4.3).

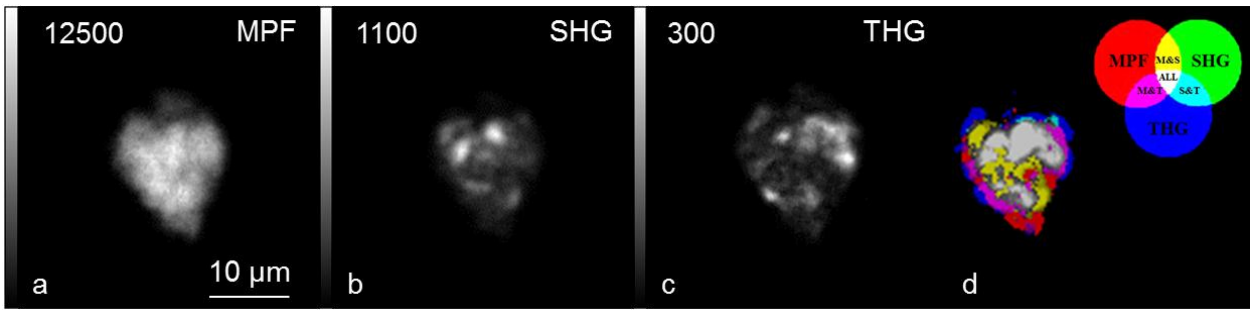

Figure 5.4.3: Nonlinear optical microscopy images of LHCII aggregates isolated from pea (*Pisum sativum*) leaves. LHCII aggregates are visualized by multiphoton excitation fluorescence (a), second harmonic generation (b) and third harmonic generation (c). The numbers in the upper left corner indicate the maximum photon counts in a pixel and the grey scale bar on the left side of the image ranges from 0 to the maximum signal intensity. A structural image cross-correlation analysis (Barzda 2008) between MPF, SHG and THG was performed and demonstrated in image (d). Figure reprinted with permission (Tokarz, Cisek et al. 2013).

Signals from the three contrast mechanisms highlight different features of the LHCII aggregate (Cisek, Spencer et al. 2009). The multiphoton fluorescence signal in the wavelength range 680-720 nm originates from the LHCII aggregates from two-photon excitation of chlorophylls and carotenoids in the pigment-protein complexes, as determined by the quadratic dependence of fluorescence signal on laser intensity.

The MPF image demonstrates a rather homogeneous distribution of LHCII (Figure 5.4.3 (a)), where the MPF signal intensity varies by 30% indicating very similar quenching properties as well as the density of the pigment-protein complexes in the aggregate. SHG signal from the LHCII aggregate (Figure 5.4.3 (b)) highlights domains with noncentrosymmetrically arranged xanthophylls and chlorophylls. LHCII aggregates are known to exhibit strong circular dichroism (Barzda 2008). In this preparation, CD (Figure 5.4.2) revealed that LHCII is likely to be found in 2D lamellar aggregates (Barzda, Mustardy et al. 1994). The pigment-protein complexes can aggregate into unilamellar stacks arranged in a unidirectional fashion, which would generate strong SHG signal. Figure 5.4.3 (b) shows that the SHG domains are embedded in a more centrosymmetrically arranged LHCII aggregate. Lastly, THG signal from the LHCII aggregate is attributed to the presence of xanthophylls and chlorophylls, which have high γ values. Unlike SHG, THG does not have organizational constraints and rather, THG signal requires structural heterogeneity occurring at interfaces where a change in refractive index and $\chi^{(3)}$ takes place. Multilamellar structures, such as stacks of thylakoid membranes can enhance THG signal (Barzda 2008, Cisek, Prent et al. 2009, Cisek, Spencer et al. 2009, Cisek 2012).

Correlation between MPF signal and SHG or THG signal of the LHCII aggregate yields evidence showing that harmonic signals are generated from the pigment-protein complexes. SHG and THG signals are mostly anticorrelated. Stronger SHG signal is seen in regions of weaker THG signal and weaker SHG signal is seen in regions of stronger THG. This observation has been previously described and explained by originating from the multilamellar structure of LHCII aggregates (Barzda 2008). The most intense SHG is observed in unidirectionally arranged stacks of membranes oriented parallel to the optical axes. At this orientation, the LHCII aggregates also show the largest chirality of the structure (Barzda 2008). Conversely, THG is most intense when the multilayer structure of LHCII is oriented perpendicular to the laser beam (Barzda 2008).

5.4.4 Aggregation Dependent THG Signals of LHCII

The third-order nonlinear optical properties of LHCII were further investigated by studying the THG intensity ratio of solution-glass to glass-air interfaces using the multicontrast nonlinear optical microscope. The THG ratios for LHCII at different aggregation states were obtained by varying the Triton X-100 concentration in the LHCII suspension (Figure 5.4.4). For an LHCII sample containing no detergent, the THG intensity ratio data were ignored when aggregates larger than the excitation focal volume occurred in the focus of the microscope objective. Therefore, the THG intensity at 0% Triton X-100 corresponds to smaller aggregates contained in the suspension.

In order to calculate the $\chi^{(3)}$ of the LHCII suspension, the refractive indices were measured at two wavelengths: the fundamental wavelength of the Yb:KGW laser, 1028 nm, and the third harmonic wavelength, 343 nm. Refractive index measurements of Triton X-100 in buffer at concentrations of interest did not significantly change from the refractive indices of the buffer, therefore the same refractive indices were assumed for the LHCII suspensions containing different detergent concentrations.

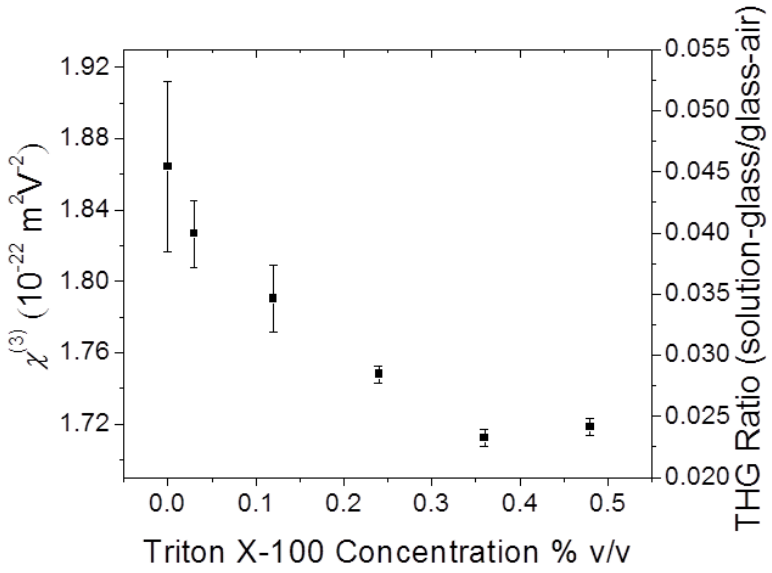

Figure 5.4.4: The third-order nonlinear optical susceptibility and the THG ratio intensity for an 80 μg/ml chlorophyll *a* + *b* solution of aggregated LHCII at various Triton X-100 concentrations. At 0.03 % v/v Triton X-100 concentration, LHCII exists in trimeric form and at 0.12 % v/v concentration, in monomeric form, as determined by CD spectroscopy (Hobe, Prytulla et al. 1994). Figure reprinted with permission (Tokarz, Cisek et al. 2013).

As the Triton X-100 concentration increases, the size of LHCII aggregates present in solution decreases and as a result, the THG intensity ratio and the $\chi^{(3)}$ of the aggregated LHCII suspension decreases. This indicates that larger LHCII aggregates show stronger THG signal. This is in agreement with previous research, which suggested that the enhancement of THG signal can be achieved with the aggregation of hematoxylin (Tuer, Tokarz et al. 2010).

At concentrations of Triton X-100 above the critical micelle concentration (0.03 % v/v) LHCII disaggregates into trimers, while LHCII monomers start to appear at higher Triton X-100 concentrations (Hobe, Prytulla et al. 1994). At concentrations above 0.36 % v/v, the release of some pigments from LHCII is likely to occur. The THG ratio increase observed above 0.36 % v/v of the detergent concentration is consistent with previously shown data in Chapter 4 of a larger THG ratio for chlorophylls in acetone (Tokarz, Cisek et al. 2012).

5.4.5 Determination of the γ value in Trimers of LHCII

The second hyperpolarizability of LHCII trimer complexes was obtained by studying the THG intensity ratio of the LHCII buffer solution-glass interface and the glass-air interface of a capillary tube found for a number of concentrations up to 100 μg/ml of chlorophylls *a* + *b* (Figure 5.4.5 (a)). At higher concentrations, LHCII was found to aggregate into larger structures.

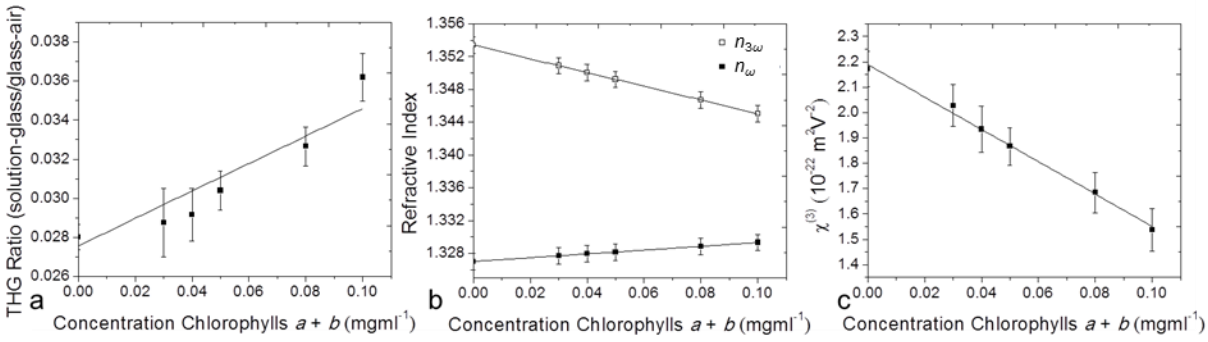

Figure 5.4.5: Determination of the second hyperpolarizability from the concentration dependent THG ratio and refractive index measurements of LHCII trimers in buffer solubilized with 0.025% v/v Triton X-100. The THG intensity ratio for LHCII versus concentration of chlorophylls *a* + *b* (a), the refractive indices of LHCII in buffer solution taken at 343 nm and 1028 nm (b), and the corresponding $\chi^{(3)}$ values versus concentration of chlorophylls *a* + *b* (c). Figure reprinted with permission (Tokarz, Cisek et al. 2013).

The THG intensity ratio increases with chlorophyll concentration, reminiscent of a similar dependence for chlorophyll *a* and chlorophyll *b* seen in Chapter 4. Previous THG

intensity ratio data of chlorophylls in acetone solvent also showed an increase in the THG intensity ratio with increasing concentration. The refractive indices of the trimeric LHCII suspensions were found at 1028 nm and 343 nm (Figure 5.4.5 (b)). LHCII does not absorb at 1028 nm however, it absorbs at 343 nm. The third harmonic wavelength is near LHCII absorption resonance and as a result, the refractive index of suspensions containing trimeric LHCII decreases with increasing concentration.

The $\chi^{(3)}$ plot of trimeric LHCII decreases with increasing chlorophyll *a* + *b* concentration (Figure 5.4.5 (c)). This suggests that the THG emitted from LHCII has the opposite phase with respect to the THG emitted from the buffer solution. This corresponds well with previous data that showed that the $\chi^{(3)}$ plots of chlorophylls *a* and *b* in acetone decrease with increasing concentration while the $\chi^{(3)}$ plots of xanthophylls in acetone increase with increasing concentration.

From the $\chi^{(3)}$ plot of trimeric LHCII, the γ value was extracted and found to be $(-1600 \pm 400)\times10^{-41}$ m^2V^{-2}. This value was compared to an estimated γ value for the LHCII trimer which consisted of the summation of individual xanthophylls and chlorophyll molecules. X-ray crystallographic studies of LHCII have concluded that a monomer of LHCII contains eight chlorophyll *a*, six chlorophyll *b*, and four xanthophyll molecules (two lutein, one neoxanthin, and one violaxanthin or zeaxanthin depending on light conditions) (Liu, Yan et al. 2004, Standfuss, van Scheltinga et al. 2005). Therefore, the estimated γ value for LHCII was obtained by the addition of individual γ values of pigments corresponding to an LHCII trimer. The estimated γ value for trimeric LHCII was found to be $(-3800 \pm 500)\times10^{-41}$ m^2V^{-2} which has an absolute value slightly larger than the experimentally measured γ value. In this estimation, the presence of polypeptide chains and lipids in the LHCII protein was ignored. The LHCII complex consists of three membrane-spanning helices and two short amphiphilic helices (Standfuss, van Scheltinga et al. 2005). The chlorophyll and xanthophyll molecules bind to the polypeptide chains as well as two different lipids, 1,2- dipalmitoylphosphatidylglycerol (DPPG) and digalactosyl diacyl glycerol (Standfuss, van Scheltinga et al. 2005). The γ values of the amino acids of the polypeptide chains in LHCII were not studied as they are not expected to contribute significantly to the overall γ value of LHCII. In order to validate this assumption, the summation of individual γ values for amino acids previously calculated using time-dependent Hartree-Fock calculations under physiological conditions (Tokarz, Tuer et al. 2010) were used to obtain the

overall γ value of the polypeptide chains in LHCII trimers as the amino acid sequences are known (Standfuss, van Scheltinga et al. 2005). The γ value for polypeptide chains in a LHCII trimer corresponds to 15.4×10^{-41} $m^2 V^{-2}$ and therefore it is negligible compared to the added γ value for all the chlorophylls in the LHCII trimer. Whereas for lipid, the γ value of DPPC measured in chloroform, which resembles DPPG, has a γ value of $(0.09 \pm 0.02)\times10^{-41}$ $m^2 V^{-2}$, which is larger than any of the individual amino acids calculated. However, the presence of six similar lipids (Standfuss, van Scheltinga et al. 2005) for each LHCII trimer does not contribute largely to the overall calculated γ value. Thus, the γ values of amino acids and lipids were not expected to contribute significantly to the overall γ value of LHCII.

Table 5.4-1: The γ value of LHCII measured by the THG ratio technique, individual γ values of carotenoids and chlorophylls found in LHCII, and the γ value of LHCII calculated from individual γ values of carotenoids and chlorophylls.

Harmonophore	γ (10^{-41} m^2V^{-2})
measured LHCII trimer	-1600 ± 400
estimated LHCII trimer	-3800 ± 500[a]
violaxanthin	+3.1 ± 0.6
neoxanthin	+8 ± 2
lutein	+1.4 ± 0.3
chlorophyll *a*	-100 ± 20
chlorophyll *b*	-80 ± 10

[a]The γ value of the LHCII trimer was estimated by the addition of individual γ values for 24 chlorophyll *a*, 18 chlorophyll *b*, 6 lutein, 3 neoxanthin and 3 violaxanthin molecules (Liu, Yan et al. 2004, Standfuss, van Scheltinga et al. 2005).

A difference between the experimentally measured and estimated γ values of the LHCII trimer is expected based on the variation in molecular environment and interaction between specifically oriented pigments in the pigment-protein complexes versus randomly oriented pigments in organic solvents. The γ values of xanthophylls and chlorophylls are measured in an acetone environment, while inside LHCII, the pigments experience a different dielectric environment of the protein. This change in environment leads to two effects, a slight change in the ground state wave function of the molecules, which influences the nonlinear properties, as well as, a shift in the index of refraction at the fundamental and third harmonic wavelength. The change in the environment has been exemplified by the alteration of the extinction coefficients, which has been shown to vary for chlorophyll *b* and xanthophylls in the LHCII protein and when present in acetone (Croce, Cinque et al. 2000). The excitonic interaction between chlorophyll and xanthophyll molecules is also expected to yield a deviation from the additive γ value. In fact the

nonlinear optical properties of pigment molecules are characterized by the second hyperpolarizability tensor, and therefore molecular interactions are very sensitive to the orientation of pigments in pigment-protein complexes. On the other hand, the LHCII second hyperpolarizability averages to an effective scalar value in the suspension. Therefore, the THG ratio technique measures the effective γ value of LHCII. In contrast, γ measurements of chlorophylls and xanthophylls in solution results in an overall orientationally averaged γ values for each pigment.

Second hyperpolarizability values can also be sensitive to solvent polarity where for instance, it has been mentioned in Chapter 3 that the γ values of carotenoids with donor-acceptor functional groups are largely affected by changes in solvent environment (Marder, Perry et al. 1993). However, the γ values for other carotenoids tends to be similar in various solvents and therefore, changes in solvent polarity are not expected to largely affect the γ values of the xanthophylls studied. Conversely, the solvent effects on the γ values of chlorophylls are not fully known. One study explored the changes in $\chi^{(3)}$ for the sulfonated zinc (II) 2,3-naphthalocyanine porphyrin (ZnNcS) in dimethyl sulfoxide (DMSO), dimethylformamide (DMF), and water (Fu, Yoda et al. 2005). Results showed that the $\chi^{(3)}$ for ZnNcS in DMSO was much higher than $\chi^{(3)}$ for ZnNcS in DMF and water however, γ values could not be obtained as ZnNcS aggregates in DMF and water (Fu, Yoda et al. 2005). The authors concluded that solvent polarity and aggregation influences $\chi^{(3)}$ (Fu, Yoda et al. 2005). Therefore, $\chi^{(3)}$ measurements of chlorophylls are sensitive to its environment and may contribute to overall differences observed between measured and calculated γ values for LHCII.

Overall, the $\chi^{(3)}$ values of LHCII trimers were achieved at a single wavelength. Therefore, if the absorption spectrum of LHCII shifts, the change in $\chi^{(3)}$ would be detected, but it is uncertain whether an overall change in the amplitude of $\chi^{(3)}$ occurs with various wavelengths. Future measurements should concentrate on studying the $\chi^{(3)}$ of LHCII at various wavelengths in order to understand the changes in $\chi^{(3)}$ values due to the harmonophores environment in pigment-protein complexes and due to the interactions between the pigments.

5.4.6 Conclusions

The γ value of the trimeric light-harvesting chlorophyll *a*/*b* pigment-protein complex of photosystem II isolated from pea (*Pisum sativum*) plants was investigated by the THG ratio

technique and found to be $(-1600 \pm 400)\times10^{-41}$ m^2V^{-2}. The γ value of LHCII at the fundamental wavelength of 1028 nm is negative and predominantly originates from the chlorophylls. The experimental γ value of LHCII trimers was found to be smaller than the estimated γ value from the corresponding stoichiometry summation of individual γ values of chlorophylls and xanthophylls in acetone. This difference is attributed to the differing molecular orientations of pigments in LHCII versus an isotropic solution as well as inter-pigment interactions which exist within LHCII. It was also shown that aggregation of LHCII leads to an increase in the $\chi^{(3)}$ values; the same effect observed for hematoxylin aggregates (Tuer, Tokarz et al. 2010).

5.5 Imaging of Carotenoids and Chlorophylls in Live Cells: *Haematococcus pluvialis*

The interaction between carotenoids and chlorophylls has been investigated in solution, as well as in covalently bonded dyads, and in pigment-protein complexes. In this section, knowledge of the nonlinear optical properties of carotenoids and chlorophylls are utilized in the investigation of nonlinear optical images of green algae. *Haematococcus pluvialis* is known to synthesize and accumulate astaxanthin when faced with unfavourable environmental conditions including: high or low light intensity, high salinity, higher temperatures and starvation. Under one or all of these conditions, it is believed that astaxanthin forms from β-carotene which is transported across the chloroplast membrane (Collins, Jones et al. 2011). Further, it has been speculated that astaxanthin accumulates in lipid vesicles outside the chloroplast (Santos and Mesquita 1984, Grunewald, Hirschberg et al. 2001, Collins, Jones et al. 2011). Little research has been done to spatially determine the location of astaxanthin in *Haematococcus pluvialis* during stress. As a result, nonlinear optical microscopy images of *Haematococcus pluvialis* were recorded in order to image the accumulation of astaxanthin in algae containing both chlorophylls and carotenoids and to investigate the accumulation processes of astaxanthin.

Haematococcus pluvialis was obtained from UTEX the Culture Collection of Algae (catalog number 2505) at the University of Texas at Austin and cultivated on MES-volvox medium. Cultures were exposed to 30 μmol $m^{-2}s^{-1}$ of cool-white fluorescent light all day and night. *Haematococcus pluvialis* were induced to accumulate astaxanthin by exposing to 5 μmol $m^{-2}s^{-1}$ of cool-white fluorescent light.

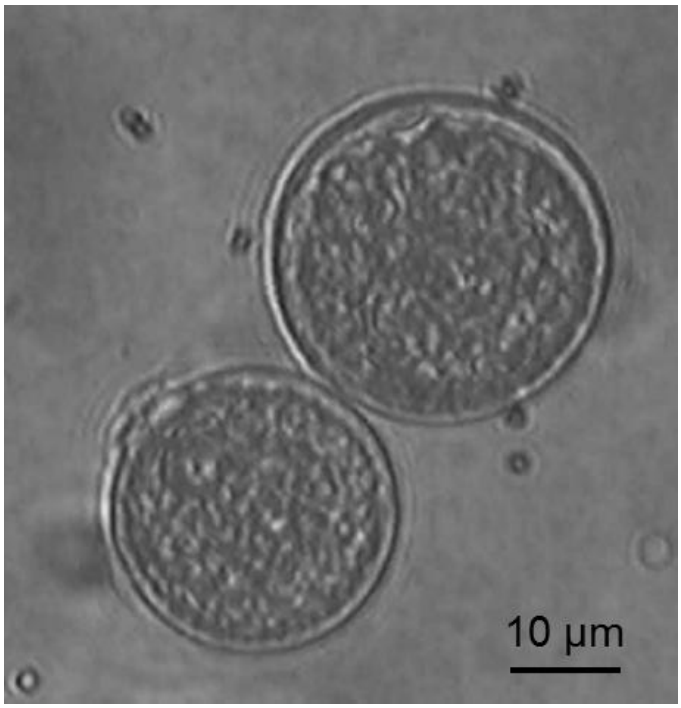

Figure 5.5.1: White light microscopy images of *Haematococcus pluvialis*. Green-colored palmella non-induced *Haematococcus pluvialis* cells.

Multiphoton excitation fluorescence is observed at the cell periphery due to fluorescence from chlorophyll present in chloroplasts. As the *Haematococcus pluvialis* turn red, the MPF signal decreases. Previous reports performed pigment quantification studies on algae extracts during the conversion of *Haematococcus pluvialis* from green flagellate cells into red aplanospores and found that the concentration of chlorophyll and β-carotene are constant throughout the conversion process (Tan, Cunningham et al. 1995, Collins, Jones et al. 2011). Therefore, the observed MPF signal decrease from green-colored palmella non-induced cells to red aplanospores seen in Figure 5.5.2 could be due to quenching of MPF signal or changes in the pigment-protein complex composition inside chloroplasts. A recent study found that the volume of chloroplasts decreases from 41.7% to 9.7% in *Haematococcus pluvialis* when changing from green-colored cells to red aplanospores (Wayama, Ota et al. 2013).

Second harmonic generation is observed from starch granules present in the algae. Starch granules in the SHG images are characterized by their double lobe structure which does not correlate with MPF or THG images (Cisek, Spencer et al. 2009). At the non-induced palmelloid stage, weak THG signal is observed. In red aplanospores, strong THG signal is observed at the periphery. Previous studies have reported high concentrations of astaxanthin at the edge of

aplanospores where astaxanthin is deposited into extra-plastidial oil bodies (Santos and Mesquita 1984, Boussiba 2000, Grunewald, Hirschberg et al. 2001, Wayama, Ota et al. 2013).The organizational structure of astaxanthin in extra-plastidial oil bodies was studied using PIPO SHG and PIPO THG. An example of PIPO SHG data and PIPO THG data corresponding to a red aplanospore is shown in Figure 5.5.3.

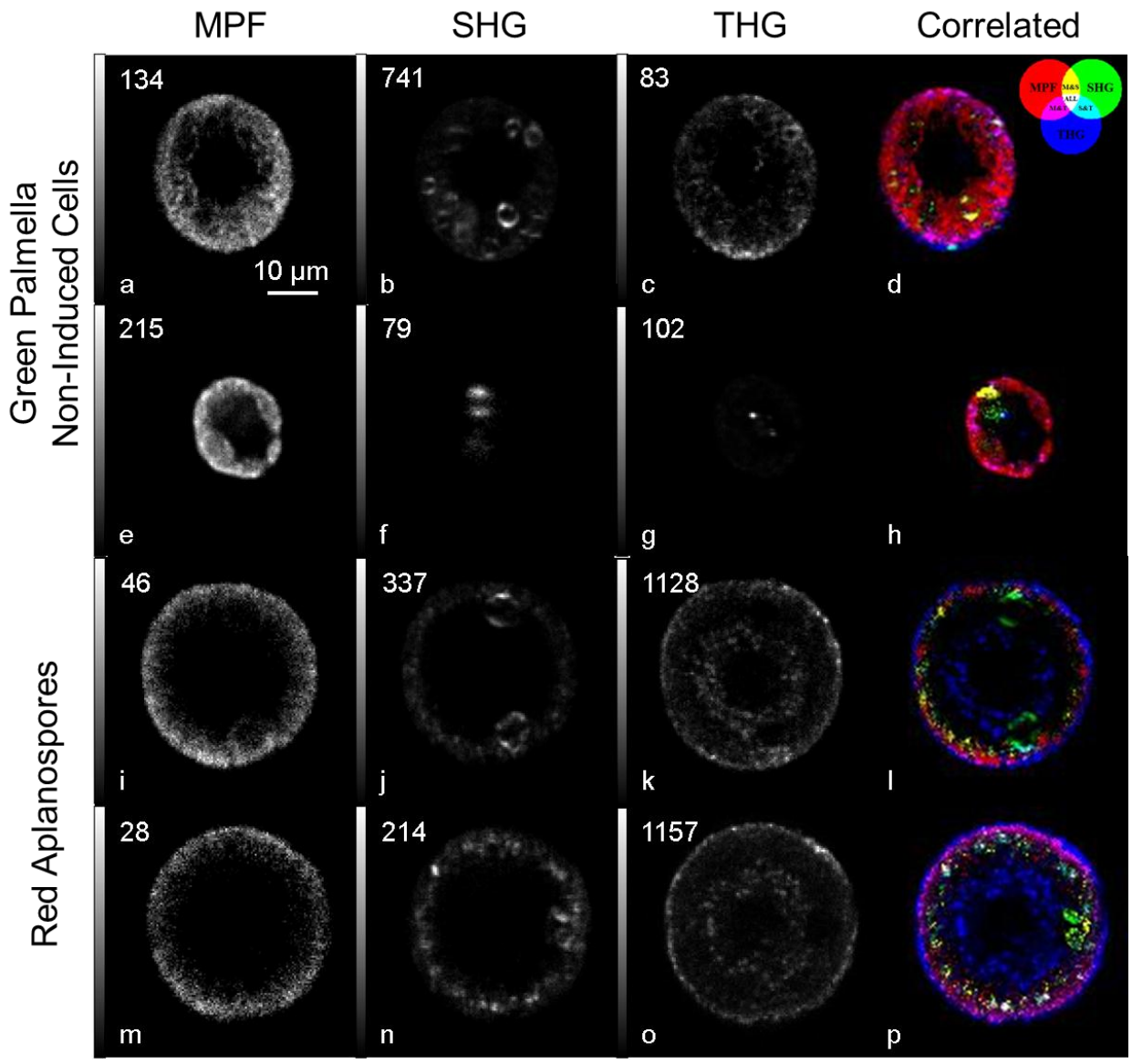

Figure 5.5.2: *Haematococcus pluvialis* imaged with MPF, SHG, and THG microscopy. The images (a) through (h) correspond to MPF, SHG, THG and correlated images, respectively, of a green-colored palmella non-induced cell while images (i) through (p) correspond to MPF, SHG, THG and correlated images, respectively, of red-colored aplanospores. The numbers in the upper left corner indicate the maximum photon counts in a pixel and the grey scale bar on the left side of the image ranges from zero to the maximum signal intensity.

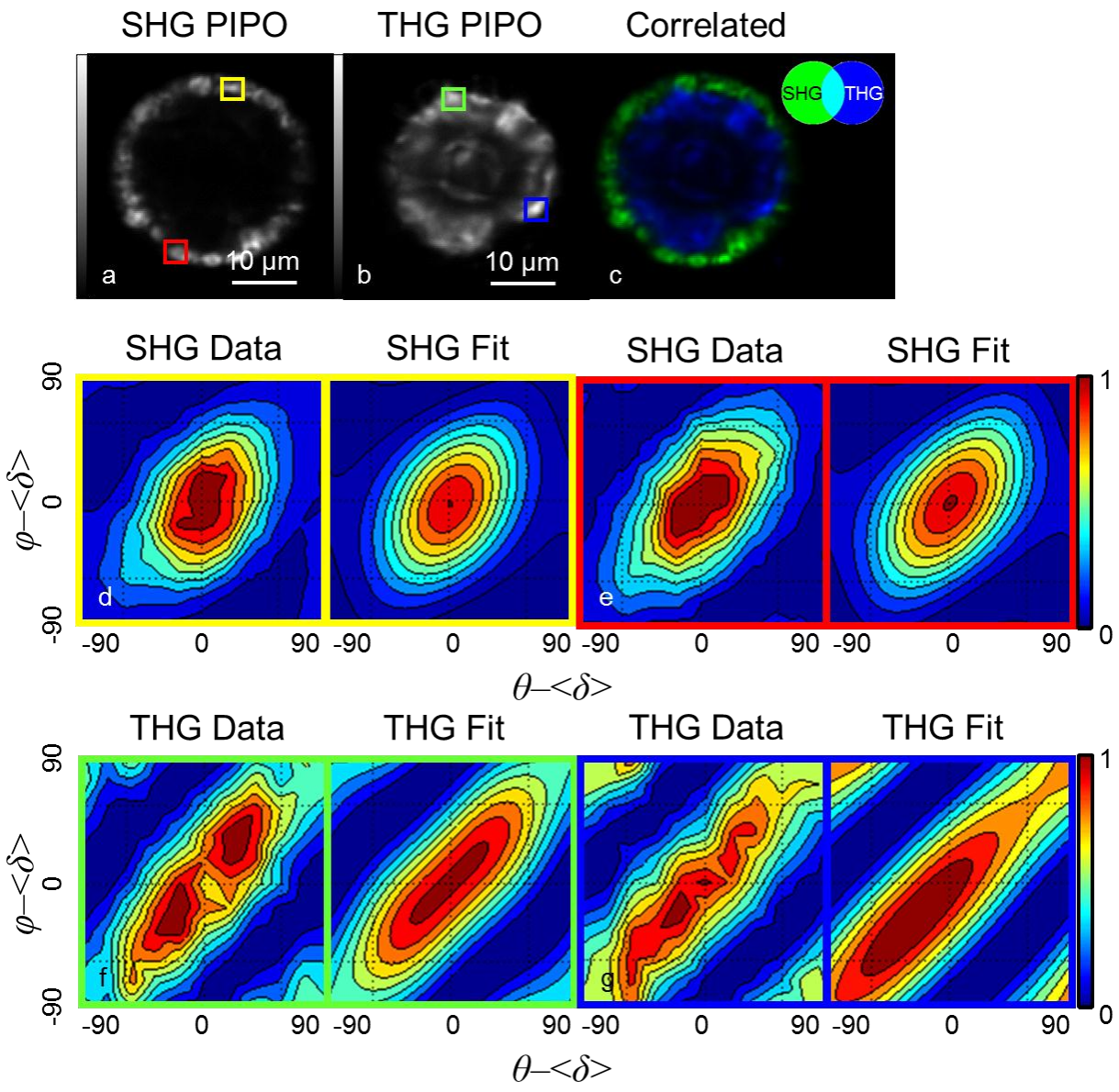

Figure 5.5.3: PIPO SHG and PIPO THG microscopy of a red aplanospore of *Haematococcus pluvialis*. The PIPO data (d, e, f, g) is shown as contour plots and represent polarization-dependent data gathered from regions of interest marked in SHG (a) and THG (b) images of a red aplanospore.

From Figure 5.5.3 (c), it is obvious that the SHG and THG signals generated from red aplanospores do not correlate. Fitting of the polarization-dependent SHG data revealed that the $\chi^{(2)}_{zzz}/\chi^{(2)}_{zxx}$ ratio for PIPO SHG data in Figure 5.5.3 (d, e) was 4.4 ± 1.0 (with a R-squared value of 0.965) and 3.6 ± 0.6 (with a R-squared value of 0.966), respectively. These ratio values are consistent with $\chi^{(2)}_{zzz}/\chi^{(2)}_{zxx}$ ratios measured for starch (Cisek 2012).

Fitting of PIPO THG data shown in Figure 5.5.3 (f, g) revealed that the $\chi^{(3)}_{zzzz}/\chi^{(3)}_{xxxx}$ ratio was 1.4 ± 0.4 (with a R-squared value of 0.915) and 1.2 ± 0.3 (with a R-squared value of 0.919), respectively, and the $\chi^{(3)}_{zzxx}/\chi^{(3)}_{xxxx}$ ratio was 0.5 ± 0.2 and 0.4 ± 0.1, respectively. The $\chi^{(3)}_{zzzz}/\chi^{(3)}_{xxxx}$ ratio for both regions is approximately 1 while the $\chi^{(3)}_{zzxx}/\chi^{(3)}_{xxxx}$ ratio for both regions is approximately 1/3. These ratios are consistent with the symmetry properties for an isotropic material: $\chi^{(3)}_{xxxx}=\chi^{(3)}_{zzzz}= \chi^{(3)}_{xxzz}+ \chi^{(3)}_{xzxz}+ \chi^{(3)}_{xzzx}$. Therefore, these ratios indicate that astaxanthin is distributed randomly in extra-plastidial oil bodies.

5.6 Summary and Outlook

Since chlorophylls and carotenoids were found to have γ values of opposite sign at 1028 nm, the THG intensity generated from a mixture containing chlorophyll *a* and β-carotene at a specific concentration was shown to cancel. However, when carotenoid and chlorophyll-like molecules are covalently bonded or excitonically interact, such as the examples seen with synthetic dyads and LHCII, additive effects with the γ values of the carotenoids and chlorophylls still occur, but in addition to this, the overall γ value is influenced by the intra- and inter-pigment interaction. Further elucidation of the interaction between chlorophylls and carotenoids can be achieved by measuring their nonlinear optical properties at different wavelengths. The interaction between chlorophylls and carotenoids in a number of pigment-protein complexes can be studied and compared. Additionally, understanding the inter-pigment interactions between carotenoids and chlorophylls will help in designing more efficient harmonophores.

Although both chlorophylls and carotenoids generate THG and THG intensity is influenced by the interaction between both pigments, specific studies such as the localization of the accumulation of a carotenoid in an algae such as *Haematococcus pluvialis* may be performed as long as additional nonlinear optical techniques are also available including MPF in order to detect chlorophyll fluorescence and SHG to detect other crystalline structures such as starch. In the following chapter, labeling studies with carotenoid harmonophores will be explored.

Chapter 6
Harmonophore Labeling of Biological Structures[5]

6.1 Labeling Experiments with Carotenoid Harmonophores

6.1.1 Muscle Labeled with Carotenoids

Fish including salmon and trout are able to retain excess carotenoids not needed for maintaining life functions in their muscle tissue, which results in a pink or red colored flesh. In nature, salmon and trout achieve this coloration by eating algae and crustaceans containing astaxanthin and canthaxanthin. Salmon raised in captivity are fed with synthetic astaxanthin in order to achieve coloration. Many speculations exist as to how astaxanthin binds to salmon muscle however, recent studies have shown that α-actinin is the only myofibrillar protein that binds significantly to astaxanthin with weak hydrophobic forces (Matthews, Ross et al. 2006, Bjerkeng 2008). Inspired by nature, *Drosophila melanogaster* larvae were fed with medium enriched with β-carotene to study the labeling of larvae myocytes.

The *Drosophila melanogaster* larvae were raised on Bloomington medium at 25 °C. Two stocks of the larvae were raised in parallel. One contained 30 mg/ml of β-carotene in the Bloomington medium, and the other stock was treated as a control without β-carotene. Treated *Drosophila melanogaster* larvae with β-carotene developed normally in comparison with the control. Second instar larvae were selected and dissected by cutting the larvae lengthwise, removing the internal organs, and unfolding the muscle tissue to lie flat. The prepared larvae were immersed in phosphate buffered saline to prolong viability.

Second harmonic generation and third harmonic generation images of *Drosophila melanogaster* larvae myocytes were recorded simultaneously. In Figure 6.1.1 (a, c), SHG images of unlabeled and labeled *Drosophila melanogaster* larvae myocytes are presented. The 830 nm

[5]Parts of the following chapter were adapted from a published paper. Reprinted (adapted) with permission from Tokarz, D., Cisek, R., Garbaczewska, M., Sandkuijl, D., Qiu, X., Stewart, B., Levine, J.D., Fekl, U., and Barzda, V. (2012) "Carotenoid Based Bio-Compatible Labels for Third Harmonic Generation Microscopy," Physical Chemistry Chemical Physics, **14** (30) 10653. Copyright Royal Society of Chemistry 2012. The specific contributions made by all authors are presented in the Statement of Contributions section on page 142.

excitation wavelength was chosen for this study as the γ value of β-carotene is higher at this wavelength than at 1028 nm excitation.

The use of SHG microscopy highlights the anisotropic bands of myocytes, which contain myosin filaments. The isotropic bands, containing actin, do not generate appreciable SHG. No difference in SHG intensity between unlabeled and labeled myocytes is observed. However, the THG intensity of labeled myocytes was over 100 times brighter than unlabeled myocytes where the entire heterogeneous tissue generates THG. In the control sample, THG seems to be generated only by blood cells. The labeled tissue is 5 times brighter than blood cells. It has been shown previously that THG originates from unlabeled blood vessels and blood cells in muscle tissue at 1275 nm excitation (Rehberg, Krombach et al. 2011). Therefore, β-carotene is retained in the muscle of *Drosophila melanogaster* larvae and β-carotene labeled muscle can be imaged with THG microscopy.

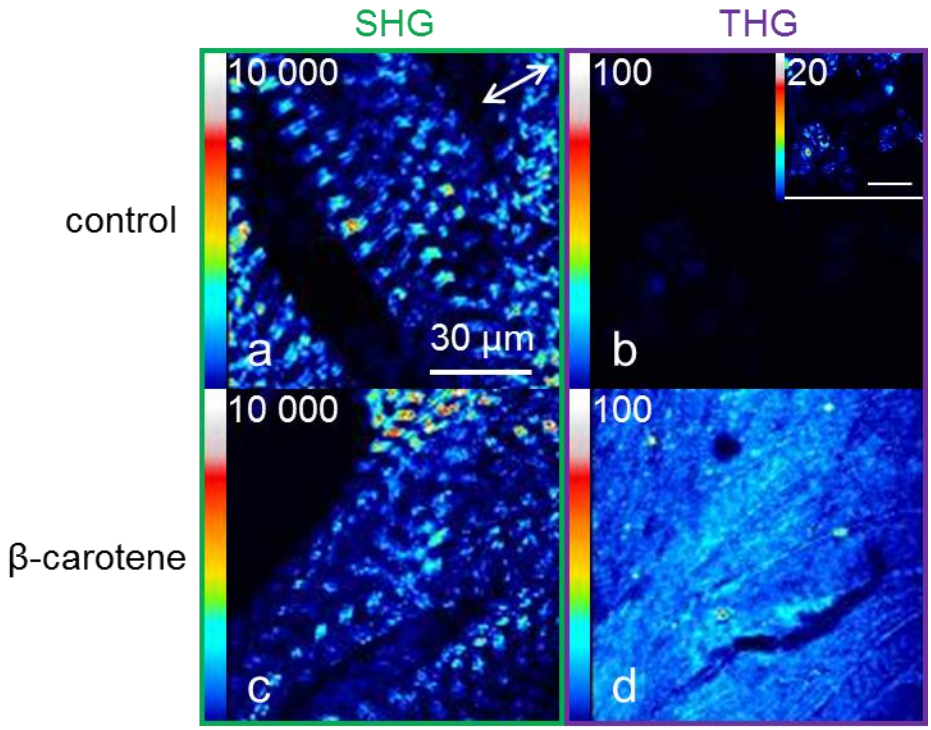

Figure 6.1.1: *Drosophila melanogaster* larvae muscle imaged with 830 nm excitation. SHG microscopy images (a, c) as well as THG microscopy images (b, d) of control unlabeled muscle (a, b) and β-carotene labeled muscle (c, d). The laser excitation polarization is demonstrated at the top right-hand corner of image (a). Figure reprinted with permission (Tokarz, Cisek, et al. 2012).

For more specific labeling of biological structures, carotenoids can be chemically modified. Recent carotenoid synthesis has focused on developing hydrophilic carotenoids which include carotenoid salts, carotenoid cyclodextrin complexes, carotenoid glycosides, carotenoid with hydroxybenzene rings and carotenoid polyethyleneglycol conjugates (Hada 2012). Unfortunately, many well-known reactions do not proceed with carotenoids and low yields of synthetic carotenoids are often achieved (Sliwka, Partali et al. 2009). Therefore, further investigation would be needed to determine cost-effective synthetic strategies of newly synthesized carotenoid-based harmonophores.

6.1.2 Hair Labeled with Carotenoids

In nature, carotenoids bind to structural proteins such as α-actinin, a muscle protein described in section 6.1.1. In addition to this, carotenoids also bind to the structural proteins of bird feathers. Specifically, carotenoids are present in the follicles of feathers. As the feathers develop, carotenoids become strongly bound to β-keratin protein filaments (Stradi, Celentano et al. 1995, Britton and Helliwell 2008, Mendes-Pinto, LaFountain et al. 2012). At the moment, it is unclear whether carotenoids in feathers bind directly to β-keratin or another protein present in bird feathers (Mendes-Pinto, LaFountain et al. 2012).

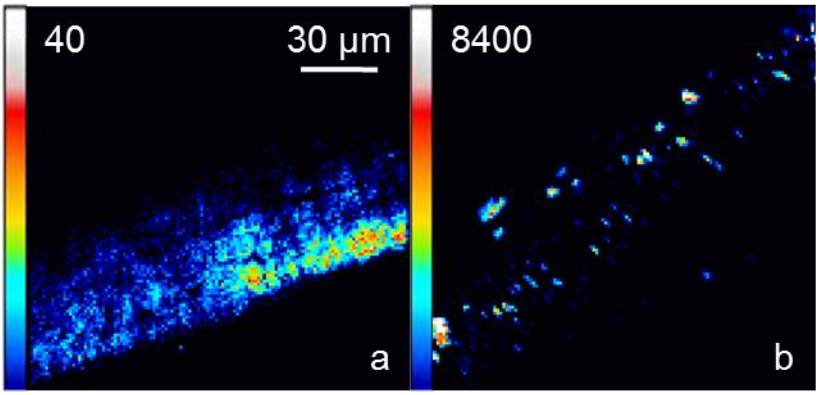

Figure 6.1.2: THG images of blonde human hair submerged in ethanol and a solution containing β-carotene. THG images of blonde hair immersed in ethanol for 15 min (a) and blonde hair immersed in a solution of 0.1 mM β-carotene dissolved in ethanol (b).

Inspired by the coloration of bird feathers, a second labeling experiment was attempted which involved immersing human hair, which is known to contain α-keratin, in a 0.1 mM solution of β-carotene dissolved in ethanol for 15 min. The human hair was then air-dried and imaged with THG microscopy. A second piece of human hair was placed in ethanol for 15 min.

This second piece of hair served as a control. THG images of the control and labeled hair is shown in Figure 6.1.2.

Human hair that was immersed in β-carotene solution gave rise to 210 times more THG signal than the control. Therefore, it is speculated that β-carotene binds to α-keratin or another protein contained within hair. Furthermore, the THG signal seen in Figure 6.1.2 (b) is not heterogeneous and occurs in specific areas of the hair which could be due to the aggregation of β-carotene. Similarly, it has been speculated that canthaxanthin J-aggregates form in the β-keratin protein fibers of feathers belonging to the *I. isabellae* species (Mendes-Pinto, LaFountain et al. 2012).

6.1.3 Cells Labeled with Carotenoid Liposomes

The two labeling experiments earlier demonstrated non-specific labeling however, in order to achieve a more selective type of labeling, experiments with carotenoid liposomes were performed. *Drosophila* Schneider 2 (S2) cells were studied after incubation with β-carotene incorporated liposomes resulting in the natural process of liposome fusion. Previous researchers have used liposome fusion as a drug delivery technique and for cell-surface engineering where complimentary functionalized cell surfaces with liposomes can chemically react (Dutta, Pulsipher et al. 2011). This fusion technique is also a convenient method to introduce β-carotene harmonophores into cells.

Cell imaging of liposome fusion studies was performed with 1-palmitoyl-2-oleoyl-*sn*-glycero-3-phosphocholine (POPC) (Avanti Polar Lipids, Inc., 99%) liposomes incorporated with 0.25 μmol of β-carotene at 1028 nm excitation. POPC lipids linearly absorb at the third harmonic wavelengths of 773 nm and 830 nm, therefore the Yb:KGW was used to reveal clearly the labeling effect of carotenoids. β-carotene was chosen for labeling experiments since it is the most widely studied and cost effective carotenoid.

Figure 6.1.3 shows the THG enhancement of S2 cells incubated with β-carotene incorporated POPC liposomes. S2 cells (Figure 6.1.3 (a, b, c)) and S2 cells incubated with POPC liposomes (Figure 6.1.3 (d, e, f)) typically give rise to THG from intracellular organelles and internalized lipid membranes. However, the cells labeled with β-carotene liposomes (Figure 6.1.3 (g, h, i)) increase THG signal by 12 times for the presented case. Further, the β-carotene

harmonophores reveal the cell membrane and internalized liposomes demonstrating that harmonophores can be successfully used for labeling biological structures in THG microscopy.

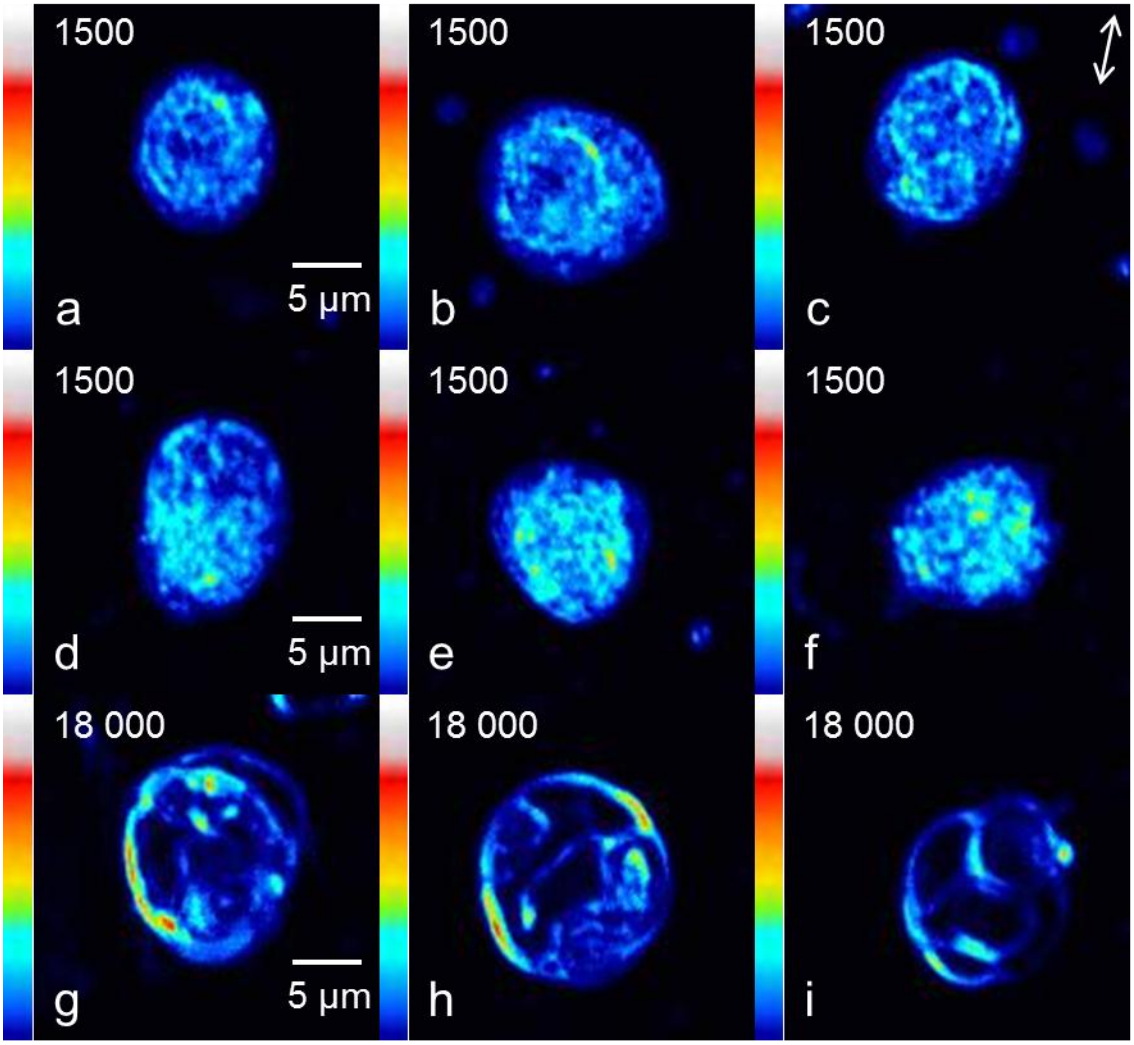

Figure 6.1.3: *Drosophila* Schneider 2 cells imaged with THG microscopy. THG images of untreated S2 cells (a, b, c), S2 cells incubated with POPC liposomes for 3 hours (d, e, f) and S2 cells incubated with β-carotene incorporated POPC liposomes for 3 hours (g, h, i). The THG images were recorded with 1028 nm laser radiation. The laser excitation polarization is shown at the top right-hand corner of image (c). Figure reprinted with permission (Tokarz, Cisek, et al. 2012).

6.2 Summary and Outlook

This chapter demonstrates that bio-compatible labels based on carotenoids can be used for cell labeling in third harmonic generation microscopy. Since carotenoids naturally occur in plants, algae and marine animals, they are biologically compatible and can also be used as labels for *in vivo* THG microscopy. Specifically, it has been shown that carotenoid liposomes can be

used for targeted labeling of cellular membranes as demonstrated by S2 cell fusion with β-carotene incorporated liposomes. Non-selective labeling of *Drosophila melanogaster* larvae myocytes with β-carotene was demonstrated where the THG intensity of the tissue was over 100 times greater than the THG of unlabeled muscle. Overall, THG enhancement by natural carotenoids can serve as the basis for the development of nontoxic labels of biological structures for *in vivo* imaging applications using third harmonic generation microscopy.

Chapter 7
Conclusions

Harmonic generation microscopy is highly valued for noninvasive biological structure imaging however, this technique is not always highly specific to particular biomolecules. In order to achieve specificity in harmonic generation microscopy, molecular labels can be used. Therefore, harmonophores present a promising avenue for labeling in harmonic generation microscopy. Consequently, the nonlinear optical properties of harmonophores were investigated in this work. First, a technique to measure the third-order nonlinear optical susceptibilities of solutions was implemented referred to as the THG ratio technique. Since $\chi^{(3)}$ values are sensitive to the difference in refractive index at the fundamental and third harmonic wavelength, the development of a refractometer was necessary in order to accurately determine $\chi^{(3)}$ values. For solutions that do not absorb at the third harmonic and fundamental wavelengths, the refractive index of the solvent can be used to find the $\chi^{(3)}$ of the solution. However, this assumption is no longer valid when the harmonophore solutions absorb at either the fundamental or third harmonic wavelength. Therefore, in order to determine accurate $\chi^{(3)}$ and γ values of such compounds, measurement of the refractive index was essential.

The third-order nonlinear optical properties of a number of carotenoids and chlorophylls were explored. The $\chi^{(3)}$ plots of carotenoids and chlorophylls dissolved in acetone as a function of concentration at 830 nm demonstrated that the THG emitted from carotenoids and chlorophylls versus acetone are opposite in phase and therefore, both carotenoids and chlorophylls possess negative γ values at this wavelength. However, at 1028 nm, the THG emitted from carotenoids is in phase with the THG generated from acetone while the THG generated from chlorophylls is still out of phase. Therefore, at 1028 nm, carotenoids have a positive γ value and chlorophylls have a negative γ value. Further, it was experimentally shown that at a specific concentration of carotenoids and chlorophylls dissolved in acetone, the THG generated from carotenoids canceled with the THG generated from chlorophylls at 1028 nm.

In nature, carotenoids and chlorophylls are often found together where for example, in plants, they both play a role in harvesting solar energy. The third-order nonlinear optical properties as a result of the interaction between carotenoids and chlorophylls were studied by a number of ways including synthetic dyads of carotenoid and chlorophyll-like molecules and

LHCII trimers. Third-order nonlinear optical susceptibility measurements were performed at 1028 nm in order to investigate how the overall γ value of the entire complex is influenced by carotenoids with positive γ values and chlorophylls with negative γ values. Both the dyads and the LHCII trimers were found to have γ values that were negative however, the γ value was influenced by a larger contribution from the carotenoids than expected. Therefore, it was found that additive effects with the γ values of the carotenoids and chlorophylls still play a role however, in addition to this, the overall γ value is also influenced by the intra- and inter-pigment interaction. In order to better understand the influence of interactions amongst carotenoids and chlorophylls on the γ value, future investigations of both the dyads and LHCII should be performed with a tunable laser in order to achieve γ measurements at several wavelengths and compared with the γ values of carotenoids and chlorophylls also performed at several wavelengths.

Studies of $\chi^{(3)}$ are performed in solution where harmonophores are presumed to have an isotropic orientation however, many instances in nature exist where harmonophores are present as crystalline aggregates. Therefore, polarization-dependent SHG and THG microscopy was used in order to reveal structural details about carotenoid aggregates. In particular, natural carotenoid aggregates including β-carotene crystalline aggregates found in orange carrot as well as H and J aggregates were studied. PIPO SHG and PIPO THG studies revealed that β-carotene molecules in crystalline aggregates in orange carrots and astaxanthin molecules in H and J aggregates have nonlinear dipoles very well aligned along a cylindrical axis. Since it has been suggested in literature that carotenoids are more easily absorbed by humans when chromoplasts adopt round structures versus crystalline aggregates, future investigations could focus on studying carotenoid crystalline morphology in different fruits and vegetables *in vivo* by PIPO SHG and PIPO THG microscopy. Further, the organization of more complex aggregates consisting of both carotenoids and chlorophylls such as LHCII could be studied by PIPO SHG and PIPO THG microscopy.

In addition to carotenoids and chlorophylls possessing large values of second hyperpolarizabilities, both types of pigments have the additional benefit that they are non-toxic and can be favorably used for health benefits. Thus, carotenoids and chlorophylls are attractive labels for *in vivo* imaging applications. Examples of labeling with carotenoids included incorporating carotenoids in liposomes and performing cell fusion experiments with *Drosophila* Schneider 2 cells. This experiment demonstrated that carotenoid liposomes can be used to label

cellular membranes. Also, non-selective labeling of *Drosophila melanogaster* larvae myocytes with β-carotene was achieved where the THG intensity of the tissue was over 100 times greater than the THG of unlabeled muscle. Although labeling experiments were solely performed with β-carotene, it is expected that labeling experiments performed with chlorophyll would further enhance the THG signal as the magnitude of its γ value is much larger than the γ value of several carotenoids at both 830 nm and 1028 nm wavelengths.

Overall, THG enhancement by natural carotenoids as well as chlorophylls can serve as the basis for the development of nontoxic labels of biological structures for *in vivo* imaging applications using third harmonic generation microscopy.

References

Abbe, E. (1873). "Beitrage zur Theorie des Mikroskops und der mikroskopischen Wahrnehmung." Schultzes Archiv fur Mikroskopische Anatomie **9**: 413-468.

Arnon, D. I. (1949). "Copper enzymes in isolated chloroplasts. Polyphenoloxidase in *Beta vulgaris*." Plant Physiology **24**(1): 1-15.

Baconnier, S. and S. B. Lang (2004). "Calcite microcrystals in the pineal gland of the human brain: Second harmonic generators and possible piezoelectric transducers." Ieee Transactions on Dielectrics and Electrical Insulation **11**(2): 203-209.

Barad, Y., H. Eisenberg, M. Horowitz and Y. Silberberg (1997). "Nonlinear scanning laser microscopy by third harmonic generation." Applied Physics Letters **70**(8): 922-924.

Barille, R., L. Canioni, S. Rivet, L. Sarger, P. Vacher and T. Ducret (2001). "Visualization of intracellular Ca^{2+} dynamics with simultaneous two-photon-excited fluorescence and third-harmonic generation microscopes." Applied Physics Letters **79**(24): 4045-4047.

Barille, R., L. Canioni, L. Sarger and G. Rivoire (2002). "Nonlinearity measurements of thin films by third-harmonic-generation microscopy." Physical Review E **66**(6): 0676021-0676024.

Barsu, C., R. Cheaib, S. Chambert, Y. Queneau, O. Maury, D. Cottet, H. Wege, J. Douady, Y. Bretonniere and C. Andraud (2010). "Neutral push-pull chromophores for nonlinear optical imaging of cell membranes." Organic & Biomolecular Chemistry **8**(1): 142-150.

Barsu, C., R. Fortrie, K. Nowika, P. L. Baldeck, J. C. Vial, A. Barsella, A. Fort, M. Hissler, Y. Bretonniere, O. Maury and C. Andraud (2006). "Synthesis of chromophores combining second harmonic generation and two photon induced fluorescence properties." Chemical Communications(2006): 4744-4746.

Bartalucci, G., J. Coppin, S. Fisher, G. Hall, J. R. Helliwell, M. Helliwell and S. Liaaen-Jensen (2007). "Unravelling the chemical basis of the bathochromic shift in the lobster carapace; new crystal structures of unbound astaxanthin, canthaxanthin and zeaxanthin." Acta Crystallographica Section B-Structural Science **63**: 328-337.

Bartalucci, G., C. Delroy, S. Fisher, M. Helliwell and S. Liaaen-Jensen (2008). "13-cis-beta,beta-carotene and 15-cis-beta,beta-carotene." Acta Crystallographica Section C-Crystal Structure Communications **64**: O128-O131.

Barzda, V. (2008). Non-linear contrast mechanisms for optical microscopy. Biophysical Techniques in Photosynthesis. T. J. Aartsma and J. Matysik. Dordrecht, Springer. **2:** 35-54.

Barzda, V., C. Greenhalgh, J. Aus der Au, S. Elmore, J. van Beek and J. Squier (2005). "Visualization of mitochondria in cardiomyocytes by simultaneous harmonic generation and fluorescence microscopy." Optics Express **13**(20): 8263-8276.

Barzda, V., L. Mustardy and G. Garab (1994). "Size dependency of circular-dichroism in macroaggregates of photosynthetic pigment-protein complexes." Biochemistry **33**(35): 10837-10841.

Belisle, J. M., S. Costantino, M. L. Leimanis, M. J. Bellemare, D. S. Bohle, E. Georges and P. W. Wiseman (2008). "Sensitive detection of malaria infection by third harmonic generation imaging." Biophysical Journal **94**(4): L26-L28.

Beljonne, D., J. Cornil, Z. Shuai, J. L. Brédas, F. Rohlfing, D. D. C. Bradley, W. E. Torruellas, V. Ricci and G. I. Stegeman (1997). "General model for the description of the third-order optical nonlinearities in conjugated systems: Application to the all-*trans* β-carotene molecule." Physical Review B **55**(3): 1505-1516.

Berera, R., C. Herrero, I. H. M. van Stokkum, M. Vengris, G. Kodis, R. E. Palacios, H. van Amerongen, R. van Grondelle, D. Gust, T. A. Moore, A. L. Moore and J. T. M. Kennis (2006). "A simple artificial light-harvesting dyad as a model for excess energy dissipation in oxygenic photosynthesis." Proceedings of the National Academy of Sciences of the United States of America **103**(14): 5343-5348.

Bjerkeng, B. (2008). Carotenoids in aquaculture: Fish and crustaceans. Carotenoids. G. Britton, S. Liaaen-Jensen and H. Pfander. Boston, Birkhäuser. **4:** 237-254.

Bondarev, S. L. and V. N. Knyukshto (1994). "Fluorescence from the S_1 (2^1A_g) state of all-trans-beta-carotene." Chemical Physics Letters **225**(4-6): 346-350.

Bosshard, C., U. Gubler, P. Kaatz, W. Mazerant and U. Meier (2000). "Non-phase-matched optical third-harmonic generation in noncentrosymmetric media: Cascaded second-order contributions for the calibration of third-order nonlinearities." Physical Review B **61**(16): 10688-10701.

Boussiba, S. (2000). "Carotenogenesis in the green alga *Haematococcus pluvialis*: Cellular physiology and stress response." Physiologia Plantarum **108**(2): 111-117.

Boyd, R. W. (2008). Nonlinear Optics. Amsterdam, Academic Press.

Brackmann, C., A. Bengtsson, M. L. Alminger, U. Svanbergb and A. Enejdera (2011). "Visualization of β-carotene and starch granules in plant cells using CARS and SHG microscopy." Journal of Raman Spectroscopy **42**: 586-592.

Britton, G. and J. R. Helliwell (2008). Carotenoid-protein interactions. Carotenoids. G. Britton, S. Liaaen-Jensen and H. Pfander. Boston, Birkhäuser. **4:** 99-118.

Brown, E., T. McKee, E. diTomaso, A. Pluen, B. Seed, Y. Boucher and R. K. Jain (2003). "Dynamic imaging of collagen and its modulation in tumors in vivo using second-harmonic generation." Nature Medicine **9**(6): 796-800.

Bryant, J. D., J. D. Mccord, L. K. Unlu and J. W. Erdman (1992). "Isolation and partial characterization of alpha-carotene-containing and beta-carotene-containing carotenoprotein from

carrot (Daucus-carota L) root chromoplasts." Journal of Agricultural and Food Chemistry **40**(4): 545-549.

Cervantes, M. M., F. M. Barboza and M. Inoue (1991). "Self-focusing in new kerr media: Large thermal nonlinearity in metallotetraphenylporphins." Journal of Russian Laser Research **12**(5): 447-451.

Chang, C. F., C. Y. Chen, F. H. Chang, S. P. Tai, C. Y. Chen, C. H. Yu, Y. B. Tseng, T. H. Tsai, I. S. Liu, W. F. Su and C. K. Sun (2008). "Cell tracking and detection of molecular expression in live cells using lipid-enclosed CdSe quantum dots as contrast agents for epi-third harmonic generation microscopy." Optics Express **16**(13): 9534-9548.

Chen, L. X. Q. (1993). "Nonlinear-optical properties of porphyrin and chlorophyll dimers studied by degenerated four-wave mixing." Proceedings of SPIE **1852**(Nonlinear Optical Properties of Advanced Materials): 162-166.

Chen, X. Y., O. Nadiarynkh, S. Plotnikov and P. J. Campagnola (2012). "Second harmonic generation microscopy for quantitative analysis of collagen fibrillar structure." Nature Protocols **7**(4): 654-669.

Chou, C. K., W. L. Chen, P. T. Fwu, S. J. Lin, H. S. Lee and C. Y. Dong (2008). "Polarization ellipticity compensation in polarization second-harmonic generation microscopy without specimen rotation." Journal of Biomedical Optics **13**(1): 0140051-0140057.

Chu, S. W., I. H. Chen, T. M. Liu, P. C. Chen, C. K. Sun and B. L. Lin (2001). "Multimodal nonlinear spectral microscopy based on a femtosecond Cr:forsterite laser." Optics Letters **26**(23): 1909-1911.

Chu, S. W., S. Y. Chen, G. W. Chern, T. H. Tsai, Y. C. Chen, B. L. Lin and C. K. Sun (2004). "Studies of $\chi^{(2)}/\chi^{(3)}$ tensors in submicron-scaled bio-tissues by polarization harmonics optical microscopy." Biophysical Journal **86**(6): 3914-3922.

Cisek, R. (2012). Structural investigation of biological and semiconductor nanostructures with nonlinear multicontrast microscopy. Doctor of Philosophy, University of Toronto.

Cisek, R., N. Prent, C. Greenhalgh, D. Sandkuijl, A. Tuer, A. Major and V. Barzda (2009). Multicontrast nonlinear imaging microscopy. Biochemical applications of nonlinear optical spectroscopy. V. V. Yakovlev. New York, CRC Press**:** 71-102.

Cisek, R., L. Spencer, N. Prent, D. Zigmantas, G. Espie and V. Barzda (2009). "Optical microscopy in photosynthesis." Photosynthesis Research **102**(2): 111-141.

Clay, G. O., A. C. Millard, C. B. Schaffer, J. Aus-Der-Au, P. S. Tsai, J. A. Squier and D. Kleinfeld (2006). "Spectroscopy of third-harmonic generation: evidence for resonances in model compounds and ligated hemoglobin." Journal of the Optical Society of America B-Optical Physics **23**(5): 932-950.

Collins, A. M., H. D. T. Jones, D. X. Han, Q. Hu, T. E. Beechem and J. A. Timlin (2011). "Carotenoid distribution in living cells of *Haematococcus pluvialis* (Chlorophyceae)." Plos One **6**(9): e243021-e243027.

Croce, R., G. Cinque, A. R. Holzwarth and R. Bassi (2000). "The Soret absorption properties of carotenoids and chlorophylls in antenna complexes of higher plants." Photosynthesis Research **64**(2-3): 221-231.

Crowe, L. M. and J. H. Crowe (1988). "Trehalose and dry dipalmitoylphosphatidylcholine revisited." Biochimica et Biophysica Acta - Biomembranes **946**(2): 193-201.

Daimon, M. and A. Masumura (2007). "Measurement of the refractive index of distilled water from the near-infrared region to the ultraviolet region." Applied Optics **46**(18): 3811-3820.

De Meulenaere, E., I. Asselberghs, M. de Wergifosse, E. Botek, S. Spaepen, B. Champagne, J. Vanderleyden and K. Clays (2009). "Second-order nonlinear optical properties of fluorescent proteins for second-harmonic imaging." Journal of Materials Chemistry **19**(40): 7514-7519.

De Meulenaere, E., W. Q. Chen, S. Van Cleuvenbergen, M. L. Zheng, S. Psilodimitrakopoulos, R. Paesen, J. M. Taymans, M. Ameloot, J. Vanderleyden, P. Loza-Alvarez, X. M. Duan and K. Clays (2012). "Molecular engineering of chromophores for combined second-harmonic and two-photon fluorescence in cellular imaging." Chemical Science **3**(4): 984-995.

de Pee, S., C. E. West, D. Permaesih, Martuti, Muhilal and J. G. A. J. Hautvast (1998). "Orange fruit is more effective than are dark-green, leafy vegetables in increasing serum concentrations of retinol and β-carotene in schoolchildren in Indonesia." American Journal of Clinical Nutrition **68**(5): 1058-1067.

Débarre, D. and E. Beaurepaire (2007). "Quantitative characterization of biological liquids for third-harmonic generation microscopy." Biophysical Journal **92**(2): 603-612.

Del Rey, B., U. Keller, T. Torres, G. Rojo, F. Agulló-López, S. Nonell, C. Marti, S. Brasselet, I. Ledoux and J. Zyss (1998). "Synthesis and nonlinear optical, photophysical, and electrochemical properties of subphthalocyanines." Journal of the American Chemical Society **120**(49): 12808-12817.

Denk, W., J. H. Strickler and W. W. Webb (1990). "Two-photon laser scanning fluorescence microscopy." Science **248**(4951): 73-76.

DeWalt, E. L., V. J. Begue, J. A. Ronau, S. Z. Sullivan, C. Das and G. J. Simpson (2013). "Polarization-resolved second-harmonic generation microscopy as a method to visualize protein-crystal domains." Acta Crystallographica Section D-Biological Crystallography **69**: 74-81.

Díaz-García, M. A., I. Ledoux, J. A. Duro, T. Torres, F. Agulló-López and J. Zyss (1994). "Third-order nonlinear-optical properties of soluble octasubstituted metallophthalocyanines." Journal of Physical Chemistry **98**(35): 8761-8764.

Dick, B. (1985). "Irreducible tensor analysis of sum-frequency and difference-frequency-generation in partially oriented samples." Chemical Physics **96**(2): 199-215.

Dombeck, D. A., K. A. Kasischke, H. D. Vishwasrao, M. Ingelsson, B. T. Hyman and W. W. Webb (2003). "Uniform polarity microtubule assemblies imaged in native brain tissue by second-harmonic generation microscopy." Proceedings of the National Academy of Sciences of the United States of America **100**(12): 7081-7086.

Dutta, D., A. Pulsipher, W. Luo, H. Mak and M. N. Yousaf (2011). "Engineering Cell Surfaces via Liposome Fusion." Bioconjugate Chemistry **22**(12): 2423-2433.

Flom, S., R. (2003). Nonlinear optical properties of phthalocyanines. The porphyrin handbook. K. M. Kadish, K. M. Smith and R. Guilard. San Diego, Elsvier. **19:** 179-190.

Flores, M. B. and M. Cervantes (1994). "Nonlinear-optical undergraduate experiments with porphyrin solutions and low-power lasers." Revista Mexicana De Fisica **40**(4): 646-653.

Frank, H. A. and R. L. Christensen (2008). Excited electronic states, photochemistry and photophysics of carotenoids. Carotenoids. G. Britton, S. Liaaen-Jensen and H. Pfander. Boston, Birkhäuser. **4:** 167-188.

Franken, P. A., G. Weinreich, C. W. Peters and A. E. Hill (1961). "Generation of optical harmonics." Physical Review Letters **7**(4): 118-119.

Freund, I. and M. Deutsch (1986). "Second-harmonic microscopy of biological tissue." Optics Letters **11**(2): 94-96.

Freund, I., M. Deutsch and A. Sprecher (1986). "Connective-Tissue Polarity - Optical 2nd-Harmonic Microscopy, Crossed-Beam Summation, and Small-Angle Scattering in Rat-Tail Tendon." Biophysical Journal **50**(4): 693-712.

Frey-Wyssling, A. and F. Schwegler (1965). "Ultrastructure of Chromoplasts in Carrot Root." Journal of Ultrastructure Research **13**(5-6): 543-559.

Fu, G., T. Yoda and K. Kasatani (2005). "Third-order optical nonlinearities of several naphthalocyanines and porphyrins measured by the resonant femtosecond DFWM technique." Nonlinear Optical Phenomena and Applications **5646**: 471-479.

Gaier, K., A. Angerhofer and H. C. Wolf (1991). "The lowest excited electronic singlet-states of all-trans beta-carotene single-crystals." Chemical Physics Letters **187**(1-2): 103-109.

Giovannetti, R., L. Alibabaei and F. Pucciarelli (2009). "Kinetic model for astaxanthin aggregation in water-methanol mixtures." Spectrochimica Acta Part A: Molecular and Biomolecular Spectroscopy **73**(1): 157-162.

Green, B. R., J. M. Anderson and W. W. Parson (2003). Photosynthetic membranes and their light-harvesting antennas. Light-harvesting antennas in photosynthesis. B. R. Green and W. W. Parson. Dordrecht, Kluwer Academic Publishers. **13:** 2-28.

Greenhalgh, C., N. Prent, C. Green, R. Cisek, A. Major, B. Stewart and V. Barzda (2007). "Influence of semicrystalline order on the second-harmonic generation efficiency in the anisotropic bands of myocytes." Applied Optics **46**(10): 1852-1859.

Grunewald, K., J. Hirschberg and C. Hagen (2001). "Ketocarotenoid biosynthesis outside of plastids in the unicellular green alga Haematococcus pluvialis." Journal of Biological Chemistry **276**(8): 6023-6029.

Gruszecki, W. I. (2009). Carotenoids in lipid membranes. Carotenoids: Physical, chemical, and biological functions and properties. J. T. Landrum. Boca Raton, CRC Press**:** 19-30.

Gualtieri, E. J., F. Guo, D. J. Kissick, J. Jose, R. J. Kuhn, W. Jiang and G. J. Simpson (2011). "Detection of membrane protein two-dimensional crystals in living cells." Biophysical Journal **100**(1): 207-214.

Gubler, U., R. Spreiter, C. Bosshard, P. Günter, R. R. Tykwinski and F. Diederich (1998). "Two-dimensionally conjugated molecules: The importance of low molecular symmetry for large third-order nonlinear optical effects." Applied Physics Letters **73**(17): 2396-2398.

Hada, M., Nagy,V., Deli, J. and Agocs, A. (2012). "Hydrophilic carotenoids: Recent progress." Molecules **17**: 5003-5012.

Haupert, L. M. and G. J. Simpson (2011). "Screening of protein crystallization trials by second order nonlinear optical imaging of chiral crystals (SONICC)." Methods **55**(4): 379-386.

Hermann, J. P. and J. Ducuing (1974). "Third-order polarizabilities of long-chain molecules." Journal of Applied Physics **45**(11): 5100-5102.

Hermann, J. P., D. Ricard and J. Ducuing (1973). "Optical nonlinearities in conjugated systems: β-carotene." Applied Physics Letters **23**(4): 178-180.

Hobe, S., S. Prytulla, W. Kuhlbrandt and H. Paulsen (1994). "Trimerization and crystallization of reconstituted light-harvesting chlorophyll *a*/*b* complex." The EMBO Journal **13**(15): 3423-3429.

Jeffrey, S. W. (1997). Chlorophyll and carotenoid extinction coefficients. Phytoplankton pigments in oceanography: Guidelines to modern methods. S. W. Jeffrey, R. F. C. Mantoura and S. W. Wright. Paris, UNESCO Publishing. **10:** 595-596.

Kajzar, F. and J. Messier (1985). "Third-harmonic generation in liquids." Physical Review A **32**(4): 2352-2363.

Kandasamy, K., S. J. Shetty, P. N. Puntambekar, T. S. Srivastava, T. Kundu and B. P. Singh (1999). "Effects of metal substitution on third-order optical non-linearity of porphyrin macrocycle." Journal of Porphyrins and Phthalocyanines **3**(2): 81-86.

Kissick, D. J., C. M. Dettmar, M. Becker, A. M. Mulichak, V. Cherezov, S. L. Ginell, K. P. Battaile, L. J. Keefe, R. F. Fischetti and G. J. Simpson (2013). "Towards protein-crystal centering using second-harmonic generation (SHG) microscopy." Acta Crystallographica Section D-Biological Crystallography **69**: 843-851.

Kissick, D. J., E. J. Gualtieri, G. J. Simpson and V. Cherezov (2010). "Nonlinear optical imaging of integral membrane protein crystals in lipidic mesophases." Analytical Chemistry **82**(2): 491-497.

Kobayashi, M., M. Akiyama, H. Kano and H. Kise (2010). Spectroscopy and structure determination. Chlorophylls and bacteriochlorophylls: biochemistry, biophysics, functions and applications. B. Grimm, R. J. Porra, W. Rudiger and H. Scheer. New York, Springer. **25:** 79-94.

Köhn, S., H. Kolbe, M. Korger, C. Köpsel, Bernhard Mayer, H. Auweter, E. Lüddecke, H. Bettermann and H.-D. Martin (2008). Aggregation and interface behaviour of carotenoids. Carotenoids. G. Britton, S. Liaaen-Jensen and H. Pfander. Boston, Birkhäuser. **4:** 53-98.

Lippitz, M., M. A. van Dijk and M. Orrit (2005). "Third-harmonic generation from single gold nanoparticles." Nano Letters **5**(4): 799-802.

Liu, T. M., S. P. Tai, C. H. Yu, Y. C. Wen, S. W. Chu, L. J. Chen, M. R. Prasad, K. J. Lin and C. K. Sun (2006). "Measuring plasmon-resonance enhanced third-harmonic χ^3 of Ag nanoparticles." Applied Physics Letters **89**(4): 0431221-0431223.

Liu, Z. F., H. C. Yan, K. B. Wang, T. Y. Kuang, J. P. Zhang, L. L. Gui, X. M. An and W. R. Chang (2004). "Crystal structure of spinach major light-harvesting complex at 2.72 Å resolution." Nature **428**(6980): 287-292.

Long, N. J. (1995). "Organometallic compounds for nonlinear optics-The search for en-light-enment!" Angewandte Chemie International Edition **34**(1): 21-38.

Major, A., R. Cisek, D. Sandkuijl and V. Barzda (2009). "Femtosecond Yb:KGd$(WO_4)_2$ laser with > 100 nJ of pulse energy." Laser Physics Letters **6**(4): 272-274.

Maker, P. D., C. M. Savage, R. W. Terhune and M. Nisenoff (1962). "Effects of Dispersion and Focusing on Production of Optical Harmonics." Physical Review Letters **8**(1): 21-&.

Marder, S. R., J. W. Perry, G. Bourhill, C. B. Gorman, B. G. Tiemann and K. Mansour (1993). "Relation between bond-length alternation and second electronic hyperpolarizability of conjugated organic molecules." Science **261**(5118): 186-189.

Marder, S. R., W. E. Torruellas, M. Blanchard-Desce, V. Ricci, G. I. Stegeman, S. Gilmour, J. L. Brédas, J. Li, G. U. Bublitz and S. G. Boxer (1997). "Large molecular third-order optical nonlinearities in polarized carotenoids." Science **276**(5316): 1233-1236.

Matthews, S. J., N. W. Ross, S. P. Lall and T. A. Gill (2006). "Astaxanthin binding protein in Atlantic salmon." Comparative Biochemistry and Physiology Part B: Biochemistry & Molecular Biology **144**(2): 206-214.

Mayer, G. and F. Gires (1964). "Action d'une onde lumineuse intense sur l'indice de refraction des liquides." Comptes Rendus de l'Académie des Sciences **258**(7): 2039-2042.

Mazumder, N., J. J. Qiu, M. R. Foreman, C. M. Romero, P. Torok and F. J. Kao (2013). "Stokes vector based polarization resolved second harmonic microscopy of starch granules." Biomedical Optics Express **4**(4): 538-547.

Mendes-Pinto, M. M., A. M. LaFountain, M. C. Stoddard, R. O. Prum, H. A. Frank and B. Robert (2012). "Variation in carotenoid-protein interaction in bird feathers produces novel plumage coloration." Journal of the Royal Society Interface **9**(77): 3338-3350.

Meredith, G. R., B. Buchalter and C. Hanzlik (1983). "Third-order susceptibility determination by third harmonic generation. I." Journal of Chemical Physics **78**(3): 1533-1542.

Meredith, G. R., B. Buchalter and C. Hanzlik (1983). "Third-order susceptibility determination by third harmonic generation. II." Journal of Chemical Physics **78**(3): 1543-1551.

Meyers, F., S. R. Marder, B. M. Pierce and J. L. Bredas (1994). "Electric-field modulated nonlinear optical properties of donor-acceptor polyenes: Sum-over-states investigation of the relationship between molecular polarizabilities (α, β, and γ) and bond length alternation." Journal of the American Chemical Society **116**(23): 10703-10714.

Milicua, J. C. G., J. L. Juarros, J. Delasrivas, J. Ibarrondo and R. Gomez (1991). "Isolation of a Yellow Carotenoprotein from Carrot." Phytochemistry **30**(5): 1535-1537.

Millard, A. C., P. J. Campagnola, W. A. Mohler, A. Lewis and L. M. Loew (2003). Second harmonic imaging microscopy. Biophotonics. G. Marriott and I. Parker. San Diego, Elsevier. **361:** 47-69.

Millard, A. C., P. W. Wiseman, D. N. Fittinghoff, K. R. Wilson, J. A. Squier and M. Muller (1999). "Third-harmonic generation microscopy by use of a compact, femtosecond fiber laser source." Applied Optics **38**(36): 7393-7397.

Mizutani, G., Y. Sonoda, H. Sano, M. Sakamoto, T. Takahashi and S. Ushioda (2000). "Detection of starch granules in a living plant by optical second harmonic microscopy." Journal of Luminescence **87-9**: 824-826.

Mori, Y., K. Yamano and H. Hashimoto (1996). "Bistable aggregate of all-trans-astaxanthin in an aqueous solution." Chemical Physics Letters **254**(1-2): 84-88.

Muller, M., J. Squier, K. R. Wilson and G. J. Brakenhoff (1998). "3D microscopy of transparent objects using third-harmonic generation." Journal of Microscopy **191**(3): 266-274.

Nagase, H., H. Ueda and M. Nakagaki (1999). "Effects of sonication on the lamellar structures of L-α-dipalmitoyl phosphatidylcholine(DPPC)/saccharide/water systems." Chemical & Pharmaceutical Bulletin **47**(10): 1355-1362.

Nalwa, H. S. (1991). "Organometallic Materials for Nonlinear Optics." Applied Organometallic Chemistry **5**(5): 349-377.

Nucciotti, V., C. Stringari, L. Sacconi, F. Vanzi, L. Fusi, M. Linari, G. Piazzesi, V. Lombardi and F. S. Pavone (2010). "Probing myosin structural conformation in vivo by second-harmonic generation microscopy." Proceedings of the National Academy of Sciences of the United States of America **107**(17): 7763-7768.

Olivier, N., F. Aptel, K. Plamann, M. C. Schanne-Klein and E. Beaurepaire (2010). "Harmonic microscopy of isotropic and anisotropic microstructure of the human cornea." Optics Express **18**(5): 5028-5040.

Oron, D., E. Tal and Y. Silberberg (2003). "Depth-resolved multiphoton polarization microscopy by third-harmonic generation." Optics Letters **28**(23): 2315-2317.

Pillai, R. S., G. J. Brakenhoff and M. Muller (2006). "Analysis of the influence of spherical aberration from focusing through a dielectric slab in quantitative nonlinear optical susceptibility measurements using third-harmonic generation." Optics Express **14**(1): 260-269.

Plotnikov, S. V., A. C. Millard, P. J. Campagnola and W. A. Mohler (2006). "Characterization of the myosin-based source for second-harmonic generation from muscle sarcomeres." Biophysical Journal **90**(2): 693-703.

Prent, N., R. Cisek, C. Greenhalgh, R. Sparrow, N. Rohitlall, M. Milkereit, C. Green and V. Barzda (2005). "Applications of nonlinear microscopy for studying the structure and dynamics in biological systems." Proceedings of SPIE **5971**: 5971061-5971068.

Psilodimitrakopoulos, S., I. Amat-Roldan, P. Loza-Alvarez and D. Artigas (2010). "Estimating the helical pitch angle of amylopectin in starch using polarization second harmonic generation microscopy." Journal of Optics **12**(2010): 0840071-0840076.

Psilodimitrakopoulos, S., V. Petegnief, N. de Vera, O. Hernandez, D. Artigas, A. M. Planas and P. Loza-Alvarez (2013). "Quantitative imaging of microtubule alteration as an early marker of axonal degeneration after ischemia in neurons." Biophysical Journal **104**(5): 968-975.

Psilodimitrakopoulos, S., S. I. C. O. Santos, I. Amat-Roldan, A. K. N. Thayil, D. Artigas and P. Loza-Alvarez (2009). "In vivo, pixel-resolution mapping of thick filaments' orientation in nonfibrilar muscle using polarization-sensitive second harmonic generation microscopy." Journal of Biomedical Optics **14**(1): 0140011-01400111.

Reeve, J. E., H. A. Collins, K. De Mey, M. M. Kohl, K. J. Thorley, O. Paulsen, K. Clays and H. L. Anderson (2009). "Amphiphilic Porphyrins for Second Harmonic Generation Imaging." Journal of the American Chemical Society **131**(8): 2758-+.

Rehberg, M., F. Krombach, U. Pohl and S. Dietzel (2011). "Label-free 3D visualization of cellular and tissue structures in intact muscle with second and third harmonic generation microscopy." Plos One **6**(11): e282371-e282379.

Reintjes, J. F. (1984). Nonlinear Optical Parametric Processes in Liquids and Gases. New York, Academic Press.

Rheims, J., J. Koser and T. Wriedt (1997). "Refractive-index measurements in the near-IR using an Abbe refractometer." Measurement Science & Technology **8**(6): 601-605.

Rojo, G., G. de la Torre, J. García-Ruiz, I. Ledoux, T. Torres, J. Zyss and F. Agulló-López (1999). "Novel unsymmetrically substituted push-pull phthalocyanines for second-order nonlinear optics." Chemical Physics **245**(1-3): 27-34.

Roth, S. and I. Freund (1979). "Second harmonic generation in collagen." Journal of Chemical Physics **70**(4): 1637-1643.

Rusk, N. (2009). Milestone 4 The fluorescence microscope. Nature milestones. London, Nature Publishing Group. **Light Microscopy:** 58-59.

Rustagi, K. C. and J. Ducuing (1974). "Third-Order Optical Polarizability of Conjugated Organic-Molecules." Optics Communications **10**(3): 258-261.

Samoc, A. (2003). "Dispersion of refractive properties of solvents: Chloroform, toluene, benzene, and carbon disulfide in ultraviolet, visible, and near-infrared." Journal of Applied Physics **94**(9): 6167-6174.

Samoc, M., A. Samoc, B. Luther-Davies, Z. N. Bao and L. P. Yu (1998). "Femtosecond Z-scan and degenerate four-wave mixing measurements of real and imaginary parts of the third-order nonlinearity of soluble conjugated polymers." Journal of the Optical Society of America B-Optical Physics **15**(2): 817-825.

Santos, M. F. and J. F. Mesquita (1984). "Ultrastructural study of *Haematococcus lacustris* (Girod.) Rostafinski (Volvocales) .1. Some aspects of carotenogenesis." Cytologia **49**(1): 215-228.

Sastre, A., M. A. Díaz-García, B. Del Rey, C. Dhenaut, J. Zyss, I. Ledoux, F. Agulló-López and T. Torres (1997). "Push-pull phthalocyanines: A Hammett correlation between the cubic hyperpolarizability and the donor-acceptor character of the substituents." Journal of Physical Chemistry A **101**(50): 9773-9777.

Scheer, H. (2003). The pigments. Light-harvesting antennas in photosynthesis. B. R. Green and W. W. Parson. Dordrecht, Kluwer Academic Publishers**:** 29-81.

Scholes, G. D., G. R. Fleming, A. Olaya-Castro and R. van Grondelle (2011). "Lessons from nature about solar light harvesting." Nature Chemistry **3**(10): 763-774.

Schurmann, S., F. von Wegner, R. H. A. Fink, O. Friedrich and M. Vogel (2010). "Second harmonic generation microscopy probes different states of motor protein interaction in myofibrils." Biophysical Journal **99**(6): 1842-1851.

Seely, G. R. and J. S. Connolly (1986). Fluorescence of photosynthetic pigments *in vitro*. Light emission by plants and bacteria. Govindjee, J. Amesz and D. C. Fork. Toronto, Academic Press, Inc.**:** 100-136.

Senge, M. O., H. Hope and K. M. Smith (1992). "Structure and conformation of photosynthetic pigments and related compounds .3. Crystal-structure of beta-carotene." Zeitschrift Fur Naturforschung C **47**(5-6): 474-476.

Shcheslavskiy, V., G. Petrov and V. V. Yakovlev (2003). "Nonlinear optical susceptibility measurements of solutions using third-harmonic generation on the interface." Applied Physics Letters **82**(22): 3982-3984.

Sheik-Bahae, M., A. A. Said, T. H. Wei, D. J. Hagan and E. W. van Stryland (1990). "Sensitive measurement of optical nonlinearities using a single beam." IEEE Journal of Quantum Electronics **26**(4): 760-769.

Sheppard, C. J. R., J. N. Gannaway, R. Kompfner and D. Walsh (1977). "Scanning harmonic optical microscope." Ieee Journal of Quantum Electronics **13**(9): D100-D100.

Simidjiev, I., V. Barzda, L. Mustardy and G. Garab (1997). "Isolation of lamellar aggregates of the light-harvesting chlorophyll a/b protein complex of photosystem II with long-range chiral order and structural flexibility." Analytical Biochemistry **250**(2): 169-175.

Singh, B. P., R. Vijaya, T. Kundu, K. Kandasamy, P. N. Puntambekar, S. J. Shetty and T. S. Srivastava (2001). "Third-order optical nonlinearity of chlorin derivatives." Journal of Porphyrins and Phthalocyanines **5**(2001): 439-441.

Slepkov, A. D., A. Ridsdale, A. F. Pegoraro, D. J. Moffatt and A. Stolow (2010). "Multimodal CARS microscopy of structured carbohydrate biopolymers." Biomedical Optics Express **1**(5): 1347-1357.

Sliwka, H.-R., V. Partali and S. F. Lockwood (2009). Hydrophilic carotenoids: Carotenoid aggregates. Carotenoids: Physical, chemical, and biological functions and properties. J. T. Landrum. Boca Raton, CRC Press**:** 31-58.

Sly, W. G. (1964). "Crystal structure of 15,15'-dehydro-β-carotene." Acta Crystallographica **17**(5): 511-528.

Squier, J. and M. Muller (2001). "High resolution nonlinear microscopy: A review of sources and methods for achieving optimal imaging." Review of Scientific Instruments **72**(7): 2855-2867.

Squier, J. A., M. Muller, G. J. Brakenhoff and K. R. Wilson (1998). "Third harmonic generation microscopy." Optics Express **3**(9): 315-324.

Sreedharanpillai, R. (2006). Isotropic and anisotropic media using focused laser beams. Doctor of Philosophy, The Institutional Repository of the University of Amsterdam.

Standfuss, R., A. C. T. van Scheltinga, M. Lamborghini and W. Kuhlbrandt (2005). "Mechanisms of photoprotection and nonphotochemical quenching in pea light-harvesting complex at 2.5 Å resolution." The EMBO Journal **24**(5): 919-928.

Sterling, C. (1964). "Crystal-structure analysis of β-carotene." Acta Crystallographica **17**(10): 1224-1228.

Sterling, C. (1964). "The crystalline structure of 7,7'-dihydro-β-carotene." Acta Crystallographica **17**(5): 500-505.

Stoller, P., P. M. Celliers, K. M. Reiser and A. M. Rubenchik (2003). "Quantitative second-harmonic generation microscopy in collagen." Applied Optics **42**(25): 5209-5219.

Stoller, P., B. M. Kim, A. M. Rubenchik, K. M. Reiser and L. B. Da Silva (2002). "Polarization-dependent optical second-harmonic imaging of a rat-tail tendon." Journal of Biomedical Optics **7**(2): 205-214.

Stoller, P., K. M. Reiser, P. M. Celliers and A. M. Rubenchik (2002). "Polarization-modulated second harmonic generation in collagen." Biophysical Journal **82**(6): 3330-3342.

Stradi, R., G. Celentano, E. Rossi, G. Rovati and M. Pastore (1995). "Carotenoids in bird plumage-I. The carotenoid pattern in a series of palearctic carduelinae." Comparative Biochemistry and Physiology B-Biochemistry & Molecular Biology **110**(1): 131-143.

Stucky, G. D., S. R. Marder and J. E. Sohn (1991). Linear and nonlinear polarizability: A primer. Materials for nonlinear optics: Chemical perspectives. S. R. Marder, J. E. Sohn and G. D. Stucky. Washington, DC, American Chemical Society. **455:** 2-30.

Sujak, A., J. Gabrielska, J. Milanowska, P. Mazurek, K. Strzalka and W. I. Gruszeeki (2005). "Studies on canthaxanthin in lipid membranes." Biochimica Et Biophysica Acta-Biomembranes **1712**(1): 17-28.

Sun, L. and S. M. Wang (2004). "Spectral and nonlinear optical properties of chlorophyll b depends on distortion of two-dimensional electron configuration along one axis." Dyes and Pigments **61**(3): 273-278.

Supatto, W., D. Debarre, E. Farge and E. Beaurepaire (2005). "Femtosecond pulse-induced microprocessing of live *Drosophila* embryos." Medical Laser Application **20**: 207-216.

Tan, S., F. X. Cunningham, M. Youmans, B. Grabowski, Z. Sun and E. Gantt (1995). "Cytochrome f loss in astaxanthin-accumulating red cells of *Haematococcus pluvialis* (Chlorophyceae): Comparison of photosynthetic activity, photosynthetic enzymes, and thylakoid membrane polypeptides in red and green cells." Journal of Phycology **31**(6): 897-905.

Teisseyre, T. Z., A. C. Millard, P. Yan, J. P. Wuskell, M. D. Wei, A. Lewis and L. M. Loew (2007). "Nonlinear optical potentiometric dyes optimized for imaging with 1064-nm light." Journal of Biomedical Optics **12**(4): 0440011-0440018.

Telfer, A., A. Pascal and A. Gall (2008). Carotenoids in photosynthesis. Carotenoids. G. Britton, S. Liaaen-Jensen and H. Pfander. Boston, Birkhäuser. **4:** 265-308.

Thornber, J. P. (1975). "Chlorophyll-proteins: Light-harvesting and reaction center components of plants." Annual Review of Plant Physiology and Plant Molecular Biology **26**: 127-158.

Tiaho, F., G. Recher and D. Rouede (2007). "Estimation of helical angles of myosin and collagen by second harmonic generation imaging microscopy." Optics Express **15**(19): 12286-12295.

Tokarz, D., R. Cisek, U. Fekl and V. Barzda (2013). "The molecular second hyperpolarizability of the light-harvesting chlorophyll *a*/*b* pigment-protein complex of photosystem II." Journal of Physical Chemistry B **117**(38): 11069-11075.

Tokarz, D., R. Cisek, M. Garbaczewska, D. Sandkuijl, X. Qiu, B. Stewart, J. D. Levine, U. Fekl and V. Barzda (2012). "Carotenoid based bio-compatible labels for third harmonic generation microscopy." Physical Chemistry Chemical Physics **14**(30): 10653-10661.

Tokarz, D., R. Cisek, N. Prent, U. Fekl and V. Barzda (2012). "Measuring the molecular second hyperpolarizability in absorptive solutions by the third harmonic generation ratio technique." Analytica Chimica Acta **755**: 86-92.

Tokarz, D., A. Tuer, R. Cisek, S. Krouglov and V. Barzda (2010). "*Ab initio* calculations of the linear and nonlinear optical properties of amino acids " Journal of Physics: Conference Series **256**(2010): 0120151-0120155.

Tsai, C. K., Y. S. Chen, P. C. Wu, T. Y. Hsieh, H. W. Liu, C. Y. Yeh, W. L. Lin, J. S. Chia and T. M. Liu (2012). "Imaging granularity of leukocytes with third harmonic generation microscopy." Biomedical Optics Express **3**(9): 2234-2243.

Tsai, C. K., T. D. Wang, J. W. Lin, R. B. Hsu, L. Z. Guo, S. T. Chen and T. M. Liu (2013). "Virtual optical biopsy of human adipocytes with third harmonic generation microscopy." Biomedical Optics Express **4**(1): 178-186.

Tsang, T. Y. F. (1995). "Optical third-harmonic generation at interfaces." Physical Review A **52**(5): 4116-4125.

Tuer, A., L. Bakueva, R. Cisek, J. Alami, D. Dumont, J. Rowlands and V. Barzda (2008). "Enhancement of third harmonic contrast with harmonophores in multimodal non-linear microscopy of histological sections." Proceedings of SPIE **6860**(Multiphoton Microscopy in the Biomedical Sciences VIII): 6860051-6860056.

Tuer, A., S. Krouglov, R. Cisek, D. Tokarz and V. Barzda (2011). "Three-dimensional visualization of the first hyperpolarizability tensor." Journal of Computational Chemistry **32**(6): 1128-1134.

Tuer, A., D. Tokarz, N. Prent, R. Cisek, J. Alami, D. J. Dumont, L. Bakueva, J. Rowlands and V. Barzda (2010). "Nonlinear multicontrast microscopy of hematoxylin-and-eosin-stained histological sections." Journal of Biomedical Optics **15**(2): 0260181-0260189.

Tuer, A. E., M. K. Akens, S. Krouglov, D. Sandkuijl, B. C. Wilson, C. M. Whyne and V. Barzda (2012). "Hierarchical model of fibrillar collagen organization for interpreting the second-order susceptibility tensors in biological tissue." Biophysical Journal **103**(10): 2093-2105.

Tuer, A. E., S. Krouglov, N. Prent, R. Cisek, D. Sandkuijl, K. Yasufuku, B. C. Wilson and V. Barzda (2011). "Nonlinear optical properties of type I collagen fibers studied by polarization dependent second harmonic generation microscopy." Journal of Physical Chemistry B **115**(44): 12759-12769.

Tykwinski, R. R., U. Gubler, R. E. Martin, F. Diederich, C. Bosshard and P. Gunter (1998). "Structure-property relationships in third order nonlinear optical chromophores." Journal of Physical Chemistry B **102**(23): 4451-4465.

van Amerongen, H. and R. van Grondelle (2001). "Understanding the energy transfer function of LHCII, the major light-harvesting complex of green plants." Journal of Physical Chemistry B **105**(3): 604-617.

van Beek, J. B., F. Kajzar and A. C. Albrecht (1991). "Resonant third-harmonic generation in all-trans β-carotene: The vibronic origins of the third-order nonlinear susceptibility in the visible region." Journal of Chemical Physics **95**(9): 6400-6412.

van Grondelle, R., R. Monshouwer and L. Valkunas (1996). "Photosynthetic light-harvesting." Berichte der Bunsengesellschaft für physikalische Chemie **100**(12): 1950-1957.

van Grondelle, R. and V. I. Novoderezhkin (2006). "Energy transfer in photosynthesis: experimental insights and quantitative models." Physical Chemistry Chemical Physics **8**(7): 793-807.

Veres, G., S. Matsumoto, Y. Nabekawa and K. Midorikawa (2002). "Enhancement of third-harmonic generation in absorbing media." Applied Physics Letters **81**(20): 3714-3716.

Wayama, M., S. Ota, H. Matsuura, N. Nango, A. Hirata and S. Kawano (2013). "Three-dimensional ultrastructural study of oil and astaxanthin accumulation during encystment green alga *Haematococcus pluvialis*." Plos One **8**(1): e536181-e536189.

Weber, G. and F. W. J. Teale (1957). "Determination of the absolute quantum yield of fluorescent solutions." Transactions of the Faraday Society **53**(5): 646-655.

Williams, R. M., W. R. Zipfel and W. W. Webb (2005). "Interpreting second-harmonic generation images of collagen I fibrils." Biophysical Journal **88**(2): 1377-1386.

Wolf, A. V. (1966). Aqueous Solutions and Body Fluids. New York, Harper & Row.

Wynne, J. J. (1969). "Optical third-order mixing in GaAs, Ge, Si, and InAs." Physical Review **178**(3): 1295-&.

Yelin, D., D. Oron, S. Thiberge, E. Moses and Y. Silberberg (2003). "Multiphoton plasmon-resonance microscopy." Optics Express **11**(12): 1385-1391.

Yelin, D. and Y. Silberberg (1999). "Laser scanning third-harmonic-generation microscopy in biology." Optics Express **5**(8): 169-175.

Yu, C. H., S. P. Tai, C. T. Kung, W. J. Lee, Y. F. Chan, H. L. Liu, J. Y. Lyu and C. K. Sun (2008). "Molecular third-harmonic-generation microscopy through resonance enhancement with absorbing dye." Optics Letters **33**(4): 387-389.

Zelmon, D. E., D. L. Small and R. Page (1998). "Refractive-index measurements of undoped yttrium aluminum garnet from 0.4 to 5.0 μm." Applied Optics **37**(21): 4933-4935.

Zhou, J. R., E. T. Gugger and J. W. Erdman (1994). "Isolation and partial characterization of an 18 kDa carotenoid-protein complex from carrot roots." Journal of Agricultural and Food Chemistry **42**(11): 2386-2390.

Zimmerley, M., P. Mahou, D. Debarre, M. C. Schanne-Klein and E. Beaurepaire (2013). "Probing ordered lipid assemblies with polarized third-harmonic-generation microscopy." Physical Review X **3**(2013): 0110021-01100216.

Statement of Contributions

I performed all second hyperpolarizability measurements in the thesis. I implemented the THG ratio technique in a nonlinear optical microscope, and performed regular alignments and maintenance of the microscope with help from Richard Cisek. Refractive index measurements were the main improvement that I made to the THG ratio technique. I incorporated a device that did not exist at the time (tunable and accurate to 3 decimal places). I built the refractometer from pre-existing components including a xenon arc lamp and a monochromator generously donated by Professor Ulrich Krull (UTM). I replaced the stepper motor in the monochromator and programmed it in LabVIEW with assistance from Professor Barzda and Richard Cisek. I designed the prism holder with helpful discussions from Professor Barzda, Richard Cisek and Adam Tuer. I performed all the refractive index measurements in the thesis. I programmed the numerical implementations to calculate the third-order nonlinear optical susceptibility of solutions in LabVIEW. Nicole Prent assisted in developing a routine used in the program to fit many THG amplitudes.

I performed all major parts of the investigation of carotenoids. I prepared the carotenoid solutions, I made carotenoid liposomes, I made H and J aggregate samples of astaxanthin, and I isolated chromoplasts from carrots. I performed imaging of all these samples using the nonlinear optical microscope. I performed PIPO SHG and PIPO THG measurements on the aggregates, the chromoplasts and thin slices of carrots. The PIPO rotation stages were programmed and implemented by Adam Tuer with help from Richard Cisek. The theory of PIPO SHG was developed by Adam Tuer, Richard Cisek, Serguei Krouglov, Nicole Prent and Professor Barzda. I developed the theory of PIPO THG alongside Richard Cisek, Serguei Krouglov and Professor Barzda.

I performed all aspects of the investigation of chlorophylls as well as mixtures of carotenoids and chlorophylls. Laura Junker and Professor Ingo Ensminger (UTM) graciously donated chlorophyll *a* and *b* for second hyperpolarizability measurements. I prepared the chlorophyll solutions and I performed the THG intensity ratio measurements for these samples. I developed the concept of negative second hyperpolarizabilities from these measurements with Richard Cisek, Professor Barzda and a brief, but valuable discussion with Professor Robert Boyd (University of Ottawa). Dyads of carotenoids and phthalocyanines were synthesized and

provided by Professor Tom Moore, Professor Ana Moore, Katie Wong Carter and Smitha Pillai (Arizona State University). I prepared the solutions of these harmonophores and I performed the THG intensity ratio measurements for these samples. I planted pea plants while Marianne Kalich (UTM Greenhouse) looked after their growth. I isolated LHCII from pea plants with Richard Cisek along with additional guidance from Professor Barzda. I performed measurements of the second hyperpolarizability of LHCII as well as experiments with LHCII and varying detergent concentration with help from Richard Cisek. *Haematoccocus pluvialis* samples were grown and supplied by Omar El-Ansari and Professor George Espie (UTM). I imaged the algae with our nonlinear optical microscope.

I performed all the major aspects of imaging and investigating labeled biological structures with harmonophores. I performed all the imaging for the investigation of labeling muscle with β-carotene. Martyna Garbaczewska and I fed *Drosophila melanogaster* larvae carotenoid-enriched food. Martyna Garbaczewska dissected larvae which were donated by Professor Joel D. Levine (UTM). I performed labeling of human hair with β-carotene as well as the subsequent nonlinear optical imaging. I incubated and labeled *Drosophila* Schneider S2 cells with carotenoid incorporated liposomes. I also imaged the cells with our nonlinear optical microscope. The cells were grown and donated by Xinping Qiu and Professor Bryan Stewart (UTM).